Title
Improving Cosmological Utility of Type Ia Supernovae through Physics and Big Data

Permalink
https://escholarship.org/uc/item/1424b4f8

Author
Siebert, Matthew Ryan

Publication Date
2022

Peer reviewed|Thesis/dissertation

UNIVERSITY OF CALIFORNIA
SANTA CRUZ

IMPROVING COSMOLOGICAL UTILITY OF TYPE Ia SUPERNOVAE THROUGH PHYSICS AND BIG DATA

A dissertation submitted in partial satisfaction of the
requirements for the degree of

Doctor of Philosophy

in

ASTRONOMY AND ASTROPHYSICS

by

Matthew R. Siebert

June 2022

The Dissertation of Matthew R. Siebert is approved:

Ryan J. Foley, Chair

J. Xavier Prochaska

Saurabh W. Jha

Robert P. Kirshner

Peter F. Biehl
Vice Provost and Dean of Graduate Studies

Table of Contents

List of Figures

List of Tables

Abstract

Improving Cosmological Utility of Type Ia Supernovae through Physics and Big Data

by

Matthew R. Siebert

After correcting for their light-curve shape and color, Type Ia supernovae (SNe Ia) are precise cosmological distance indicators. However, there remains a non-zero intrinsic scatter in the differences between measured distance and distances inferred from a cosmological model (i.e., Hubble residuals). We have found that Hubble residuals are correlated with different properties of SN Ia host galaxies (e.g., mass, star-formation rate, and metallicity). Cosmological analyses attempt to correct for these effects empirically without any physical knowledge of the progenitor system, potentially introducing a bias. In this thesis, I detail several projects aimed at uncovering the dominant physical sources of intrinsic scatter.

First, I will present Kaepora, a relational database for SN Ia observations containing 4975 public spectra of 777 SNe Ia. We have significantly improved this data set by inspecting these spectra for quality, removing galactic emission lines and cosmic rays, generating variance spectra, and correcting for the reddening caused by both MW and host-galaxy dust. Using this large homogenized sample, we produce composite spectra that have been precisely controlled for phase and light-curve shape. These composite spectra reproduce known trends with other optical properties of SNe Ia,

and by controlling for these effects, they can be used to investigate a wide parameter space. Critically, with these methods I will show that SN Ia distances can potentially be improved with the knowledge of their ejecta velocities.

I will then describe late time observations of the UV-flashing high-velocity SN Ia 2019yvq. We identify strong Calcium emission in the nebular spectrum of this SN and argue that this indicates SN 2019yvq was likely the result of a sub-Chandrasekhar mass double-detonation explosion. It is possible that 2019yvq-like SNe contribute to our cosmological samples, and the presence of multiple progenitor channels could be a source of Hubble residual intrinsic scatter. A better understanding of SN Ia progenitor environments (which may correlate with progenitor channel) could help us discern the relative contributions of multiple progenitor channels in cosmological samples.

Finally, I will present preliminary results from the Foundation/Swope host galaxy survey (a project which has spanned my entire graduate career). We have obtained optical spectroscopy for 372 out of 517 total SN host galaxies in the Foundation and Swope combined cosmological SN sample (the largest low-z sample). The mass-metallicity relationship of our preliminary sample is consistent with similar samples and contains some of the lowest mass galaxies studied in a cosmological sample. Our sample also shows evidence for a “metallicity-step” using measurements from both the galaxy nucleus and the supernova location. With the full sample, we hope to constrain the functional form of this relationship and better understand the underlying physical cause of the empirical host-galaxy correction.

For my grandfather, Dr. Alan Siebert

Personal Acknowledgments

First, I would like to thank Ryan Foley. From very early on, Ryan's enthusiasm for transient astronomy inspired me to pursue a career in the field. His consistent support as an advisor has had an enormous impact on my professional development and overall confidence. I am very grateful that Ryan also saw talent in me as a mentor and encouraged me to work with younger students. These relationships have been some of the most rewarding experiences in my graduate career.

Ryan and I fortuitously arrived at the same time at UCSC and this allowed me to watch and participate in the growth of the group from the ground up. I have learned so much from this unique experience, and our group should be really proud of everything we have built together. On this note, I would also like to thank the UCSC transients team as a whole. Georgios, Dave, Charlie, David, Cesar, Ari, Kyle, and many others, your camaraderie and support has been so important to me over these years.

I specifically want to thank some of the students I have worked with closely. Kyle, Erika, and Rodrigo, it has been a delight to get to know you and see you succeed, you all have inspired me more than you know. I am incredibly proud to be able to call all of you my peers, and I cannot wait to see what you all do next.

Special thanks to my Santa Cruz friends Zack, Grecco, and Platon for sharing your free time and bizarre senses of humor with me over the years. I also want to thank my “COVID bubble” consisting of Callie, Enia, Amanda, Zack, and Grecco. Despite a global pandemic and local wildfires, we were still able to find some fun and I am very grateful for your support and friendship during this uncertain time. Furthermore Callie, getting to know you has been the highlight of the tail end of my graduate career and your companionship has meant the world to me.

Finally, I would like to thank my parents Keith and Cheryl, and my brother Mark for their unconditional love and support. I couldn't have done it without you all cheering me on.

Published Material

The text of this dissertation includes reprints of the following published material led by Siebert, with the permission of the listed coauthors.

Chapter 2 was published in the literature as Siebert et al. (2019). I was responsible for performing the analysis, writing the text, and creating the figures. I wish to thank my coauthor Ryan J. Foley for his generous support and feedback in the course of this research.

Chapter 3 was published in the literature as Siebert et al. (2020a). I was responsible for performing the analysis, writing the text, and creating the figures. I wish to thank my coauthor Ryan J. Foley and David O. Jones for their generous support and feedback in the course of this research.

Chapter 4 was published in the literature as Siebert et al. (2020b). I was responsible for performing the analysis, writing the text, and creating the figures (with the exception of Fig. 4.5 and the left panel of Fig. 4.6). I wish to thank my coauthors Ryan J. Foley, Georgios Dimitriadis, and Abigil Polin for their generous support and feedback in the course of this research.

Scientific Acknowledgments

I gratefully acknowledge research support from the National Science Foundation Graduate Research Fellowship Program Under Grant No. 1842400. This research was further supported by NASA grant NNG17PX03C, NSF grant AST-1815935, the Gordon & Betty Moore Foundation, the Heising-Simons Foundation, and by a fellowship from the David and Lucile Packard Foundation to R.J.F. The Computational HEP program in The Department of Energy's Science Office of High Energy Physics provided resources through Grant #KA2401022. Calculations presented in these papers used resources of the National Energy Research Scientific Computing Center (NERSC), which is supported by the Office of Science of the U.S. Department of Energy under Contract No. DE-AC02-05CH11231.

An integral part of this thesis (`kaepora`) relies on data obtained over several decades by many researchers. Critically, these scientists made their data publicly available for additional studies such as this. We thank all of the telescope operators, observers, data reducers, and PIs who's whose hard work and attention to detail were crucial for this project's success. This project was initiated as part of an undergraduate and graduate seminar at the University of Illinois by R.J.F. We thank A. Beaudoin, Y. Cao, R. Chue, B. Fry, Y. Lu, S. Rubin, and A. Snyder for their contributions in the project's infancy.

A significant portion of this project was made possible by observations made with the NASA/ESA Hubble Space Telescope, obtained from the Data Archive at the Space Telescope Science Institute, which is operated by the Association of Universities for Research in Astronomy, Inc., under NASA contract NAS 5–26555. These observations are associated with programs GO–4016, GO–12298, GO–12582, GO–12592, GO–13286, and GO–13646. Swift spectroscopic observations were performed under programs GI–04047, GI–5080130, GI–6090689, GI–8110089, GI–1013136, and GI–1215205; we are very grateful to N. Gehrels, S.B. Cenko, and the Swift team for executing the observations quickly.

A large fraction of the data presented herein were obtained at the W. M. Keck Observatory, which is operated as a scientific partnership among the California Institute of Technology, the University of California and the National Aeronautics and Space Administration. The Observatory was made possible by the generous financial support of the W. M. Keck Foundation. I wish to recognize and acknowledge the very significant cultural role and reverence that the summit of Maunakea has always had within the indigenous Hawaiian community. We are most fortunate to have the opportunity to conduct observations from this mountain.

Chapter 1

Introduction

1.1 Type Ia supernovae are "standardizable" candles

SNe Ia are widely accepted to result from the thermonuclear explosions of near-Chandresekhar mass carbon-oxygen (C/O) white dwarfs (WDs). In the context of other explosive phenomena, these events are intrinsically very bright ($M_B \sim -19$ mag at peak), and despite contributing roughly only a quarter of all SNe by volume, they are the most commonly discovered class of SN, typically $\sim 80\%$ of magnitude-limited samples (Li et al. 2011a; Jones et al. 2021).

As a class of SN, these events show remarkable uniformity in their light curves. The end product of the thermonuclear process is unstable ^{56}Ni. At early times, SNe Ia exhibit a photospheric phase where their luminosities are entirely driven by the radioactive decay of ^{56}Ni to ^{56}Co. The high-energy gamma rays produced in this decay are reprocessed in the dense and optically thick expanding ejecta, shifting them to larger wavelengths in the ultraviolet (UV), optical, and infrared. These photons free-stream when they reach a location in the ejecta with low enough opacity to escape. At maximum light 85% of the observed luminosity of SNe Ia is at rest-frame optical wavelengths (Howell 2011). The resulting maximum light spectrum is a black-body with the broad characteristic P-Cygni absorption features that reveal the nucleosynthetic products in the outer layers of the ejecta. The expansion velocity inferred from these features indicates a kinetic energy of 10^{51} ergs, two orders of magnitude larger than the energy produced via the radioactive decay chain of ^{56}Ni.

The characteristic width of a SN Ia light curve is set by the diffusion timescale of the gamma rays produced in the decay of ^{56}Ni to ^{56}Co. This powers the light curve for the first few weeks (Colgate & McKee 1969). The peak luminosity corresponds to the instantaneous rate of energy deposition from this radioactive decay and is a direct result of the total amount of ^{56}Ni produced in the explosion (Arnett 1982). Differences in the amount ^{56}Ni produced leads to a range of peak luminosities that spans an order of magnitude, meaning these phenomena are not true "standard candles". Fortunately, an empirical relationship has been observed between SN Ia peak luminosity and light-curve shape. Intrinsically bright SNe Ia tend to have broad, slowly evolving light curves, while fainter SNe Ia have narrow, fast evolving light curves (Phillips 1993). This width-luminosity relationship facilitates the use of SN Ia as cosmological distance indicators.

The origin of this width-luminosity relationship is more enigmatic than the processes described thus far. A common interpretation is that differences the mean opacity and ionization state of the ejecta vary with the amount of ^{56}Ni generated in the explosion. A larger ^{56}Ni mass results in more radioactive heating, larger temperatures, and more ionization all of which can contribute to increasing the diffusion timescale (Pinto & Eastman 2000, 2001). However, others have found that spectroscopic differences are the primary driver of the width-luminosity relationship. Kasen & Woosley (2007) showed that after maximum light, the spectra of SNe Ia are greatly affected at bluer wavelengths by line blanketing from Fe II and Co II. They argued that the lower temperatures of lower-luminosity SNe Ia result in an earlier recombination of Fe III to Fe II, causing a faster B-band decline rate. It is likely that all of these effects play a role in the width-luminosity relationship, but regardless of its physical origin, this relationship is of great importance for SN Ia cosmology.

1.2 Constraining dark energy by mapping the expansion history of the Universe

A primary technique for measuring the expansion history of the Universe involves relating the redshift, z, observed in astronomical phenomena to their inferred distances. This is done through the Friedmann equation which is derived directly from Einstein's theory of General Relativity and can be expressed as:

$$\frac{H(z)^2}{H_0^2} = \Omega_{0,R}(1+z)^4 + \Omega_{0,M}(1+z)^3 + \Omega_{0,k}(1+z)^2 + \Omega_{0,\Lambda} \tag{1.1}$$

$H(z)$ is the Hubble parameter (defined as $\frac{\dot{a}}{a}$). Here $a(t)$ is the dimensionless scale factor relating the proper distance between two objects in an expanding universe as a function of time since the beginning of the Universe ($a = 1$ at present time). It is related to the redshift by $a = 1/(1+z)$. $\Omega_{0,R}$, $\Omega_{0,M}$, $\Omega_{0,k}$, and $\Omega_{0,\Lambda}$, are the radiation, matter, spatial curvature and vacuum density at present time, respectively.

By observing the flux, F, of objects with known intrinsic luminosity, L, often referred to as "standard candles", we can measure a luminosity distance:

$$d_L = \sqrt{\frac{L}{4\pi F}} \tag{1.2}$$

Accounting for the dilution of energy in photons due to redshifting, the luminosity distance can be expressed as $d_L = a_0 r(1+z)$, where r is the comoving distance. This allows us to numerically solve the Friedmann equation relating d_L, z, and the fundamental cosmological parameters. By measuring d_L as a function redshift, we can determine these parameters (H_0^2, $\Omega_{0,R}$, $\Omega_{0,M}$, $\Omega_{0,k}$, and $\Omega_{0,\Lambda}$), and furthermore the dark energy equation of state parameter, w, which determines the relationship of how the energy density of dark energy scales with a.

The accelerating expansion of the Universe was proven by calibrating SN Ia luminosities through relationships of their peak luminosities with their light-curve shapes and colors (Riess et al. 1998; Perlmutter et al. 1999). Modern cosmological experiments show strong evidence that we live in a flat universe with dark energy in the form of a cosmological constant, and presence of cold dark matter (ΛCDM). However, open questions still remain. In particular, measurements of H_0 inferred from the early universe via the cosmic microwave background (CMB) still disagree with local measurements of H_0 using supernovae. Specifically, using a sample of SN Ia, Riess et al.

(2021) find $H_0 = 73.30 \pm 1.04$ km s^{-1} Mpc^{-1}, a 5σ difference from the value predicted by Planck+ΛCDM (67.4 ± 0.5 km s^{-1} Mpc^{-1}; Planck Collaboration et al. 2020). Additionally, modern SN Ia samples still cannot distinguish between dark energy with an equation of state parameter above or below $w = -1$, and a higher precision is needed in order to constrain the potential for an evolving dark energy equation of state (w_a).

1.3 Unaccounted physics affects distance measurements

One way to assess the precision of SN Ia distance measurements is by looking at the differences between our measured distances and those predicted by a best fit cosmological model. With current techniques, the scatter in these residuals (known as Hubble residuals or HRs) can be reduced to ∼8% (Scolnic et al. 2018; Jones et al. 2019). Photometric uncertainty in the measurements cannot alone account for this scatter (~ 0.1 mag), therefore there is likely additional physics that goes unaccounted in the calibration process.

It is well known that several observation properties of SN Ia correlate with host environment. In particular, prior to calibration, SN Ia luminosities depend on host galaxy star formation rate (SFR), metallicity, and age. Additionally, Wang et al. (2013) found that high-velocity SN Ia tend to prefer higher-mass host galaxies and tend to occur closer to the host galaxy nucleus, both indicating a higher metallicity. While not a problem for cosmology, these results indicate the potential for contributions from multiple progenitor channels in our cosmological samples.

The well-studied host-galaxy mass step is the best evidence we have so far that unaccounted physics plays a role in our distance measurements. Several studies have confirmed that HRs are negatively correlated with host galaxy mass. Meaning the *corrected* luminosities of SN Ia appear brighter in more massive host galaxies than one would expect from a cosmological model (Kelly et al. 2010; Lampeitl et al. 2010; Sullivan et al. 2010). Other properties of SN Ia host galaxies like metallicity (D'Andrea et al. 2011; Childress et al. 2013c; Pan et al. 2014), sSFR (Childress et al. 2013c), local SFR (Rigault et al. 2013, 2018), local sSFR (Rigault et al. 2018), and local colors (Roman et al. 2018; Jones et al. 2018b), have also been shown to correlate with HR. We still do not know which of these effects is dominant and whether we are simply measuring degeneracies among these properties (i.e. more massive hosts tend to be more metal-rich). Regardless, current cosmological analyses treat the mass-HR relationship as a step function and apply a correction without knowledge of its physical origin. These environmental indicators must be a proxy for some physical process related to the progenitor system.

1.4 The Type Ia supernovae progenitor problem

Even after multiple decades of SN Ia research, we still cannot answer basic questions about their progenitor systems. The generally accepted picture is that SN Ia occur in binary systems where interaction with a companion star leads to the thermonuclear detonation of a C/O WD. Two broad categories of progenitor systems are thought to play a role in the main population of SN Ia. In one, a C/O WD accretes material from a companion main sequence or asymptotic giant branch star (Whelan & Iben

1973; Nomoto 1982). The primary WD eventually accretes enough mass to produce the central temperatures and pressures needed to ignite Carbon fusion and produce a runaway thermonuclear reaction. This is commonly referred to as the single degenerate (SD) scenario, and requires that the primary WD reach a mass that is (somewhat coincidentally) near the Chandresekhar limit (1.4 $M_{\odot}$).

Another popular scenario involves the interaction of two WDs in a close binary system (the double degenerate or DD scenario). In this scenario the mass of the system may exceed the Chandresekhar limit. One possibility is that two WDs in a binary lose energy and angular momentum via gravitaional wave radiation and eventually merge to produce a SN Ia (Iben & Tutukov 1984; Webbink 1984). So far no companion star has been discovered for nearby SNe Ia, providing support for the DD scenario. Other explosion mechanisms potentially exist for both SD and DD progenitors.

Some studies have proposed that surface detonations caused by the accretion of Helium can propagate a shock into the primary WD and trigger a Carbon core detonation that unbinds the star. Since C/O WDs have thin Helium layers, this mechanism has been proposed for both non-degenerate (Nomoto 1982; Woosley et al. 1986) and and degenerate companions (Bildsten et al. 2007; Shen & Bildsten 2009). Thus in both scenarios, the range of potential primary WD masses can fall significantly below the Chandresekhar limit.

In the last decade, advances in the field of SN Ia progenitor physics have been enabled by extremely high quality observations of individual SNe. For example, the proximity of SN Ia 2011fe and 2014J (7.2 Mpc and 3.5 Mpc, respectively) allowed for extensive follow-up campaigns that resulted in strong constraints on the presence of non-degenerate companion stars. More recently, a great deal of attention has been given to a sub-population of SN Ia with flux-excess in their very early light curves. Several explosion models have gained popularity and been invoked to explain the diversity of SN Ia. In particular, there are a variety predictions based on the modeling of ejecta interaction with a companion star (Kasen 2010), double-detonations of sub-Chandrasekhar mass white dwarfs (Shen et al. 2018a; Polin et al. 2019), Nickel clumps in the SN ejecta (Piro & Morozova 2016), and violent mergers (Pakmor et al. 2010). Obtaining high-quality observations of individual SNe is important for constraining specific explosion mechanisms, progenitor systems, and understanding their potential contributions to cosmological samples.

It is still unclear whether both SD and DD progenitors are needed to produce the observed population of SNe Ia used in cosmological studies. Several studies have argued that SD progenitors cannot alone reproduce the observed delay-time distribution of SNe Ia, measured from the lag between cosmic SFR and SN Ia production (Mannucci et al. 2006; Totani et al. 2008). Some studies have shown that SD and DD progenitor systems may produce SN Ia at similar rates (Maoz & Mannucci 2008; Foley et al. 2012c). It is likely that both progenitor systems contribute to cosmological samples and even contribute to Hubble scatter. If SNe Ia from SD and DD systems are produced by populations with different progenitor ages, the total population of SNe Ia will evolve with cosmic time. If the environmental relationships of host galaxy mass, SFR, and metallicity with HR are in fact manifestation of differences in progenitor age, then it is possible that SN Ia distance measurements could be biased with redshift (Childress et al. 2014). We do not yet know how differences in progenitor companion stars and explosion mechanisms could affect SN Ia light-curves and colors in a way that would not be corrected using current methods.

1.5 The diversity of SN Ia ejecta velocities

Ejecta velocity appears to a key component to unlocking the unexplained diversity in SN Ia. Velocity is correlated with several other observables known to be indicators of the progenitor system and/or explosion physics, and is currently not used to inform SN Ia distance measurements. Maeda et al. 2011 found that an off-center ignition model could be used to explain the correlations that they observed among, the velocity gradient, presence of Carbon in early optical spectra, and emission line shifts in nebular spectra. Polin et al. 2019 suggest that SN Ia coming from sub-Chandrasekhar mass double detonations are distinguished by their ejecta velocities, peak luminosities, polarization (Cikota et al. 2019), and nebular Ca emission. Sternberg et al. (2011) suggested that variable Na D velocity profiles in SN Ia indicate that roughly 20% of SN Ia could originate from a SD channel. Foley et al. 2012c found that high-velocity SN Ia tend to have blue-shifted and stronger Na D absorption profiles. This result is supported by the existence of multiple progenitor systems, or if a single progenitor channel is dominant, indicates the need for asymmetric ejecta.

Several other studies have pointed to asymmetric ejecta distributions as being the root for a known relationship with velocity. In such studies, Foley et al. 2011 found that high-velocity SN Ia tend to have redder intrinsic $B-V$ colors at maximum light, Cikota et al. 2019 found that higher-velocity SN Ia tend to have higher Si II line polarization, and Zhang et al. 2020 found that the existing SN Ia velocity distribution in the literature is likely bimodal. Furthermore, velocity has suggested correlations with the presence of high velocity features (Silverman et al. 2015) and light-curve rise time (Ganeshalingam et al. 2011). SN Ia velocities maybe linked to properties of their host galaxy environments (Wang et al. 2013), and investigating this connection is of critical importance for understanding if ejecta velocity can be used to reduce Hubble scatter.

1.5.1 Progenitor metallicity can affect optical properties of SNe Ia

The effect of progenitor metallicities on SN Ia UV continua is a clear prediction from theory. Variable amounts of ^{56}Ni are produced in SN Ia. This affects the overall temperature, opacity, and diffusion timescales of the ejecta, and results in the width-luminosity (Phillips 1993), and color-luminosity relationships (Tripp 1998). Theory suggests that progenitor metallicity could also affect ^{56}Ni yields and thus overall SN luminosity (Timmes et al. 2003). Higher-metallicity progenitors should generate less ^{56}Ni since their excess neutrons allow for the generation of a larger fraction of stable iron-group elements (IGEs). Since the overall composition is not altered, the opacity should not change significantly, and the optical light-curve shape should be unaffected while producing a lower peak luminosity. The increased fraction of IGEs in higher metallicity SN Ia is also expected to increase the amount of line blanketing, and thus have the largest impact on the UV continuum. This effect was likely observed in high quality observations of two "twin" SN Ia.

Observations of the "twin" SN Ia 2011fe and 2011by showed that these events had nearly identical optical SEDs yet dramatically differed at UV wavelengths (Foley & Kirshner 2013b). SN 2011by had a lower peak luminosity and suppressed UV flux consistent with predictions from theory for having a higher metallicity. The gas-phase metallicities of 12 + log(O/H) from the host galaxies of these SN are also consistent with differing by ~ 0.5 dex. Their optical light-curve shape and colors are nearly identical, meaning that their peak luminosities would not be corrected with current methods. Thus, progenitor metallicity could be a significant source of Hubble scatter. Pan et al. (2019) looked at a larger sample of SN Ia UV spectra and found that SN Ia HRs are positively correlated with progenitor metallicity; however, Brown et al. (2018) did not find evidence for this UV flux-metallicity correlation. More work is needed to understand whether the progenitor metallicity is accurately represented by estimates from its host galaxy environment.

1.6 Outline of this work

The multi-dimensional nature of the diversity in SN Ia observational properties demonstrates the necessity for large samples. In Chapter 2, I first show how I have leveraged decades of public SN Ia data to produce a homogeneous sample of spectra in an open-source relational database called `kaepora`. The suite of analysis tools developed for this project allow for the generation of composite spectra that are precisely controlled for their phase and light-curve shape. These composite spectra are then used to reproduce known sequences in SN Ia spectral features, and we show how they can be used to isolate the effects of single parameters on the whole SN Ia spectral energy distribution (SED). Chapter 3 builds on this concept by using the `kaepora` framework to investigate the potential for relationships between SN Ia spectral properties and HRs. We show that SN Ia ejecta velocities are potentially related to HRs. In Chapter 4 an extensive study is performed to explain the late time observations of the UV-flashing high-velocity SN Ia 2019yvq. Finally Chapter 5, presents preliminary results from the Foundation/Swope host galaxy survey. In this work, we present spectroscopic observations of both the global and local environmental properties of SNe Ia in a cosmological sample. We investigate how these measurements correlate with HRs.

Chapter 2

Investigating the Diversity of Type Ia Supernova Spectra with the Open-Source Relational Database Kaepora

2.1 Introduction

Type Ia (SNe Ia) are excellent cosmological probes and an important tool for understanding dark energy. In general, the accepted models for these phenomena involve the thermonuclear disruption of a carbon-oxygen white dwarf. Despite their reputation as “standard candles”, the observational properties of these explosions are intrinsically heterogeneous (Hatano et al. 2000; Blondin et al. 2012b). SN Ia luminosities can vary by an order of magnitude (Pskovskii 1977). The "standardizability" of these events only became evident after observing some basic correlations between these optical properties. Mainly, SNe Ia exhibit an empirical relationship between peak luminosity and light-curve width (Pskovskii 1977; Phillips 1993; Riess et al. 1996). This relationship has been attributed to the varying amount of ^{56}Ni produced in these explosions (Arnett 1982; Nugent et al. 1995; Stritzinger et al. 2006).

The normalization of SN Ia luminosities via this relationship allows for precise distance measurements on extragalactic scales. Measurements of SNe Ia were used to show that the expansion of our universe is currently accelerating (Riess et al. 1998; Perlmutter et al. 1999). Today, after making corrections for light-curve shape and color, there remains an intrinsic scatter that may belie unaccounted SN physics (Foley & Kasen 2011; Scolnic et al. 2018; Jones et al. 2018a). This scatter will soon become a dominant source of systemic uncertainty for SN Ia distance measurements (Jones et al. 2018a).

Although valuable, these basic correlations do not adequately explain the observed spectral diversity. For example, SNe Ia with the same light-curve shape and color exhibit a wide range of photospheric velocities at maximum light (Hatano et al. 2000). Spectra provide an abundance of information about SN ejecta (e.g., nucleosynthesis, ionization states, kinematics, etc.) necessary for constructing a complete picture of these phenomena.

Despite their proven cosmological utility, open questions remain regarding the physical processes that can produce the observed range of diversity. Detailed studies of individual events have been essential for improving our understanding of how spectral features change with phase and luminosity. The well-sampled spectroscopic observations of SN 2011fe solidified our understanding of the optical properties of normal SNe Ia from very early to very late epochs (Nugent et al. 2011; Pereira et al. 2013b; Shappee et al. 2013; Mazzali et al. 2014b). Observations of the spectroscopically distinct SNe 1991T (Phillips et al. 1992; Filippenko et al. 1992d) and 1991bg (Filippenko et al. 1992b; Leibundgut et al. 1993) highlight how the temperature of the SN ejecta can impact spectral features. SN 1991T exhibited a large intrinsic luminosity and showed very little Ca H&K and Si II $\lambda5972$ absorption. In addition to its low intrinsic luminosity, SN 1991bg showed strong Ti II absorption near 4300 Å at maximum light. These effects have been attributed to a sequence in the photospheric temperature where peculiar events like SNe 1991T and 1991bg lie in the high- and low-temperature tails of this relationship, respectively (Nugent et al. 1995). This sequence could be described by the tight correlation between light-curve shape and the ratio of the depth Si II $\lambda5972$ and $\lambda6355$ ($\mathcal{R}$(Si II)). While very useful, detailed analyses of a few individual events cannot fully represent the observed spectroscopic diversity.

Branch (1987) first showed that ejecta velocities of SNe Ia are heterogeneous. Studies of larger samples have revealed that the nature of the diversity of SNe Ia properties is indeed multidimensional (Hatano et al. 2000; Li et al. 2001c; Benetti et al. 2005; Foley et al. 2011; Blondin et al. 2012b). For normal SNe Ia, the velocities derived from Si II $\lambda6355$ do not correlate with the decline-rate parameter $\Delta m_{15}(B)$ (Hatano et al. 2000). Foley & Kasen (2011) showed that high-velocity (HV) SNe Ia have redder intrinsic colors. Furthermore, subgroups of SNe Ia exhibit a large range of velocity gradients for the Si II $\lambda6355$ feature. Benetti et al. (2005) showed that for normal SNe Ia, this velocity gradient does not correlate with $\Delta m_{15}(B)$. Additional observations have also revealed the presence of high-velocity features (HVF) in numerous events. These typically appear as double-troughed absorption profiles in Si II $\lambda6355$, Ca II H&K, or the Ca II near-infrared triplet (Gerardy et al. 2004; Mazzali et al. 2005a,b; Foley et al. 2012b; Childress et al. 2013a; Silverman et al. 2015). HVF strength was shown to correlate with the maximum-light velocity of Si II $\lambda6355$ (Childress et al. 2014). Filling this photometric and spectroscopic parameter space has proven difficult even with large individual SN data sets.

Studies of the mean spectroscopic properties of SNe Ia have been particularly useful for cosmology. Distance estimators require spectral models so that photometric measurements can be calibrated. Spectral models are also useful for estimating bolometric luminosities and thus ^{56}Ni yields (Howell et al. 2009). Nugent et al. (2002) first developed a spectral template for the purpose of representing the temporal evolution of normal SNe Ia. Similarly, Hsiao et al. (2007) constructed a mean spectral template time series using ∼600 spectra of ∼100 normal SNe Ia. Sparse sampling of the observed spectroscopic diversity has limited most data-driven spectral templates to single-parameter models (typically phase). The Nugent and Hsiao template spectra are only representative of normal SNe Ia and do not vary with $\Delta m_{15}(B)$. To best represent the heterogeneous nature of SNe Ia, all available spectroscopic data and metadata should be compiled.

Large efforts have been made to improve the accessibility of spectroscopic SN data. Online databases such as SUSPECT (Richardson et al. 2001), WISEREP (Yaron & Gal-Yam 2012), and the Open Supernova Catalog (Guillochon et al. 2017) have all provided access to large samples of spectra covering decades of observations. However, since the origins of these data are heterogeneous, studying the bulk properties of these data has been challenging. These spectra have been reduced using different techniques and come from a variety of telescopes and instruments. Thus, the available spectra vary greatly in many basic properties (e.g., wavelength coverage, resolution, signal-to-noise ratio, reduction quality, existence of telluric correction, variance spectra, etc.) Furthermore, online databases do not often link these samples to their respective calibrated light-curves and photometric metadata. While some groups have released large homogenized spectroscopic samples (Blondin et al. 2012b; Silverman et al. 2012b; Folatelli et al. 2013b), no efforts have been made to make use of all available SN Ia spectra at once.

In order to properly combine these data, we have developed a framework to homogenize these spectra. By taking steps like inspecting individual spectra for quality, removing unwanted features, generating variance spectra, correcting for Milky-Way (MW) extinction, and interpolating to constant resolution, we are able to provide a fully homogenized sample containing 4975 spectra of 777 SNe Ia and their associated event specific and spectrum specific metadata. One way we aim to improve the efficiency of SN Ia analyses is via leveraging the power of relational queries. A relational database model simplifies data retrieval and provides a structure that is easily scalable in order to accommodate the rapidly increasing number of SN observations. In this work, we present a comprehensive relational database for observations of SNe Ia. We generate composite spectra from subsets of the data in order to validate the data itself and our processing techniques. The database used in this work and all composite spectra presented below can be found online[1]. The source code developed here is open and freely available for use[2]. Installation instructions and example code are also available online[3]. Here we outline how to query the database for subsamples of individual spectra, and produce composite spectra if desired.

In Section 2, we overview the demographics of the dataset. In Section 3, we outline the reprocessing steps that we execute to homogenize all spectroscopic data and the methods we use for spectroscopic analyses. In Section 4 we present our composite spectra generated from various subsets of these data, compare these composites spectra with other template spectra, and use these composite spectra to investigate SN Ia spectral variations related to their host-galaxy environments. Finally in Section 5, we summarize our results and discuss the future potential for uses of our relational database.

2.2 Sample

Our database currently contains 4975 spectra of 777 SNe Ia. The full sample is comprised of spectra from heterogeneous data sources. The majority of our data are sourced from the Center for Astrophysics (CfA) Supernova Program (Blondin et al. 2012b), the Berkeley SN Ia Program (BSNIP; Silverman et al. 2015), and the Carnegie

---

[1] https://msiebert1.github.io/kaepora/

[2] https://github.com/msiebert1/kaepora

[3] https://kaepora.readthedocs.io/en/latest/index.html

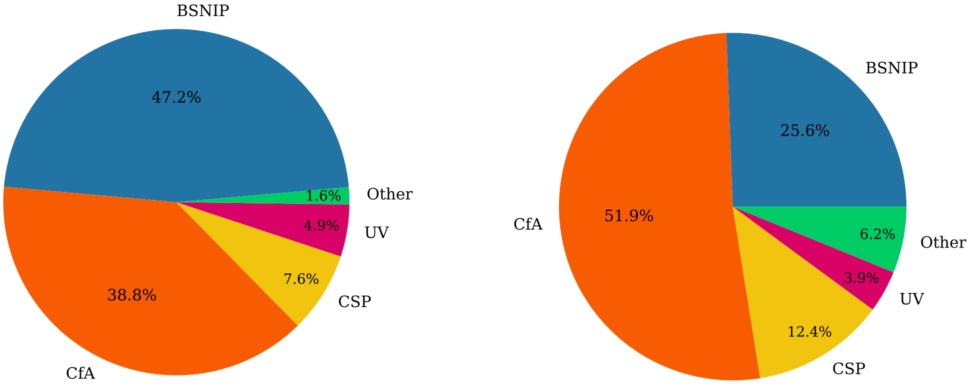

Figure 2.1: (*left*): Contributions of each major data source to the total number of SNe in the database. (*right*): Contributions of each major data source to the total number of spectra in the database. The BSNIP sample provides the largest number of individual SNe, while the CfA sample tends to provide the largest number of spectra per SN.

Supernova Project (CSP; Folatelli et al. 2013b). These sources provide 2584, 1273, and 616 spectra respectively. We also include 195 *Swift* and *HST* UV spectra, and 307 spectra from various other sources detailed in Table 2.1. The relative contributions to the total number of objects and spectra from each source are shown in Figure 2.1. While BSNIP and the CfA have observed a comparable number of SNe, the CfA has acquired more spectra per object. Figure 2.2 shows the relative contributions of these sources as a function of wavelength. The two largest samples, CfA and BSNIP, are complementary. The CfA data are very important for representing SNe Ia at a range of epochs, and the BSNIP spectra are vital for their larger wavelength range (extending from $\sim$3000 – 10000 Å). These data are linked to a variety of event-specific and spectrum-specific metadata. We also include light-curves from the Open Supernova Catalog (Guillochon et al. 2017) that overlap with our sample of SNe Ia.

Individual spectra have been inspected by eye for quality. Those that are

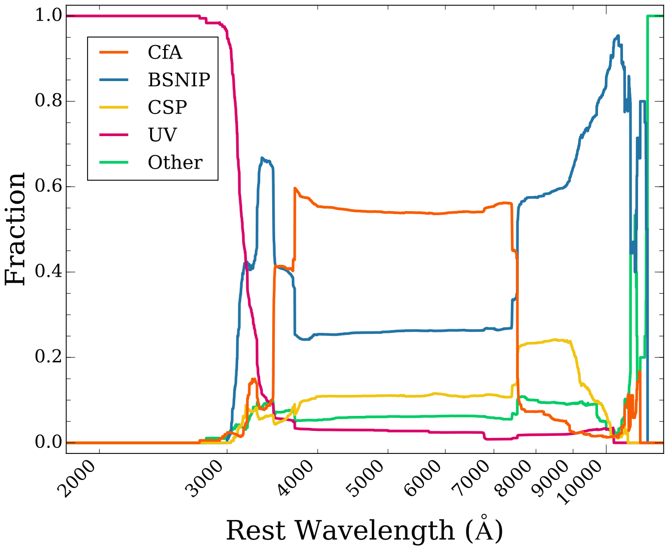

Figure 2.2: Fraction of all spectra coming from the major sources as a function of wavelength. The CfA sample is the dominant source of spectra in the range of ∼3500 − 7500 Å. The BSNIP sample is incredibly important for reaching wavelengths >7500 Å, and *Swift* and *HST* spectra provide the valuable data <3000 Å.

dominated by noise or contain large wavelength gaps are discarded. Spectra with considerable telluric contamination have been identified and flagged. Details for individual spectra are provided in Table 2.1. Associated metadata for each SN contained within the database are described in Table 2.2.

2.2.1 Nominal Sample

We explore the diversity of spectral properties of SNe Ia for a large subsample of these data. The main criterion for selecting this subsample from the total SN sample was whether there was a calibrated light-curve covering the time of maximum light. With this, each spectrum allows for a measurement of the phase relative to B-band maximum light for each spectrum in this subsample. We also do not consider SNe classified as Type Iax as they are proposed to originate from a different progenitor

SN Name	MJD	Phase	S/N	Wavelength Range	Reference
1980N	44584.0	-1.8	1.9	1886 - 3247	1
1980N	44586.0	0.2	1.8	1875 - 3261	1
1980N	44589.0	3.2	1.2	1883 - 3271	1
1980N	44590.0	4.2	1.8	1883 - 3239	1
1980N	44596.0	10.1	1.5	1899 - 3202	1
1980N	44597.0	11.1	1.4	1923 - 3237	1
1980N	44620.0	34.0	0.6	1899 - 3240	1
1981B	44672.0	1.0	3.8	1910 - 3213	1
1981B	44673.0	2.0	2.2	1891 - 3261	1
1981B	44674.0	2.9	2.5	1862 - 3298	1
1986G	46556.0	10.5	0.7	1995 - 3348	1
1986G	46558.0	12.5	1.8	1939 - 3257	1
1986G	46562.0	16.5	1.4	1923 - 3286	1
1986G	46565.0	19.5	1.9	1873 - 3326	1
1986G	46569.0	23.5	1.5	1907 - 3270	1
1989A	47643.0	83.8	11.6	3450 - 9000	2
1989B	47572.0	7.5	211.6	3450 - 8450	3
1989B	47578.0	13.5	12.1	3450 - 7000	3
1989B	47643.0	78.3	56.3	3300 - 9050	3
1989B	47717.0	152.1	14.1	3900 - 6226	3
1989B	47558.0	-6.5	2.6	1226 - 3348	1
1989M	47716.0	2.5	221.1	3080 - 10300	2

Table 2.1: Full spectral sample. **References**: (1) Foley et al. (2008b); (2) Silverman et al. (2012a); (3) Wells et al. (1994a); (4) Filippenko et al. (1992a); (5) Ruiz-Lapuente et al. (1993); (6) Matheson et al. (2001); (7) Filippenko et al. (1992c); (8) Unknown; (9) Blondin et al. (2012a); (10) Ruiz-Lapuente et al. (1997); (11) Patat et al. (1996a); (12) Salvo et al. (2001); (13) Li et al. (1999); (14) Li et al. (2001b); (15) Cappellaro et al. (2001); (16) Modjaz et al. (2001); (17) Gal-Yam et al. (2003); (18) Li et al. (2001a); (19) Valentini et al. (2003); (20) Krisciunas et al. (2011); (21) Leonard et al. (2005a); (22) Benetti et al. (2004); (23) Elias-Rosa et al. (2008); (24) Li et al. (2003); (25) Jha et al. (2006b); (26) Pignata et al. (2008); (27) Kotak et al. (2005); (28) Elias-Rosa et al. (2006a); (29) Stanishev et al. (2007); (30) Anupama et al. (2005); (31) Folatelli et al. (2013a); (32) Leonard (2007b); (33) Wang et al. (2009a); (34) Garavini et al. (2007); (35) Chornock et al. (2006); (36) Phillips et al. (2007); (37) Foley et al. (2010); (38) Thomas et al. (2007); (39) Hicken et al. (2007); (40) Östman et al. (2011); (41) Wang et al. (2008a); (42) Yamanaka et al. (2009); (43) Simon et al. (2007); (44) Zhang et al. (2010); (45) Silverman et al. (2011); (46) Pan et al. (2018); (47) McCully et al. (2014); (48) Foley et al. (2009a); (49) Foley & Kirshner (2013a); (50) Pereira et al. (2013a); (51) Mazzali et al. (2014a); (52) Amanullah et al. (2015); (53) Pan et al. (2015b); (54) Foley et al. (2016c) (This table is available in its entirety in a machine-readable form in the online journal. A portion is shown here for guidance regarding its form and content.)

Property	Number of SNe
t_{max} (B)	444
Redshift	773
$\Delta m_{15}(B)$	274
$\Delta m_{15}(B)$ from fit parameter	97
A_V	314
Host Morphology	525
M_B	120
$B - V$	120
Velocity at Max m_B	290
Carbon Presence	193
Hubble Residual	149

Table 2.2: The main queryable spectral and photometric properties of the SNe included in the database. We also include but do not list additional metadata from Hicken et al. (2009) and Betoule et al. (2014).

scenario (103 spectra of 13 SNe Iax); (Foley et al. 2013). Since the reddening caused by host-galaxy dust causes the relative strengths of spectral features and overall continuum to change, we restrict our sample again to SNe Ia where we can correct for this effect using MLCS reddening parameters (Jha et al. 2007). These requirements limit us to 3485 spectra of 305 SNe Ia for our analysis. From here on this sample will be referred to as our "nominal" sample.

Some of the characteristics of the nominal sample are shown in Figure 2.3. All SNe in the sample are at low-redshift (median $z = 0.02$), vary greatly in their light-curve shapes ($0.68 \leq \Delta m_{15}(B) \leq 2.09$ mag), and occur in a diversity of host environments. For SNe Ia without an explicit measurement of $\Delta m_{15}(B)$, we estimate $\Delta m_{15}(B)$ based on its power-law relationships with SALT, SALT2 and MLCS31 shape parameters (Figure 2.4). s, x_1, and Δ are taken from tables 1, 2, and 3 of Hicken et al. 2009. We also include Δ estimates from another set of MLCS fits using $R_V = 2.5$ (Jha et al. 2007). For SNe that have been fit by more than one of these methods, we determine $\Delta m_{15}(B)$ from the

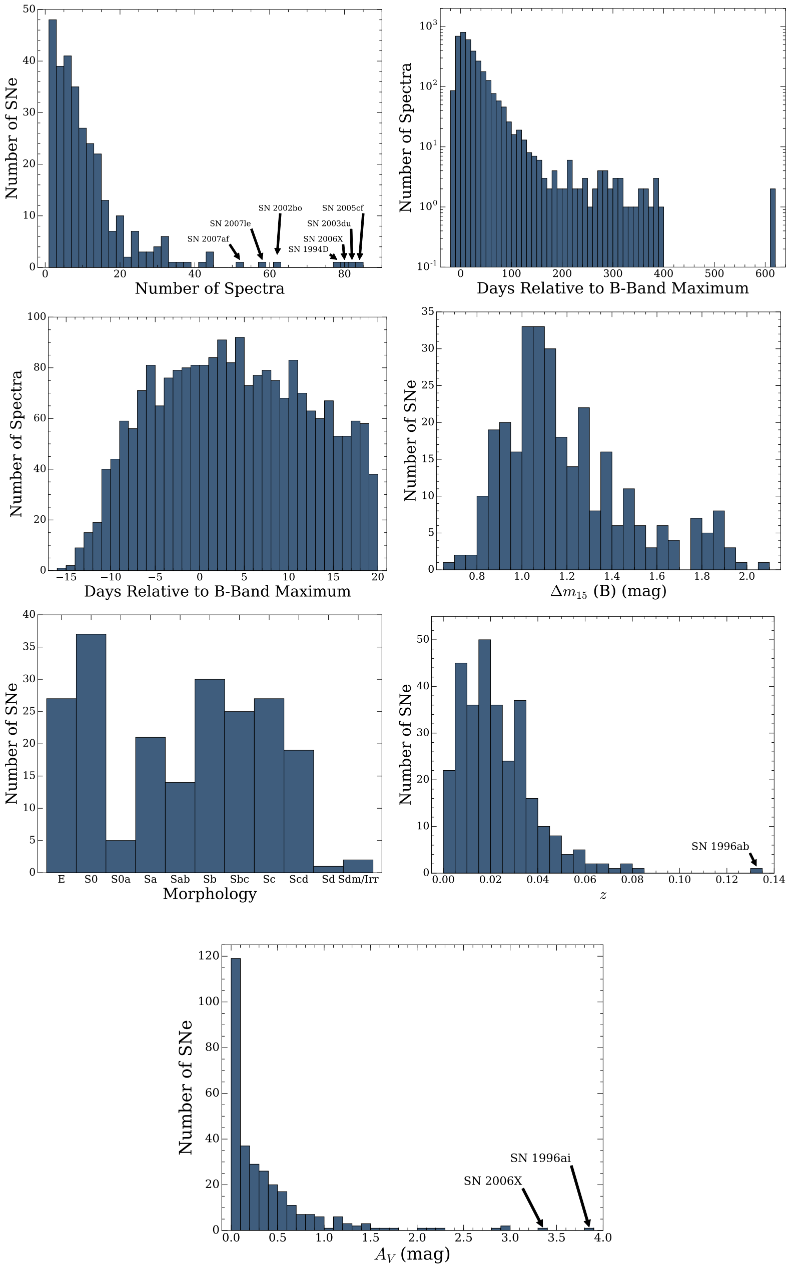

Figure 2.3: From top-left to bottom-right: Histograms of the number of individual spectra per SN, the number of individual SN spectra at each epoch, the number of individual SN spectra at each epoch within 20 days of maximum brightness, the number of SNe Ia per $\Delta m_{15}(B)$ bin, the number of SNe Ia per bin in host galaxy morphology, the number of SNe Ia per redshift bin, and the number of SNe Ia per host-galaxy extinction bin in the nominal sample.

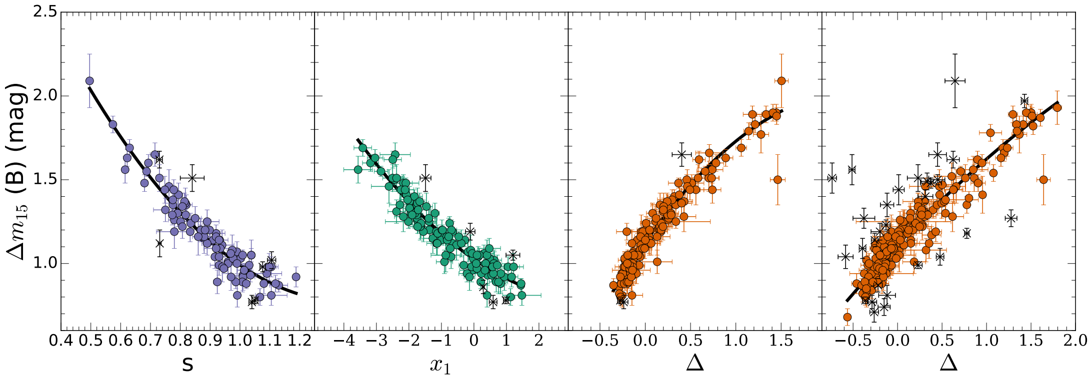

Figure 2.4: Power-law relationships between $\Delta m_{15}(B)$ and the light-curve shape parameters s (SALT; *first*), x_1 (SALT2; *second*), Δ (MLCS using $R_V = 3.1$; *third*), and Δ (MLCS using $R_V = 2.5$; *fourth*). We use these relationships to determine an estimate of $\Delta m_{15}(B)$ when there is no explicit measurement available. In all panels, points marked with a black "x" are 3-σ outliers and are not included when fitting the relation.

power-law relationship with the lowest on outlier fraction and RMS uncertainty. Using a consistent sample of 85 SNe among fitting methods, we estimate the outlier fractions of SALT, SALT2, MLCS31, and MLCS25 to be 0.082, 0.035, 0.024, and 0.071 respectively, and the RMS uncertainties to be 0.071, 0.066, 0.070, and 0.074 respectively. Thus, we choose to give MLCS31 highest priority, followed by SALT2, SALT, and then MLCS25 for determining $\Delta m_{15}(B)$ from a given light-curve shape parameter.

2.3 Data Homogenization

The heterogeneous nature of spectral observations and reduction techniques has been a significant barrier to studying the bulk properties of SN Ia spectra across multiple sources. We have developed a framework to process SN spectra in order to facilitate analyses of large data sets. Prior to storing a spectrum in the database, several steps are taken to ensure homogeneity. These processing steps are applied to every spectrum in the database in addition to the nominal sample.

2.3.1 Variance Spectrum Generation

For many spectra, we do not have a corresponding variance spectrum. We illustrate the procedure we use to generate an approximate variance spectrum in Figure 2.5. First, we create a smoothed spectrum using the inverse-variance Gaussian smoothing algorithm from Blondin et al. 2006. In this work, Blondin et al. 2006 define a "smoothing factor" ($d\lambda/\lambda$) that accounts for the intrinsic broadening of spectral features due to the large expansion velocities. Since our spectra vary greatly in S/N, one value of $d\lambda/\lambda$ is not sufficient to adequately smooth every spectrum. Using a sample of spectra with varying S/N, we empirically determined the best value of $d\lambda/\lambda$ for each spectrum. We fit a linear function of S/N to these data:

$$d\lambda/\lambda = \begin{cases} 0.0045 & S/N < 2.5 \\ 4.61 \cdot 10^{-3} - 4.52 \cdot 10^{-5} * S/N & 2.5 \leq S/N \leq 80 \\ 0.001 & S/N > 80 \end{cases}$$

We apply constant values of $d\lambda/\lambda$ at the extremes of our S/N range to prevent over-/under-smoothing of the data. The yellow curve in the left panel of Figure 2.5 shows a smoothed spectrum of SN 2005lz using this method. We then subtract the smoothed spectrum from the original spectrum (blue curve), take the absolute value, and smooth again using $d\lambda/\lambda = 0.015$ (orange curve in right panel). We account for possible uncertainty from sky emission by scaling a template sky emission spectrum to to our

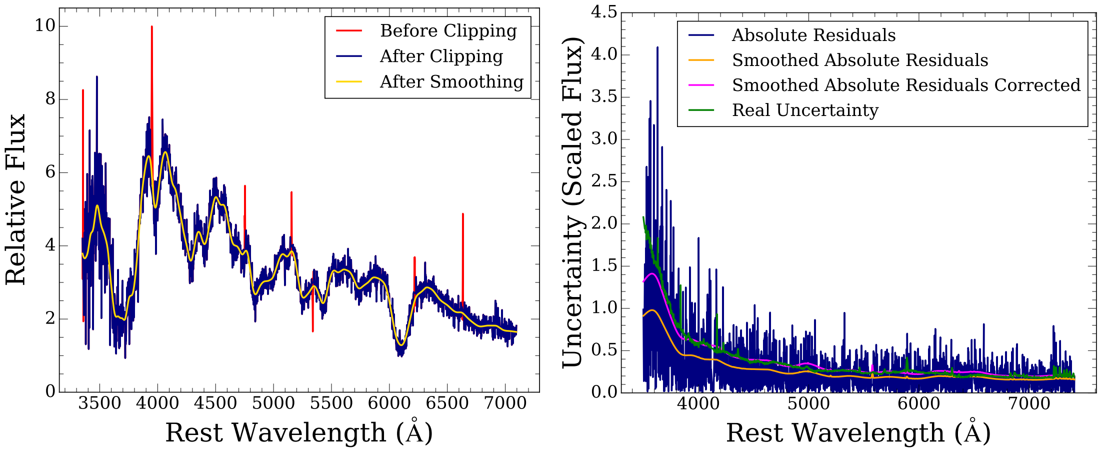

Figure 2.5: (*left*): Spectra SN 2005lz before (red curve) and after (blue curve) removing unwanted features using the method described in section 2.3.2. The smoothed spectrum (with $d\lambda/\lambda = 0.004$; yellow curve) is used to estimate a preliminary uncertainty in order to determine the clipping threshold. (*right*): Uncertainty spectra corresponding to the spectrum of SN 2005lz. The blue curve is the absolute residual spectrum from the difference between the clipped spectrum and the smoothed spectrum, the green curve is the real uncertainty spectrum from the CfA archive, the yellow curve is the smoothed absolute residual spectrum, and the pink curve is the same spectrum after applying a small scaling in order to better match the green curve.

smoothed absolute residual spectrum, multiplying by a constant factor, and adding this to our smoothed absolute residual spectrum. We chose a value for the constant factor that provides a reasonable match to the uncertainty due to sky emission seen in the CfA spectra.

We compare the generated approximate uncertainty spectra to the associated uncertainty spectra of the CfA sample. We find that we consistently underestimate the uncertainty of the CfA sample at bluer wavelengths (see Figure 2.5, right panel). To quantify this effect, we divide every CfA uncertainty spectrum by the uncertainty spectrum that we generate from the flux. We then fit a linear function of wavelength to each of these ratio spectra. For spectra without archival uncertainty spectra, we apply the mean fit as a wavelength-dependent scaling to each uncertainty spectrum in order to account for this discrepancy. After making this scaling correction, we obtain an uncertainty spectrum (pink curve) that closely matches the CfA uncertainty spectrum (green curve), especially at bluer wavelengths.

2.3.2 Removal of Residual Sky Lines, Cosmic Rays, and Galaxy Emission Lines

We attempt to remove any residual night sky lines, cosmic ray hits, and host-galaxy emission lines that are still present. We generate a smoothed absolute residual spectrum via the same method in Section 2.3.1. We interpolate the flux and the variance over regions where the residual spectrum exceeds this smoothed residual spectrum by $>5\sigma$, where σ is the local scatter obtained from the variance spectrum. We also increase the threshold for clipping of negative residuals to 10σ in regions where absorption lines from Ca H&K, Na I D, K I $\lambda7687$, and the 5780 Å diffuse interstellar band may exist. The effects of this method are shown in Figure 2.5. The narrow emission features (red) have been removed resulting in the blue curve.

2.3.3 Reddening Corrections, Deredshifting, and Re-binning

We correct each flux and variance spectrum for MW-reddening using the Schlafly and Finkbeiner reddening map (Schlafly & Finkbeiner 2011), a Fitzpatrick 1999 (F99) reddening law, and $R_V = 3.1$. We then deredshift the spectrum, rebin at equally spaced wavelength values ($\Delta\lambda = 2$ Å) using a flux-conserving interpolation algorithm, and store the re-binned spectrum in the database. Since interpolation introduces unwanted correlation in our variance spectra, we scale our original variance spectrum to the rebinned variance spectrum. When available, we use MLCS reddening parameters to correct for the distortion introduced by host-galaxy reddening. Since there is a larger degree of uncertainty associated with this step, the non-corrected spectra are stored in the database and we perform this correction during our analysis.

2.4 Generating Composite Spectra

The large sample necessitates a reliable way to visualize and validate the data and our processing techniques. Composite spectra provide a reasonable solution to this problem. They attempt to provide the "most representative" average of a given subset of data. We use this tool to reproduce the known spectral trends in SNe Ia in order to verify that our sample is of high quality. By maximizing S/N and reducing the impact of outliers, composite spectra make it easy to analyze the differences between complex spectral feature shapes. This is an advantage over measurements of derived quantities from individual spectra like velocities, EWs, and line ratios, which significantly reduce the available information and may only apply to a subset of the data (e.g., not all spectra have obvious carbon absorption).

We show that composite spectra in combination with relational queries with `kaepora` provide for a fast means of validating known relationships and testing different hypotheses. We always find it useful to follow up potential trends seen in composite spectra with an analysis of the individual underlying spectra.

Here we describe our method for generating composite spectra from subsets of our nominal sample. The basic algorithm is adapted from the methods used in Foley et al. 2008a and Foley et al. 2012a. Reference these works for a more detailed description of the potential systematic errors introduced using these techniques. We require $A_V < 2$ for each SN included in the composite spectra generated for this work.

2.4.1 Algorithm

When combining spectra from a subsample of SNe, we make an effort to ensure that the selected sample of SNe are representative of their respective populations. Multiple spectra from a single SN may satisfy a given query and in this case, we first create individual inverse-variance weighted composite spectra for each of these SNe using the methods described below. If a spectrum does not overlap with any other spectra from the same SN we attempt to add it in during the next step (if there is still no overlap, the spectrum is ignored). Once the set of spectra (now including combined spectra) is selected, we scale the flux of all spectra to the flux of the spectrum with the largest wavelength range (the preliminary template spectrum) by minimizing the sum over wavelength of the absolute differences between each spectrum and this template spectrum. A new template spectrum is then created by averaging these spectra weighted by their inverse variance (or taking the median). Spectra in the original sample that did not have overlap with the largest wavelength spectrum may potentially overlap with this new template spectrum. This process is repeated until all possible spectra are included in the composite spectrum. The 50 Å at the beginning and end of each spectrum are ignored when constructing composite spectra in order to suppress any systematic errors that frequently occur in these regions.

It is often the case that one or a few high-S/N spectra will strongly influence the overall continuum and spectral features of the composite spectrum. This is a larger problem for smaller sample sizes where the median may be a more appropriate representation of the underlying spectra. Highly unequal weight distributions also tend to cause discontinuities in the composite spectrum at wavelengths where highly weighted spectra end. These issues can be resolved by assigning equal weights to each spectrum at the expense of S/N of the composite spectrum. We re-weight using Gini coefficients to mitigate this issue. This solution is a middle-ground approach that avoids discontinuities while attempting to still maximize S/N.

In this case, the Gini coefficient is used to measure how much the distribution of weight deviates from complete equality. It ranges from 0 to 1, where 0 means complete equality and 1 means complete inequality. Therefore in the context of combining spectra, a Gini coefficient of 0 indicates equal weight given to each spectrum (i.e., the average) and a gini coefficient of 1 indicates that a single spectrum carries all of the weight. Equation 2.1 defines the Gini coefficient as half of the relative mean absolute difference. For our purposes, w_i represents the total weight (sum of inverse variance) given to an individual spectrum in some wavelength range, and N is the number of spectra contributing to the composite spectrum in that same wavelength range.

$$G = \frac{\sum_{i=1}^{N}\sum_{j=1}^{N}|w_i - w_j|}{2N\sum_{i=1}^{N} w_i} \tag{2.1}$$

We separate the composite spectrum into 1000 Å regions and measure G. If $G > 0.6$ in

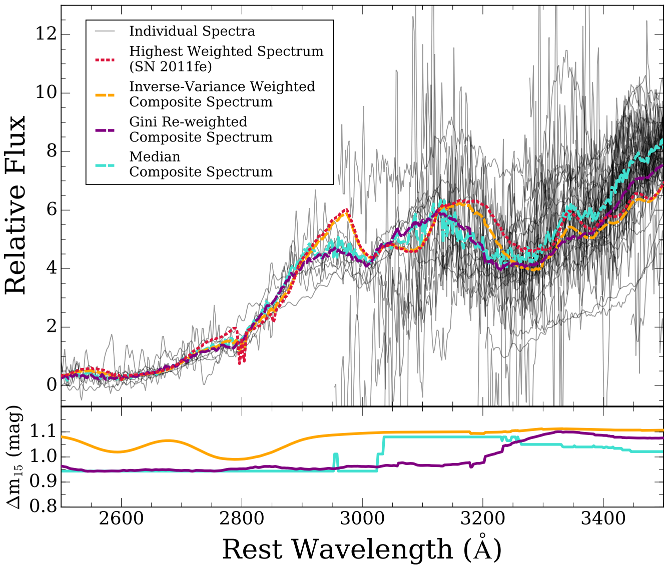

Figure 2.6: (*top panel*): Composite spectra generated from a subsample (black curves) using different methods. The red dashed curve is a high S/N spectrum of SN 2011fe. This spectrum carries the most weight in this wavelength range. The cyan curve is the median composite spectrum, the yellow curve is the inverse-variance weighted composite spectrum, and the purple curve is the Gini-weighted composite spectrum. The Gini-weighted composite spectrum is less influenced by SN 2011fe than the inverse-variance weighted composite spectrum while maintaining a larger S/N that the median composite spectrum. (*bottom panel*): The average value of $\Delta m_{15}(B)$ as a function of wavelength for each composite spectrum.

any of these wavelength bins, we subsequently de-weight the individual spectrum that carries the most weight across its whole wavelength range by a constant factor. This process is iterated until $G < 0.6$ in all wavelength bins. We chose a value of $G < 0.6$ as our threshold because it tends to provide a reasonable compromise between the average and the inverse-variance weighted average. This method allows us to achieve better S/N in our composite spectrum than the average without a strong bias towards the highest S/N spectra. This tends to result in a smooth composite spectrum that is more representative of the underlying data.

We demonstrate the effects using different methods to construct composite spectra in Figure 2.6. Here we have generated composite spectra from a sample of 180 spectra of 82 total SNe. These spectra have phase between -4 and 0 days and $\Delta m_{15}(B)$ < 1.25 mag. The black curves are individual spectra (or combined spectra from the same SN) of varying S/N, the red dashed curve is a high-S/N spectrum SN 2011fe, and the other colored curves are composite spectra generate from these individual spectra using three different methods; medianed (cyan), inverse-variance weighted (yellow), and "Gini-weighted" (purple). As expected, the inverse-variance weighted composite spectrum (yellow curve) is strongly influenced by the high S/N spectrum of SN 2011fe. We find that the median composite spectrum works well in this wavelength range and the Gini-weighted composite spectrum is consistent with the median, but with higher S/N. We also see that as N increases, the properties of the Gini-weighted composite spectrum approach the inverse-variance weighted composite spectrum. The average gini coefficients of the inverse-weighted composite spectrum and the Gini-weighted composite spectrum in this wavelength range are 0.86 and 0.57 respectively. The effective value of $\Delta m_{15}(B)$ for our Gini-weighted composite spectrum is consistent with the median at wavelengths <2950 Å and then smoothly approaches the inverse-variance weighted value as N increases. This is expected since SN 2011fe carries less overall weight as more spectra contribute to each weighted composite spectrum. Since we have demonstrated that Gini-weighted composite spectra are more reliable for sample sizes that vary with wavelength, the composite spectra presented in this work are constructed using this method unless specified otherwise.

2.4.2 Uncertainty of Composite Spectra

To understand the subtle differences between composite spectra we need an estimate of the uncertainty at each wavelength. We implement a bootstrap resampling with replacement algorithm in order to estimate the variation about the average spectrum.

Although not completely independent, the bootstrapping uncertainty is different from the root-mean-square error (RMSE) in several ways. The bootstrapping method assumes that the given sample probes the diversity of the underlying population. This diversity is manifested in the bootstrapping uncertainty by taking random resamples of the original set of spectra. This means that composite spectra with high S/N can still have large bootstrapping uncertainty if the underlying population is diverse. Therefore, the bootstrapping uncertainty provides information about the reproducibility of the average spectrum. The RMSE is typically smaller than the bootstrapping uncertainty and less affected by the diversity of the underlying population. At any given wavelength, the bootstrapping uncertainty may be estimated from the full distribution (and therefore asymmetric about the average spectrum) while the RMSE is defined as being symmetric about the average spectrum.

The uncertainty that we observe is a combination of several effects. The blue end of our composite spectra are primarily dominated by the intrinsic variation of the sample which increases towards the UV (Foley et al. 2008c), Poisson noise because we have fewer spectra contributing to the average, and the typically low detector responses in this region. We correct the continuum for host-galaxy extinction using an estimate of A_V from an MLCS2k2 fit (Jha et al. 2007). Since we normalize our spectra by minimizing absolute differences in the overlap region with the template spectrum (see Section 2.4.1), we effectively normalize near 5000 Å on average. Therefore, spectra with anomalous continua can cause more scatter farther away from this central wavelength. Since host-galaxy extinction corrections modify the continua of our spectra, we expect that the uncertainty at the red end of a composite spectrum is dominated by imperfect corrections for reddening.

2.4.3 Example Composite Spectrum

In Figure 2.7 we present a Gini-weighted composite spectrum constructed from 142 maximum-light spectra ($-1 < \tau < +1$ days, and $\Delta m_{15}(B) < 1.8$ mag) of 96 SNe Ia. This composite spectrum has an average phase of 0.11 days, an average $\Delta m_{15}(B)$ = 1.11 mag, and an average $z = 0.013$. In the first panel, the blue curve is the relative flux and the blue-shaded region is the 1σ bootstrap resampling region. Our composite spectrum covers a wavelength range where we require at least 5 contributing SNe. We exclude the fastest declining events ($\Delta m_{15}(B) < 1.8$ mag) because their continua are often far redder than the rest of the sample. Overall, the flux and the average properties of our maximum-light composite spectrum are very similar to those of a normal SN Ia.

The second panel contains the 1σ bootstrap contours divided by the relative flux of the composite spectrum. This fractional uncertainty is largest below 3200 Å. The uncertainty also gradually increases redward of ∼6000 Å. The fractional uncertainty is smallest between these regions because this is both the region where most spectra overlap, and the region where most spectra are effectively normalized. There is a slight

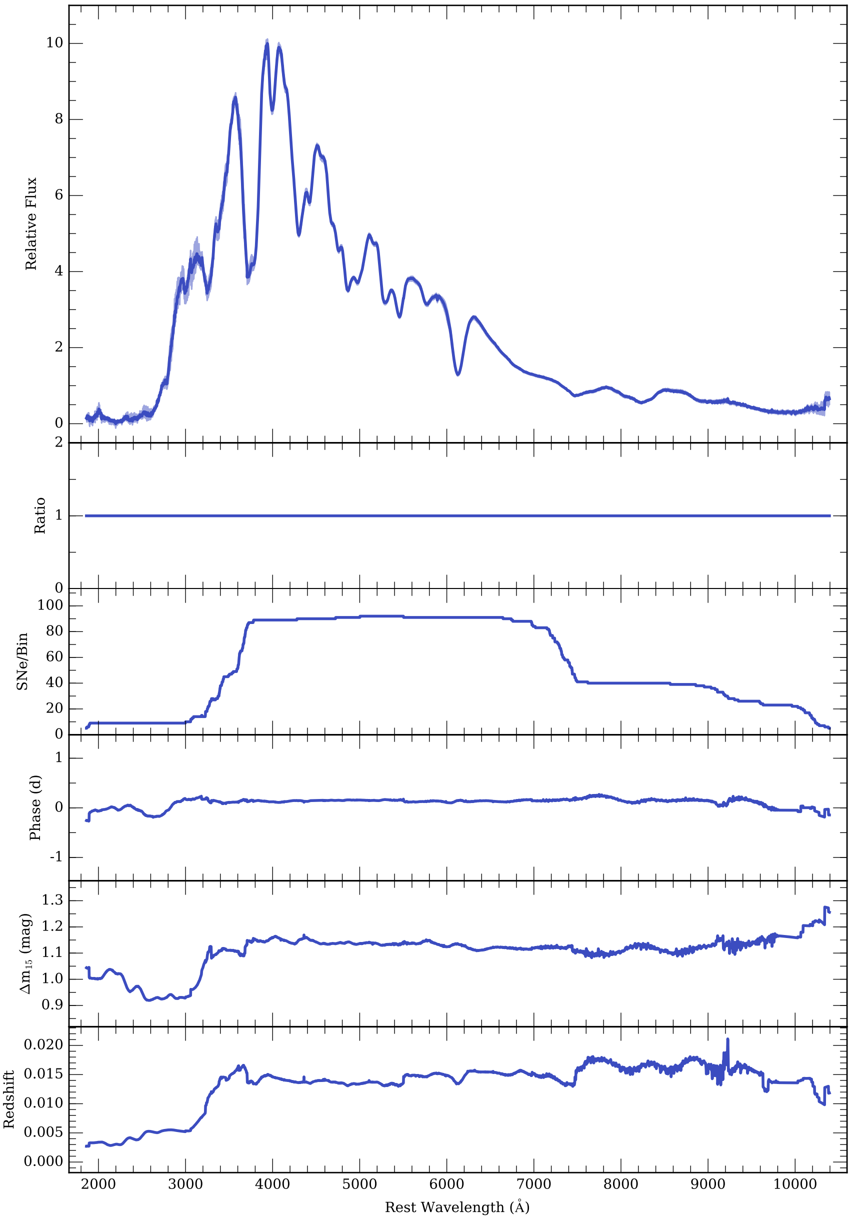

Figure 2.7: (*first panel*): Maximum-light composite spectrum created from our nominal sample consisting of spectra from 145 spectra of 96 SNe ($-1 < \tau < +1$ days, and $\Delta m_{15}(B) < 1.8$ mag). The light-blue region is the 1σ bootstrap sampling uncertainty. (*second panel*): The light-blue region is the ratio of the 1σ bootstrap sampling uncertainty relative to the composite spectrum. (*third panel*): The number of individual spectra contributing to each wavelength bin. For this composite spectrum, a minimum of 5 and a maximum of 96 spectra contribute at any given wavelength. (*fourth panel*): The average phase relative to maximum brightness as a function of wavelength for this composite spectrum. (*fifth panel*): The average value of $\Delta m_{15}(B)$ as a function of wavelength for this composite spectrum. (*sixth panel*): The average redshift of the composite spectrum as a function of wavelength.

correlation of the fractional uncertainty with the Si II and Ca II absorption features. This correlation is likely caused by the variability of line velocities in the underlying sample.

Since the wavelength ranges of individual spectra can vary greatly, the number of contributing events varies with wavelength. The third panel of the figure shows the number of SNe contributing to the composite spectrum as a function of wavelength. Since the CfA could obtain spectra frequently, it is more likely that to have spectra within a small phase window than other surveys. Therefore, a large portion of this subsample are spectra obtained with the FAST spectrograph. This instrument has a wavelength coverage of $\sim$3700 – 7600 Å (Fabricant et al. 1998). Thus the number of spectra contributing to the composite spectrum reaches its maximum in this wavelength range.

Additionally, since the variance of individual spectra vary with wavelength, the average properties of composite spectra can change with wavelength. Panels 4 – 6 of Figure 2.7 show the variation of phase, $\Delta m_{15}(B)$, and redshift with wavelength. There is a large shift in the average properties from the UV to the optical part of our composite spectrum. This change is due to the fact that UV spectra tend to be from intrinsically bright and nearby events. Overall, there is not much variation in these average properties in the optical, but there does seem to be some slight correlation with the stronger spectral features. It is also important to note our maximum-light composite spectrum is subject to Malmquist bias. However, analyses of subsamples with comparable $\Delta m_{15}(B)$ should not be as heavily impacted by this effect.

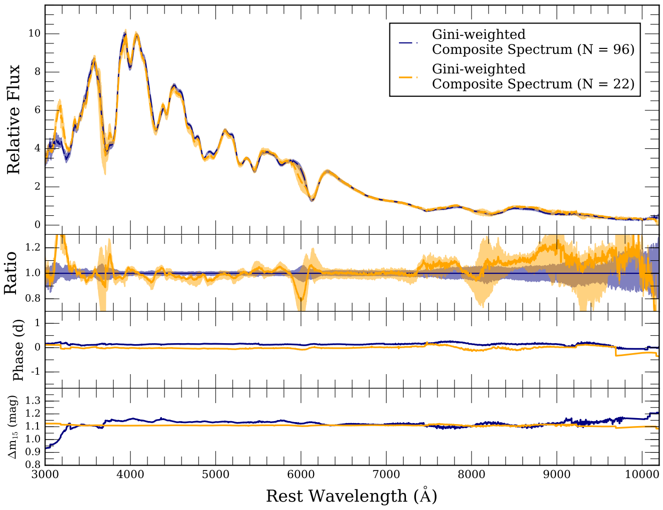

Figure 2.8: (*first panel*): The maximum-light composite spectrum from Figure 2.7 (blue curve) compared to a maximum-light composite spectrum constructed from a subsample of 15 SNe Ia with $-1 < \tau < +1$ days and $1.05 < \Delta m_{15}(B) < 1.15$ mag (yellow curve). The shaded regions are the 1σ bootstrap sampling uncertainties of the respective composite spectra. (*second panel*): The ratio of the given composite spectra and 1σ bootstrap sampling regions to the larger sample size composite spectrum. (*third panel*): The average phase relative to maximum brightness as a function of wavelength for a given composite spectrum. (*fourth panel*): The average value of $\Delta m_{15}(B)$ as a function of wavelength for a given composite spectrum.

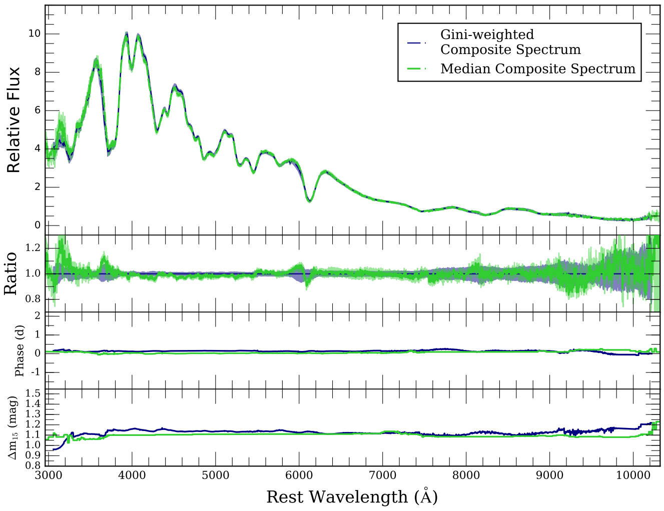

Figure 2.9: A comparison between Gini-weighted composite spectra and median composite spectra constructed from the subsample of 96 SNe Ia with $-1 < \tau < +1$ days and $\Delta m_{15}(B) < 1.8$ mag (blue and green curves respectively). The panel format is the same as Figure 2.8.

We find that composite spectra with similar average properties tend to look remarkably similar regardless of sample size. In Figure 2.8 we compare our maximum-light composite spectrum ($N = 96$; blue curve) to a maximum-light composite spectrum constructed from a smaller sample of SNe ($N = 22$) with the same average phase and $\Delta m_{15}(B)$ ($-1 < \tau < +1$ days and 1.05 $<\Delta m_{15}(B) <$ 1.15 mag). This composite spectrum has an average phase of 0.13 days, an average $\Delta m_{15}(B) = 1.09$ mag, and an average $z = 0.015$. These properties are very similar to those of the composite spectrum constructed with a larger $\Delta m_{15}(B)$ window. Most of the differences are captured by the 1σ bootstrap uncertainty regions and the largest differences occur in regions where the average light curve shapes differ between composite spectra (∼3200 Å).

We also compare these Gini-weighted maximum-light composite spectra to median composite spectra generated from the same subsamples (Figure 2.9). Generally, the Gini-weighted composite spectrum is very similar to the corresponding median composite spectrum at all wavelengths and has higher S/N. The small differences tend occur at the large spectral features. The most discrepant regions are the Si II and Ca II absorption features, however the differences are consistent with the 1σ bootstrap uncertainty region of the Gini-weighted composite spectrum and vice versa.

2.5 Results and Analysis

In this section, we use `kaepora` to generate subsets of our nominal sample with desirable average properties. We present composite spectra generated using our Gini-weighting method from these subsets that vary primarily with phase and light-curve shape. We demonstrate that our composite spectra reproduce known correlations between spectral and photometric properties. We obtain composite spectra with desired properties by making cuts on the certain parameter ranges. We often refer to this process as "controlling for" a specific parameter. Finally, we investigate the spectral variation of SNe Ia residing in different host-galaxy environments.

We compare our results to four sets of SN Ia template spectra and their respective color curves. The template spectra come from Nugent et al. (2002), Stern et al. (2004), Hsiao et al. (2007), Guy et al. (2007), and Foley et al. (2008a) and will be referred to as the Nugent/Nugent-91T/Nugent-91bg, Hsiao, SALT2, and Foley template spectra respectively. These template spectra were developed with different scientific goals in mind. It is also important to note that the spectral samples used in constructing these spectral templates will inevitably overlap with some of the data in our nominal sample. It is difficult to know exactly which data are shared between template spectra, but we still expect to find similar results because of this overlap.

The Nugent and Hsiao template spectra were created for the purpose of determining K-corrections for samples of SNe Ia. The Nugent template spectra are solely dependent on phase and use only local SNe Ia. The Nugent template spectra are heavily influenced by SNe 1989B, 1992A, and 1994D. One of which has strong dust reddening (SN 1989B; Wells et al. 1994b) and another of which has anomalous luminosity and colors (SN 1994D; Richmond et al. 1995; Patat et al. 1996b). We include the Nugent template spectra in our comparisons but acknowledge that significant discrepancies may be caused by the weight of these atypical SNe.

The Hsiao template spectra improve on the method for constructing spectral templates and provide a phase dependent spectral sequence for normal SNe Ia. The number of spectra contributing to these epochs ranges from 16 spectra at 85.6 days to 71 spectra at 0 days. Additionally, the spectral library used to construct these template spectra included a sample of high-z SNe Ia. The total sample included 576 spectra of 99 SNe at $z < 0.2$ and 32 spectra of 32 SNe at $z > 0.2$ (Hsiao et al. 2007). While small compared to the total sample, the high-z sample is restricted in phase and light-curve shape greatly influences the UV region of the Hsiao template spectra. The colors of the Hsiao template spectra are set to match the B-band template light curve from Goldhaber et al. (2001) and the UVR-band template light curves from Knop et al. (2003).

SALT2 was developed to improve distance estimates of SNe Ia. This light-curve fitter models the evolution of the mean spectral energy distribution (SED) of SNe Ia along with its variation with light-curve shape and color (Guy et al. 2007). We are interested in improving our understanding of this multi-dimensional spectral surface with our composite spectra. The SALT2 model also makes use of high-z SN data in order to constrain the UV continuum. In the sections below we compare the properties of our composite spectra to version 2.4 of the SALT2 spectral sequence model.

The Foley template spectra were created to investigate the potential evolution of SNe Ia with redshift. The methods for constructing our composite spectra are similar to this work and make use of inverse-variance weighting to produce composite spectra. These composite spectra vary with phase, light-curve shape, and redshift.

2.5.1 Evolution of Phase-binned Composite Spectra

We first examine the spectral evolution of our composite spectra. In Figure 2.10, we present 62 phase-binned composite spectra with phase ranging from -11.2 to $+270.5$ days. This set of composite spectra represents all of the spectra in our nominal sample. The time of maximum light of each SN is likely the largest source of error on phase (typical uncertainty 0.5 days), therefore we do not assume that our composite spectra can differentiate spectral features with sub-day precision. We require a minimum bin size of 1 day and expand the size of the phase bin as needed as we probe later epochs. We require a minimum of 20 individual SNe per composite spectrum. We also require at least 5 spectra per wavelength bin and thus these composite spectra have differing wavelength ranges. For clarity, the 1σ bootstrap uncertainty regions and other composite spectrum properties are are not displayed. However, each of these composite spectra can be decomposed in a similar way to our maximum-light composite spectrum in Figure 2.7.

The spectral features evolve smoothly with time and clearly show how the average SN Ia transitions from its photospheric phase, dominated by absorption from intermediate mass elements (IMEs), to the nebular phase, which is dominated by forbidden emission from iron-group elements (IGEs). There is a slight tendency to see small discontinuities near the edges of the composite spectra where N is small and near $\sim$7600 Å (the red end of the CfA sample's wavelength coverage). The overall effect on the continuum is small and most often captured by the bootstrapping uncertainty region. Our composite spectra are comprised of spectra coming from a diversity of

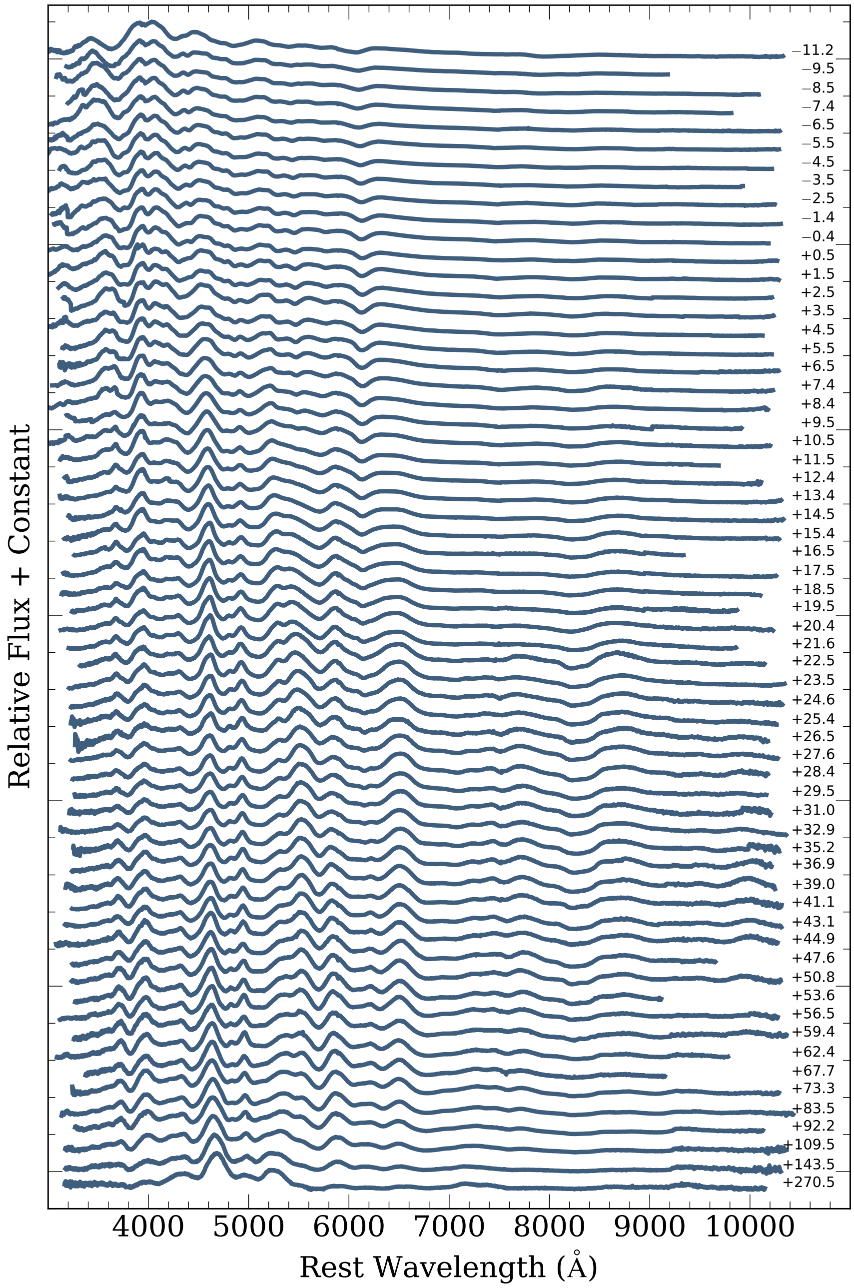

Figure 2.10: Composite spectra generated from the nominal sample showing the time evolution of spectral features of SNe Ia. A time series is plotted with effective phases of $t = -11.3$ to $t = 271.2$ days relative to B maximum brightness. Minimum bin sizes of 1 day are enforced near maximum brightness. Bin sizes are adjusted accordingly at later epochs to include a statistically significant ($N \geq 20$) sample for each composite spectrum.

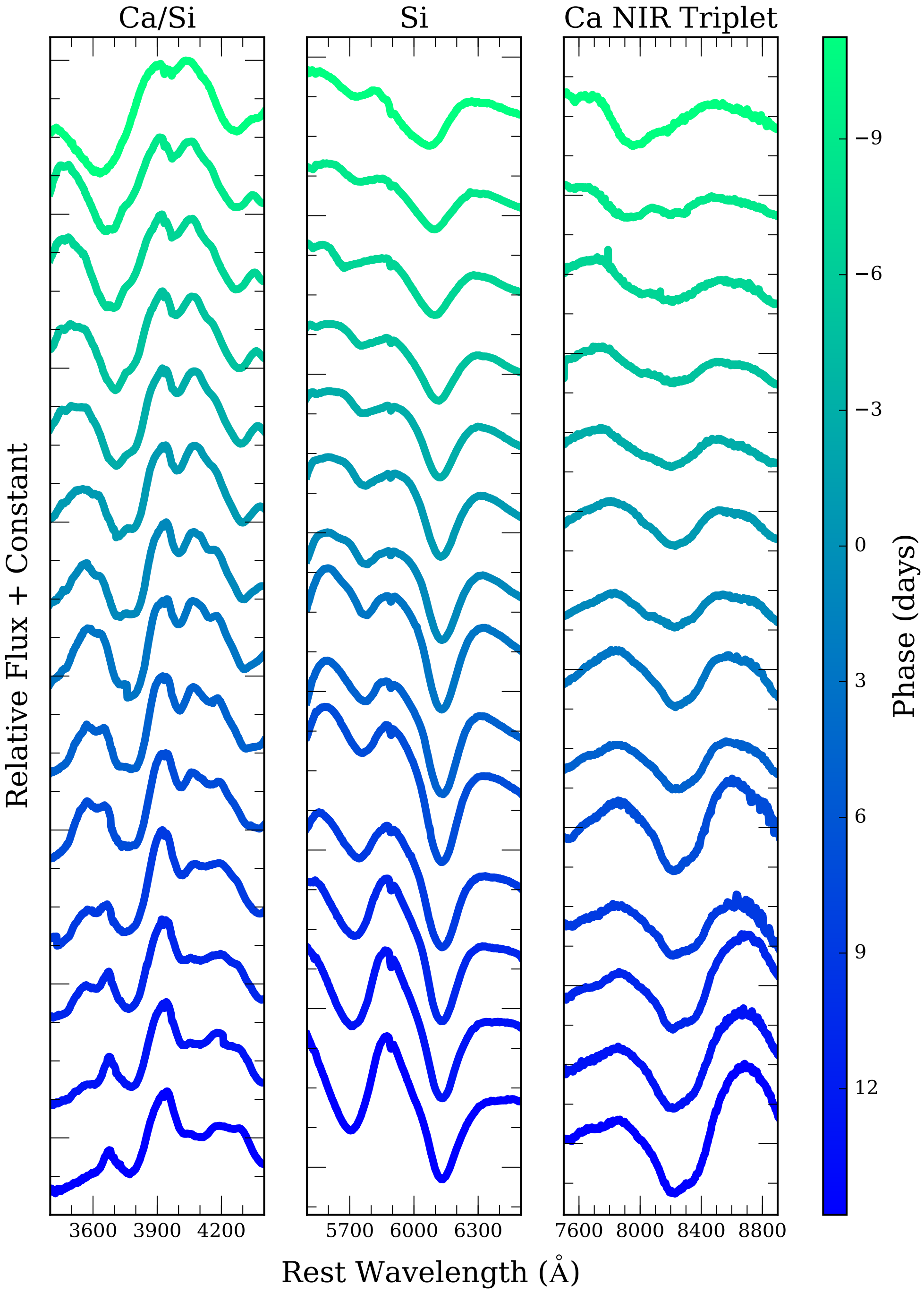

Figure 2.11: Zoomed-in composite spectra within 16 days of maximum light created from the nominal sample. The spectral absorption features associated with Ca II H&K, Si II, and the Ca II NIR triplet are shown in the left, middle and right panels respectively. Bin sizes of 2 days are used for each of these composite spectra.

events, therefore, at any specific phase normal selection biases will apply. In particular, composite spectra for later phases are more likely to be influenced by intrinsically bright events.

In Figure 2.11, we present 16 phase-binned composite spectra ranging from -11 days relative to maximum light to 16 days after maximum light using a bin size of 2 days. The Si II and Ca II absorption features evolve smoothly with time indicating a steady change in photospheric velocity. The minima of these features progress towards redder wavelengths indicating a smooth decrease in velocity with time.

Beyond MW and host galaxy extinction corrections, we do not make any modifications to the continua of our composite spectra. The $B-V$ color evolution of these composite spectra is very similar to that of normal SNe Ia. This similarity means that the relative flux calibration among different surveys is good enough to produce reliable mean continua.

In Figure 2.12, we show the $B-V$ color evolution of our composite spectra with $\Delta m_{15}(B) < 1.8$ mag (red squares) and compare to the Nugent (cyan), Hsiao (yellow), and SALT2 template spectra (black) for phases ranging from -12 to $+56$ days. We also investigate the effects of binning our composite spectra with $1.05 \leq \Delta m_{15}(B) \leq 1.25$ mag (dark blue stars). We chose this bin size for $\Delta m_{15}(B)$ since the Hsiao and Nugent template spectra were created to represent $s = 1.0$ ($\Delta m_{15}(B) \approx 1.1$ mag) SNe, and the SALT2 base template spectrum has $x_1 = 0$ ($\Delta m_{15}(B) \approx 1.1$ mag). Thus our sets of composite spectra with large and small $\Delta m_{15}(B)$ windows have average values of $\Delta m_{15}(B)$ that range from $1.03 - 1.17$ mag and $1.07 - 1.11$ mag respectively. This

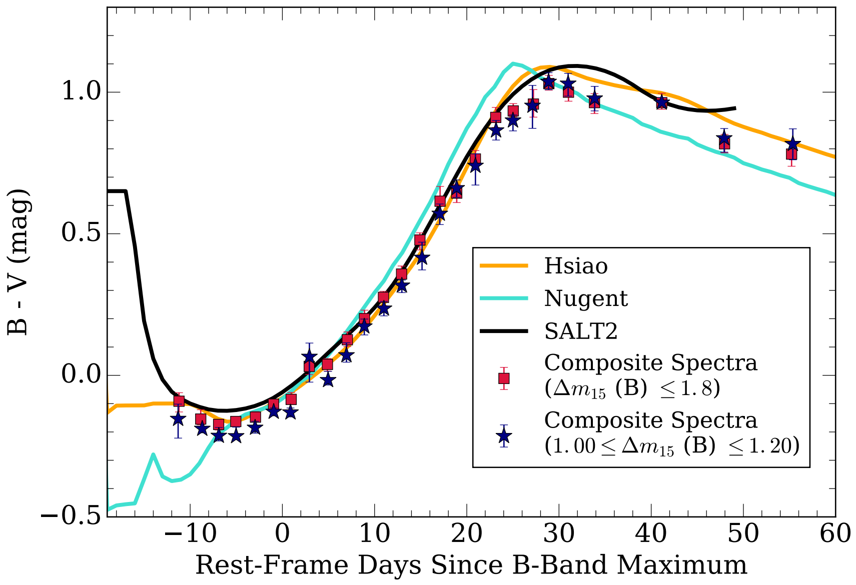

Figure 2.12: Comparison of the $B-V$ color evolution of various SN Ia template spectra and our composite spectra created from the nominal sample. The orange, light-blue, and black curves are the Hsiao, Nugent, and SALT2 template spectra respectively. The red squares are color measurements from composite spectra generated from the nominal sample with $\Delta m_{15}(B) < 1.8$ mag. The blue stars are color measurements from composite spectra generated from the nominal sample using only SNe where $1.00 \leq \Delta m_{15}(B) \leq 1.20$ mag. Bin sizes of 2 days are used for phase $\leq$+30 days and bin sizes of 4 days are used for phase >+30 days.

means that on average these two sets of composite spectra have very similar light curve shapes.

Overall, we see good agreement with the the three template spectra. We also find that our two sets of composite spectra with different $\Delta m_{15}(B)$ windows are consistent at all phases. This further reinforces the fact our composite spectra with larger sample sizes (due to having larger ranges of light curve shape) are representative of SNe Ia with the average properties of our underlying samples. On average, our composite spectra are most consistent with Hsiao and slightly bluer than the SALT2 and Nugent color curves. The slope of the Nugent template spectrum between the epochs of -6 and $+24$ days is significantly larger than the other color curves. This difference may be due to the influence of atypical SNe on the Nugent template spectrum. Both the Hsiao and Nugent spectral templates are warped to match the photometry of template light curves in the literature (Hsiao; B-band Goldhaber et al. 2001, UVR-band Knop et al. 2003, Nugent; B-band Riess et al. 1999, RI-band Knop et al. 2003). Our composite spectra reproduce a normal SN Ia $B - V$ color curve without the need for spectral warping and thus preserve absorption features, lines ratios, and velocities that are representative of the underlying spectra.

Si II λ6355 line velocities measured from these composite spectra are also representative of their respective subsets. In Figure 2.13, we compare the velocity evolution of our composite spectra (black) to the distributions of velocities of the individual SNe in each phase bin (distinguished by color) covering phases between -13 and $+16$ days. We also compare to the velocity evolution of the median velocity measurement in each phase range (brown), and median composite spectra generated from the same subsets (orange).

The velocities of our composite spectra are consistent with these measurements across all phases and range from a blueshift of $-13{,}700$ km s^{-1} at -11 days to $-10{,}700$ km s^{-1} at $+15$ days. The velocities of our weighted mean and median composite spectra steadily decline with phase until around maximum light where they level off at $\sim -10{,}800$ km s^{-1}. Due to the lack of data at very early epochs (< -10 days), it is likely that the velocity of our composite spectrum is slightly underestimated at this phase.

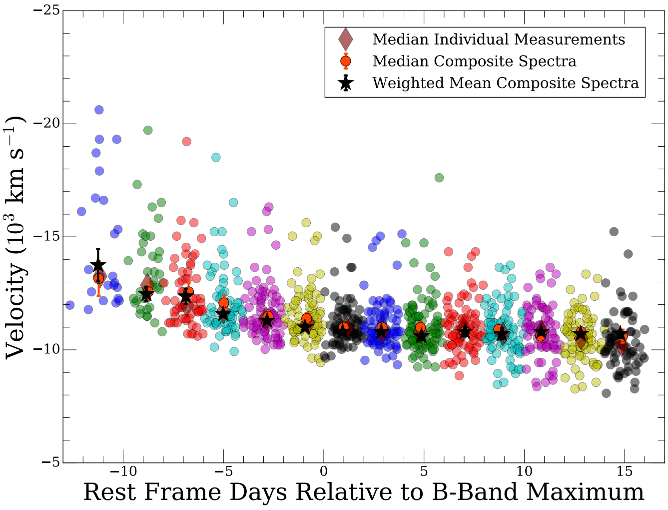

Figure 2.13: Velocity evolution of our composite spectra created from the nominal sample. Black stars are measurements from the weighted mean composite spectra and orange circles are measurements from median composite spectra. The smaller circle points are measurements from the individual spectra. These are color coded to distinguish the borders of the phase bins defined for the composite spectra. The brown diamonds correspond to the median of the individual measurements within each bin.

2.5.2 Maximum-Light $\Delta m_{15}(B)$-binned spectra

We also examine luminosity-dependent spectral differences through the light-curve decline rate parameter $\Delta m_{15}(B)$ for events near maximum light. In Figure 2.14 we present 6 maximum light composite spectra where we have controlled for light-curve shape. Here we expand our phase range to include spectra with phase between -3 and $+3$ days. We require at least 5 spectra per wavelength bin which results in varying wavelength ranges among the composite spectra. Since there are more UV spectra for slow-declining events that tend to have higher luminosities, we are able to extend two of these composite spectra into the UV.

This subdivision by $\Delta m_{15}(B)$ clearly demonstrates several known spectral sequences with light-curve shape. In particular the continua become redder with narrower

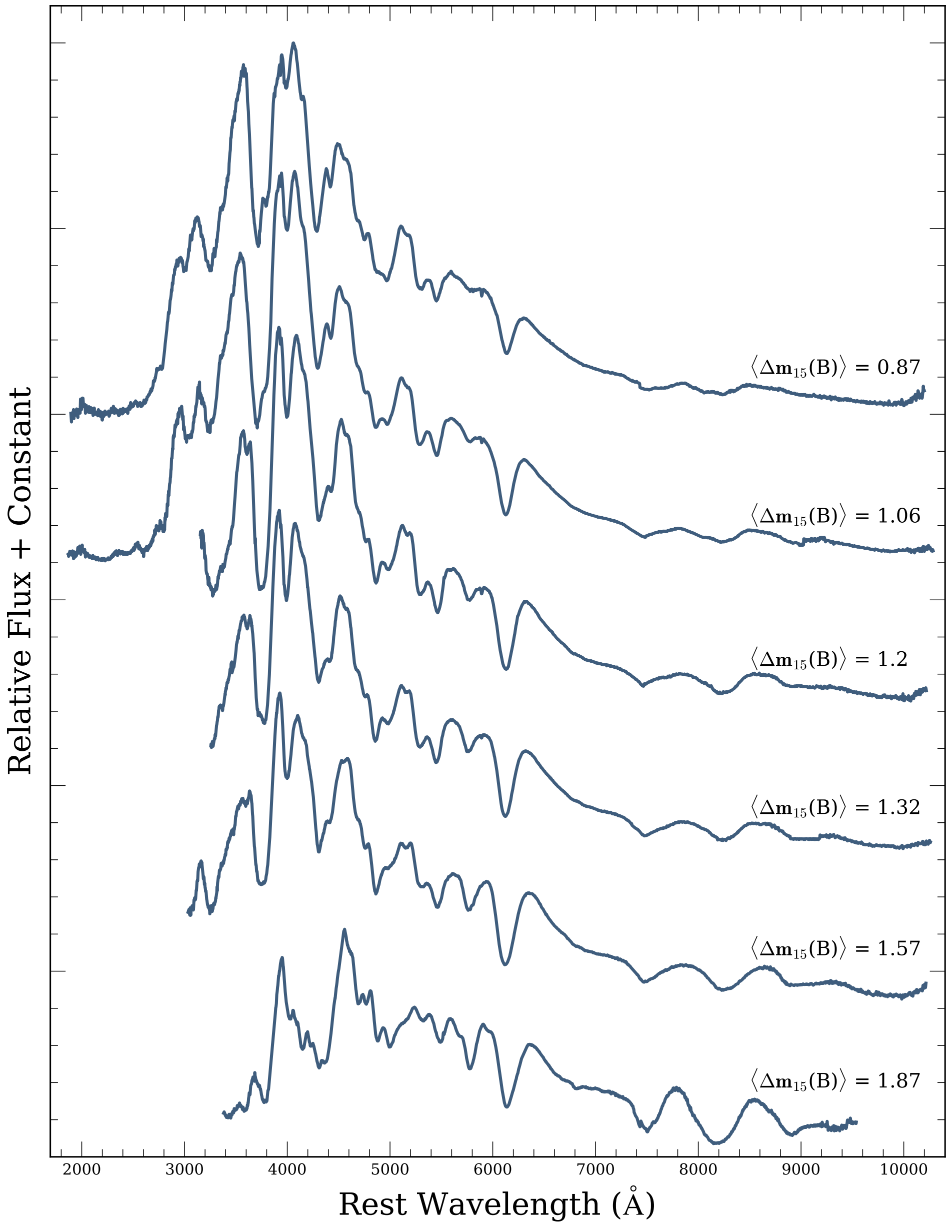

Figure 2.14: $\Delta m_{15}(B)$-binned maximum-light composite spectra. From top to bottom the spectra has $\Delta m_{15}(B)$ bins of $\Delta m_{15}(B) < 0.95$ mag, $0.95 < \Delta m_{15}(B) < 1.15$ mag, $1.15 < \Delta m_{15}(B) < 1.25$ mag, $1.25 < \Delta m_{15}(B) < 1.42$ mag, $1.42 < \Delta m_{15}(B) < 1.7$ mag, and $\Delta m_{15}(B) > 1.7$ mag. Phase bins of $-3 < \tau < +3$ days were used for each composite spectrum. The composite spectra consist of 30, 61, 16, 23, 21, and 13 individual SNe respectively. The average $\Delta m_{15}(B)$ for each composite spectrum is shown above each spectrum.

light-curves (larger $\Delta m_{15}(B)$). We also see clear evidence of Ti II absorption at ~4300 Å in the lowest luminosity composite spectrum ($\Delta m_{15}(B) = 1.87$ mag). This is a characteristic feature of the SN 1991bg-like subclass of SNe Ia (Filippenko et al. 1992b; Leibundgut et al. 1993) and is expected for these faster declining events. This composite spectrum also has stronger O I λ7773 and Ca near-IR triplet absorption than the other composite spectra.

We measure the $B - V$ colors of our composite spectra from Figure 2.14 and present them in the left panel of Figure 2.15 (blue stars). For comparison, we show measurements made from maximum-light SALT2 template spectra with effective $\Delta m_{15}(B)$ corresponding to the mean values of $\Delta m_{15}(B)$ from our composite spectra (black circles), a linear fit of this relationship from Phillips et al. (1999) (green curve), and the relationship that is produced by the MLCS2k2 model (Jha et al. 2007; orange curve).

While the SALT2 spectral feature strengths differ greatly, the $B - V$ colors of the SALT2 maximum-light spectra, by design, do not vary much with light-curve shape. The $B - V$ colors of our maximum-light composite spectra slowly become redder with $\Delta m_{15}(B)$ and then change dramatically for the fastest-declining SNe. Our composite spectra are consistent with with Phillips et al. (1999) for the slower-declining SNe Ia and produce the same general trend seen in MLCS2k2. This is not surprising because we rely on an estimate of A_V from MLCS light-curve fits in order to correct individual spectra for host-galaxy extinction.

The right panel of Figure 2.15 highlights the subtle differences between the Si II λ5972 and λ6355 absorption features of $\Delta m_{15}(B)$-binned composite spectra. Here

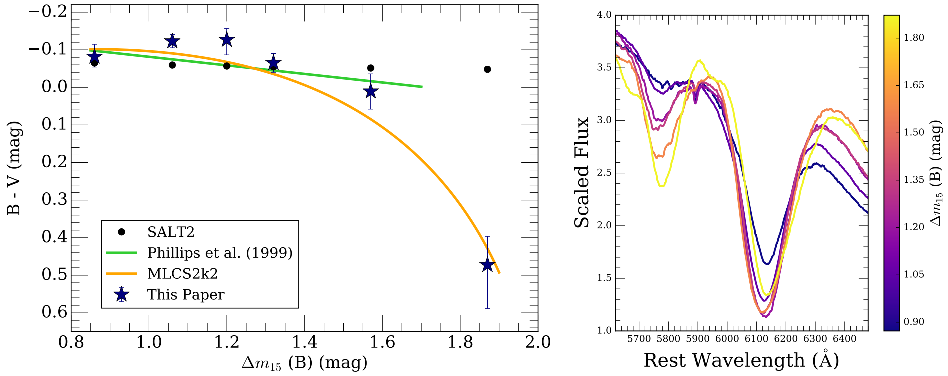

Figure 2.15: (*left*): The relationship between $\Delta m_{15}(B)$ and $B - V$ color at maximum-light. The blue stars are measurement made from our composite spectra in Figure 2.14. The black circles are measurements made from maximum-light SALT2 template spectra with effective $\Delta m_{15}(B)$ corresponding to the mean values of $\Delta m_{15}(B)$ from our composite spectra. The green and orange curves are fits from Phillips et al. (1999) and Phillips (1993) respectively. (*right*): The Si II λ5972 and λ6355 absorption features of our maximum-light composite spectra from Figure 2.14. The color bar ranges from slow-declining light-curve shapes ($\Delta m_{15}(B) = 0.86$ mag; dark purple) to fast-declining light-curve shapes ($\Delta m_{15}(B) = 1.87$ mag; yellow).

the continuum difference between these composite spectra is obvious. Since intrinsically bright SNe tend to have bluer colors, our composite spectra progress towards having redder continua as the average light-curve shape becomes narrower ($\Delta m_{15}(B)$ increases). Additionally, we see evidence of Na I D absorption in all composite spectra except the two with the largest effective $\Delta m_{15}(B)$ values. This trend is likely because fast-declining SNe Ia tend to occur in early-type environments devoid of gas (Hamuy et al. 2000; Howell 2001).

From the slowest-declining to fastest-declining composite spectra (top to bottom in Figure 2.14) the Si II λ6355 line velocities of these composite spectra are −10,500, −11,000, −10,800, −11,200, −11,200, and −10,500 km s^{-1}. These measurements are consistent with the lack of an observed correlation between light-curve shape and ve-

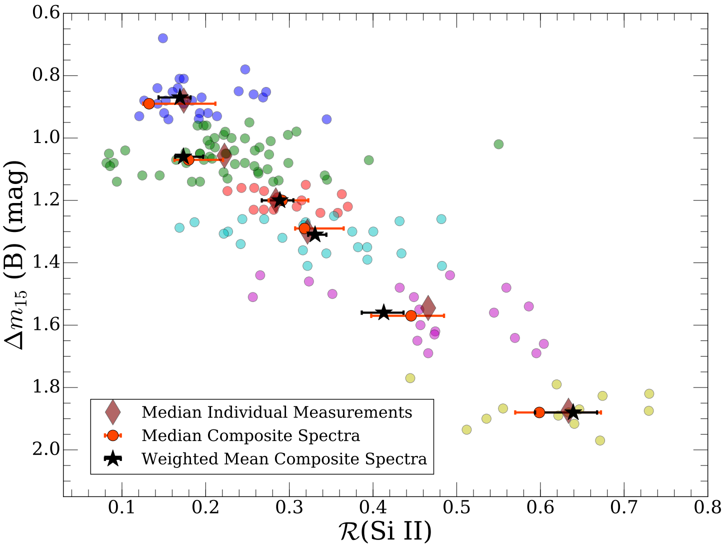

Figure 2.16: $\mathcal{R}$(Si II) of our $\Delta m_{15}(B)$-binned composite spectra created from the nominal sample. Black stars are measurements from the weighted mean composite spectra and orange circles are measurements from median composite spectra. The smaller circle points are measurements from the individual spectra. These are color coded to distinguish the borders of the phase bins defined for the composite spectra. The brown diamonds correspond to the median of the individual measurements within each bin.

locity for the bulk of SNe Ia and the tendency for events with extremely high or low values of $\Delta m_{15}(B)$ to have slightly lower velocities (Wang et al. 2009b).

In addition, the ratio of the depth of the two main Silicon absorption features ($\mathcal{R}$(Si II)) changes with light-curve shape. This sequence, originally discovered by Nugent et al. (1995), results from the changing abundance of the ionization species of Silicon (Hachinger et al. 2008). Using a similar approach to our analysis of velocity near maximum light, we compare $\mathcal{R}$(Si II) from our composite spectra (black) to those measured from the individual spectra in each $\Delta m_{15}(B)$ bin (distinguished by color; Figure 2.16). We also compare the median $\mathcal{R}$(Si II) measurement in each $\Delta m_{15}(B)$ range (brown), and $\mathcal{R}$(Si II) measured from median composite spectra generated from the same subsets (orange). Here we clearly show that $\mathcal{R}$(Si II) of a composite spectrum is representative of its effective decline rate. The measurements of $\mathcal{R}$(Si II) reproduce the properties of their underlying subsets and are consistent with the median properties of these individual spectra.

The SNe in our nominal sample span a large range of light-curve shapes and their spectra cover a large range of phases. These are the primary parameters that control the spectral features of SNe Ia and we have demonstrated that our composite spectra reproduce evolution and variation with these properties. In Figure 2.17, we present a grid of composite spectra generated by controlling for both phase and light-curve shape. From top to bottom composite spectra are increasing in their effective phase, and from left to right composite spectra are increasing in their effective $\Delta m_{15}(B)$. So the maximum-light composite spectra from Figure 2.14 are represented by the third row in this grid. For clarity we have used slightly different $\Delta m_{15}(B)$ ranges and the rightmost column contains all SNe with $\Delta m_{15}(B) > 1.50$ mag (including SNe Ia spectroscopically similar to SN 1991bg). The amount of data contributing to each composite spectrum is related to observing strategies, intrinsic brightness, and rates. For example, the composite spectrum for bins with $-3 < \tau < +3$ days and $0.95 < \Delta m_{15}(B) < 1.15$ mag contains the most individual spectra (61) likely because most SNe Ia are discovered near maximum brightness and normal SNe Ia ($\Delta m_{15}(B) \approx 1.1$ mag) are relatively bright and common. Despite slower declining SNe Ia ($\Delta m_{15}(B)$ < 0.95 mag) being intrinsically brighter, fewer spectra contribute to these composite spectra because the rates of these events are lower (Li et al. 2011a). Similarly, faster declining SNe Ia ($\Delta m_{15}(B) > 1.50$ mag) are both intrinsically fainter and have lower

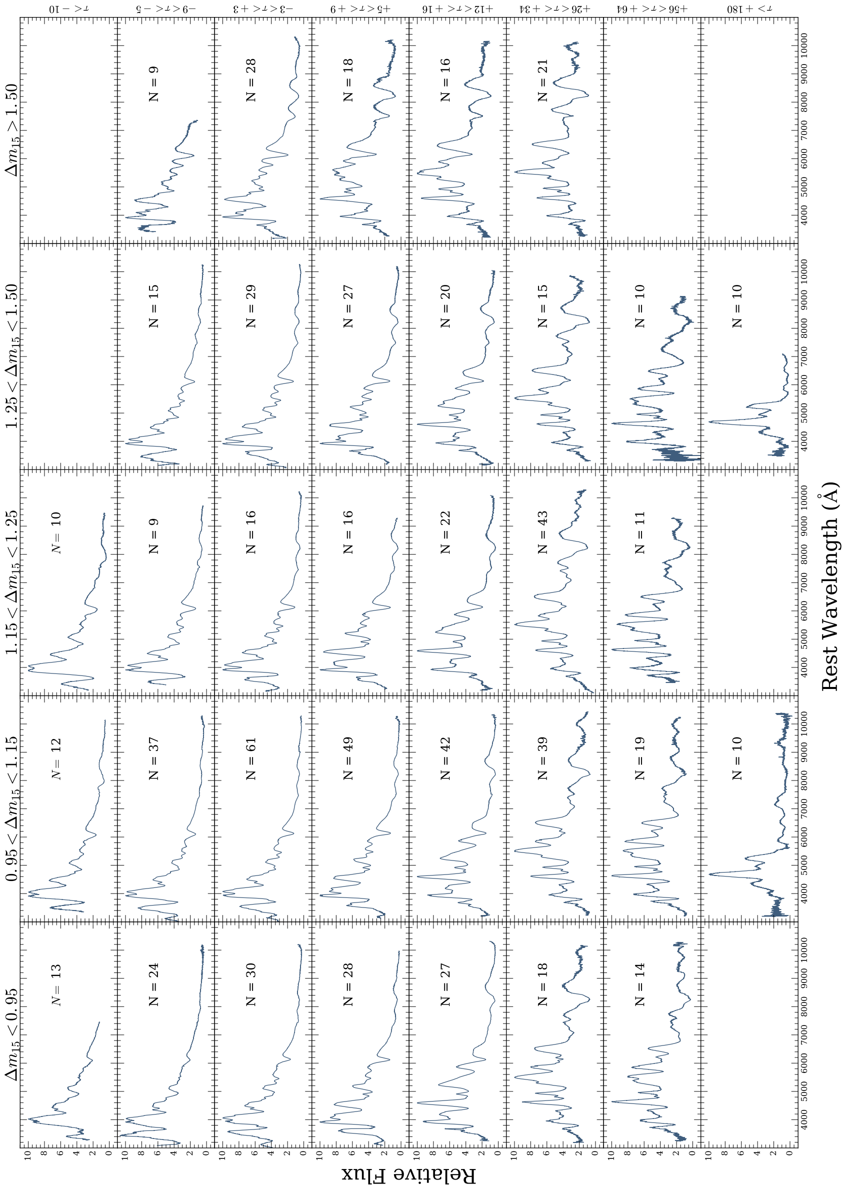

Figure 2.17: Phase and $\Delta m_{15}(B)$-binned composite spectra. Columns from left to right (rotated) correspond to $\Delta m_{15}(B)$ bins of $\Delta m_{15}(B) < 0.95$ mag, $0.95 < \Delta m_{15}(B) < 1.15$ mag, $1.15 < \Delta m_{15}(B) < 1.25$ mag, $1.25 < \Delta m_{15}(B) < 1.5$ mag, and $\Delta m_{15}(B) > 1.5$ mag.. Rows from top to bottom (rotated) corresponds to phase bins of $\tau < -10$ days, $-9 < \tau < -5$ days, $-3 < \tau < +3$ days, $+5 < \tau < +9$ days, $+12 < \tau < +16$ days, $+26 < \tau < +34$ days, $+56 < \tau < +64$ days, and $\tau > +180$ days. The number of individual spectra included in each composite spectrum is stated in the corresponding panel. Composite spectra have varying wavelength ranges because we require at least 5 individual spectra at any given wavelength. Blank panels correspond to regions of this parameter space where we do not currently have enough data to generate a representative composite spectrum.

rates than normal SNe Ia (Li et al. 2011a). For these fast-declining events, we again see Ti II absorption at ∼4300 Å at all phases. Naturally, we also see a decrease in the number of spectra with phase as the SNe dim and get more difficult to observe.

This figure also highlights some spectral correlations that are slightly degenerate with both phase and light-curve shape. As expected, the continua of our composite spectra are bluer for earlier phases and smaller values of $\Delta m_{15}(B)$ and redder for later phases and larger values of $\Delta m_{15}(B)$. This continuum relationship is consistent with Figure 2.12 which shows that the $B - V$ color of our composite spectra become redder with time for phases between -6 and $+28$ days, and Figure 2.15 which also shows the tendency for maximum-light composite spectra with larger effective $\Delta m_{15}(B)$ to have redder continua. Additionally, light-curve shape and phase produce some similar effects on spectral feature strengths. For example, the strength of the Si II $\lambda4130$ absorption feature is weaker with earlier epochs and broader light-curve shapes. The flux of the peak to the right the $\lambda4130$ absorption feature has the tendency to decrease with phase relative to the peak to the right of the Ca H&K absorption feature. A similar correlation between these peaks exists with increasing $\Delta m_{15}(B)$ near maximum light. We also observe a slight positive correlation between $\mathcal{R}$ (Si II) and phase between -11 and $+9$ days. For these reasons, some composite spectra look very similar despite having very different average properties. For example, our composite spectra constructed using $-9 < \tau < -5$ and $1.25 < \Delta m_{15}(B) < 1.5$ mag (row 2, column 4) and $+5 < \tau < +9$ and $\Delta m_{15}(B) < 0.95$ mag (row 4, column 1) have similar continua and spectral feature strengths.

2.5.3 Template Spectrum Comparisons

In this section, we compare our composite spectra to the Nugent, Hsiao, SALT2 and Foley template spectra using various bins of phase and $\Delta m_{15}(B)$.

In Figure 2.18 we investigate the normal SN Ia template spectra near maximum light. We use our total maximum-light composite ($-1 < \tau < +1$ days and $\Delta m_{15}(B)$ < 1.8 mag) spectrum from Figure 2.7 as a comparison. Overall, our composite spectrum is most similar to the Hsiao and Foley template spectra. The majority of the Hsiao anf Foley template spectra fall within the 1σ bootstrap uncertainty of our composite spectrum and the near-UV peaks blueward of 4000 Å are very well matched. Hsiao has slightly higher flux in some regions >8000 Å. The Nugent template spectrum is slightly bluer than the composite spectrum especially in the UV and near-UV. The SALT2 maximum-light ($x_1 = 0$) template spectrum has a slightly redder continuum than the composite spectrum and only extends from $2000 - 9200$ Å.

Despite the slight color differences, the relative strengths of most absorption features are very similar for our composite spectrum and the three template spectra. The Nugent template spectrum has a larger Si II λ6355 blueshift of $-$12,300 km/s in comparison to our composite spectrum ($-$10,900 km s^{-1}), Hsiao ($-$11,000 km s^{-1}), Foley ($-$11,500 km s^{-1}), and SALT2 ($-$11,300 km s^{-1}).

In section 5.1, we investigated the effect our $\Delta m_{15}(B)$ bin size on the color evolution of our composite spectra. Here we perform a similar analysis to see if spectral feature strengths differ for composite spectra with the same average properties but different sample sizes. In Figure 2.19 we compare our maximum-light composite spec-

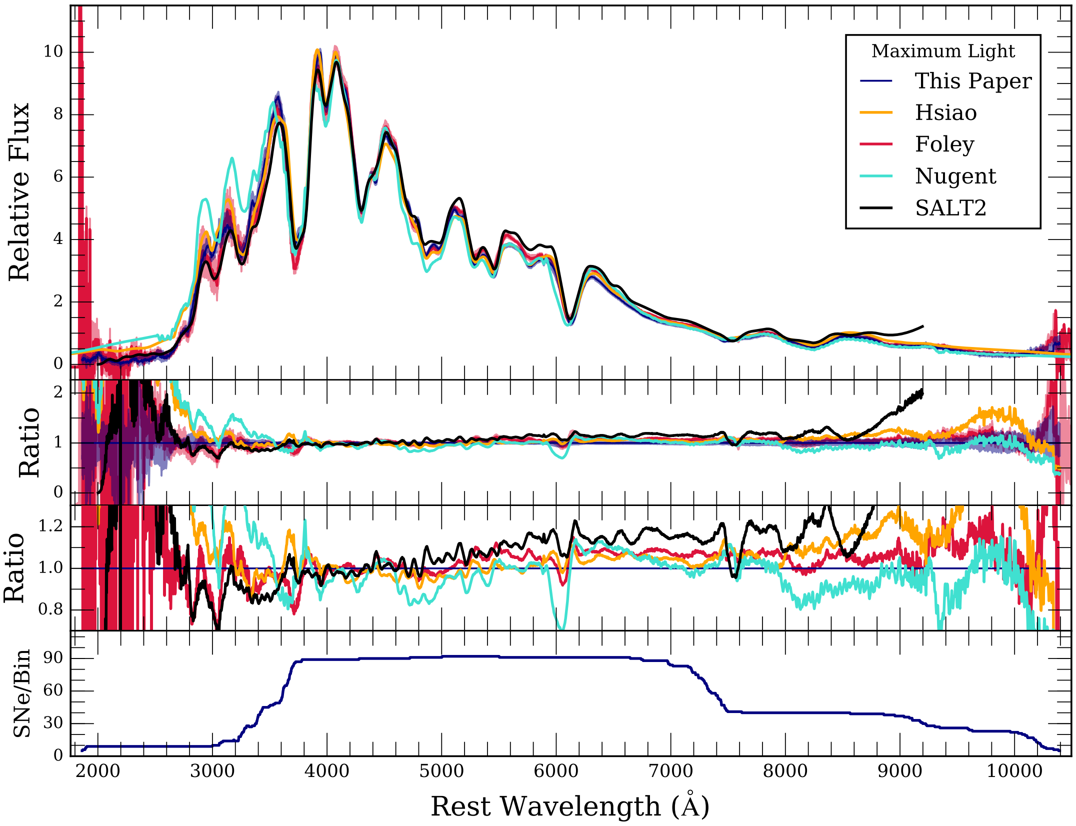

Figure 2.18: (*first panel*): Comparison of our maximum-light composite spectrum (blue curve) from Figure 2.7 to maximum-light template spectra from Hsiao (orange curve), Foley (red curve), Nugent (light-blue curve), and SALT2 (black curve). The blue- and red-shaded regions are the 1σ bootstrapping uncertainty on the composite spectra from this work and Foley respectively. (*second panel*): The ratio as a function of wavelength of a given template spectrum to our maximum-light composite spectrum. (*third panel*): Zoomed in version of the second panel to emphasize smaller differences between template spectra. The light-blue shaded region is the 1σ bootstrap variation of the total maximum-light composite spectrum. (*fourth panel*): The number of individual spectra contributing to each wavelength bin of the total maximum-light composite spectrum.

.

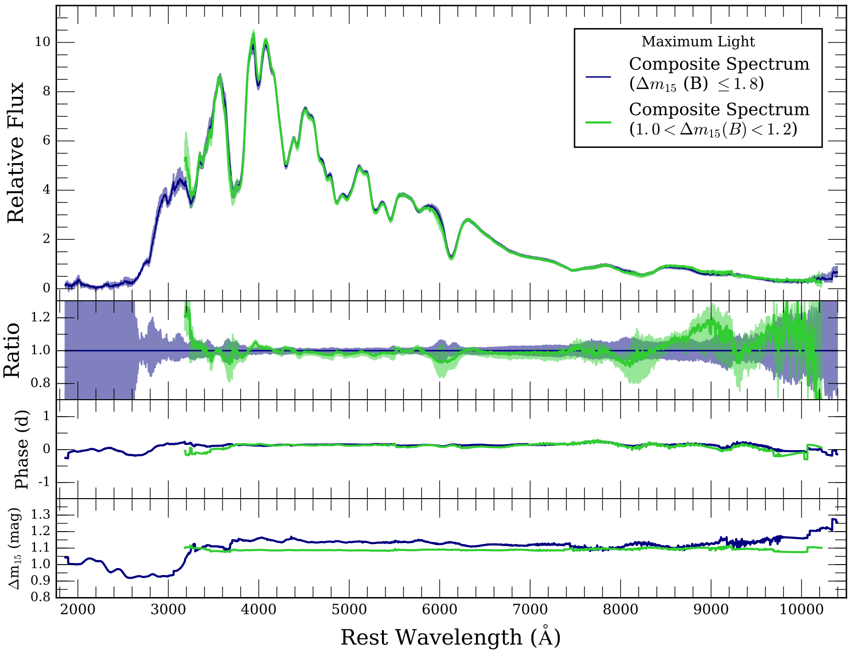

Figure 2.19: Same format as Figure 2.8 except we compare our maximum-light composite spectrum (blue curve) from Figure 2.18 and our maximum-light composite spectrum with $1.0 < \Delta m_{15}(B) < 1.2$ mag (green curve).

trum with $\Delta m_{15}(B) < 1.8$ (blue curve) to our maximum-light composite spectrum with $1.0 < \Delta m_{15}(B) < 1.2$ mag (green curve). The latter composite spectrum was constructed from 51 spectra of 34 SNe. The differences between this composite spectrum and our maximum-light composite spectrum with $\Delta m_{15}(B) < 1.8$ (blue curve) are very small. There does seem to be larger variation near the stronger spectral features, but these differences are all captured by the bootstrapping uncertainty. We also see that the average phase and $\Delta m_{15}(B)$ are very similar in the wavelength range where these composite spectra overlap. For these reasons, we elect to use our composite spectra constructed from larger sample sizes when comparing to other template spectra of normal SNe Ia.

Figures 2.20, 2.21 and 2.22 compare our composite spectra to the Nugent, Hsiao, SALT2, and Foley template spectra at different epochs (~ -1 week, $\sim +1$ week, and $\sim +1$ month respectively). The line velocities of these composite spectra are well matched by the SALT2 template spectra. We measure a Si II λ6355 blueshift of $-12{,}600$ km s^{-1} for our -1 week composite spectrum ($-11{,}700$ km s^{-1}, $-12{,}100$ km s^{-1}, $-11{,}500$ km s^{-1}, and $-12{,}700$ km s^{-1} for the -1 week Hsiao, Foley, Nugent, and SALT2 template spectra respectively). Similarly, we measure a Si II λ6355 blueshift of $-10{,}800$ km s^{-1} for our +1 week composite spectrum ($-10{,}900$ km s^{-1}, $-11{,}000$ km s^{-1}, $-10{,}600$ km s^{-1}, and $-10{,}800$ km s^{-1} for -1 week Hsiao, Foley, Nugent, and SALT2 template spectra respectively). At every epoch, our composite spectra best match the spectral features and continua of the Hsiao and Foley template spectra. Additionally, the SALT2 template spectra have redder continua than our composite spectra at every epoch. The largest differences tend to occur near the stronger spectral features such as Si II λ6355 and the Ca II NIR triplet. Finally, our +1 month composite spectrum is significantly bluer than the other template spectra.

We also compare SN Ia template spectra with maximum-light composite spectra for both slow and fast declining events. In Figure 2.23 we present our composite spectrum constructed using only slow-declining events ($\Delta m_{15}(B) < 0.90$ mag). For this comparison, we warp the Hsiao maximum-light ($\Delta m_{15}(B) = 1.1$ mag) template spectrum to match the B, V, and R-band photometry of the composite spectrum. We also compare to the Foley $\Delta = -0.27$ ($\Delta m_{15}(B) = 0.90$) template spectrum, the Nugent-91T template spectrum (Stern et al. 2004), and the SALT2 model spectrum for an

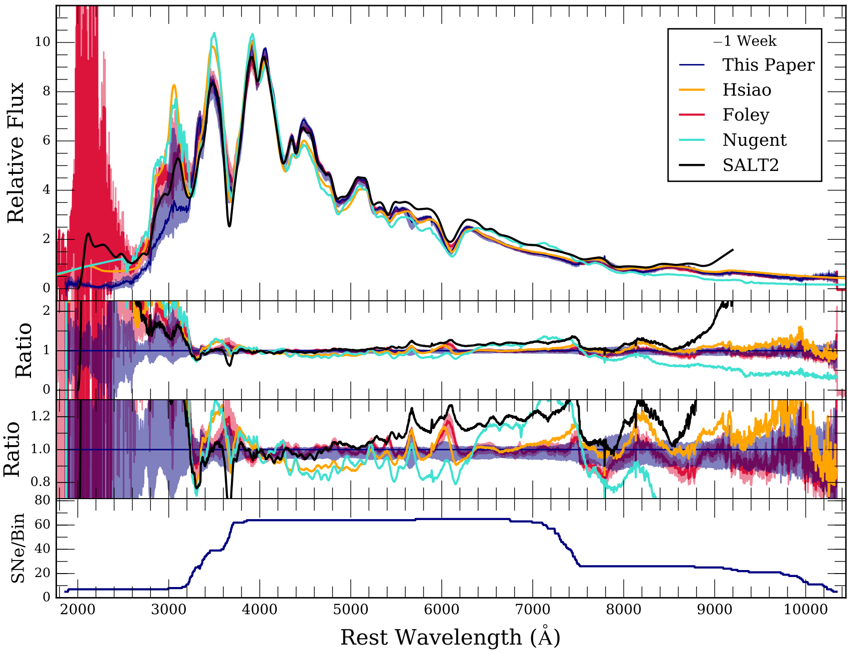

Figure 2.20: Same as Figure 2.18 except the composite spectrum (blue curve) is constructed using a phase bin of $-8 < \tau < -6$ days and $\Delta m_{15}(B) < 1.8$ mag.

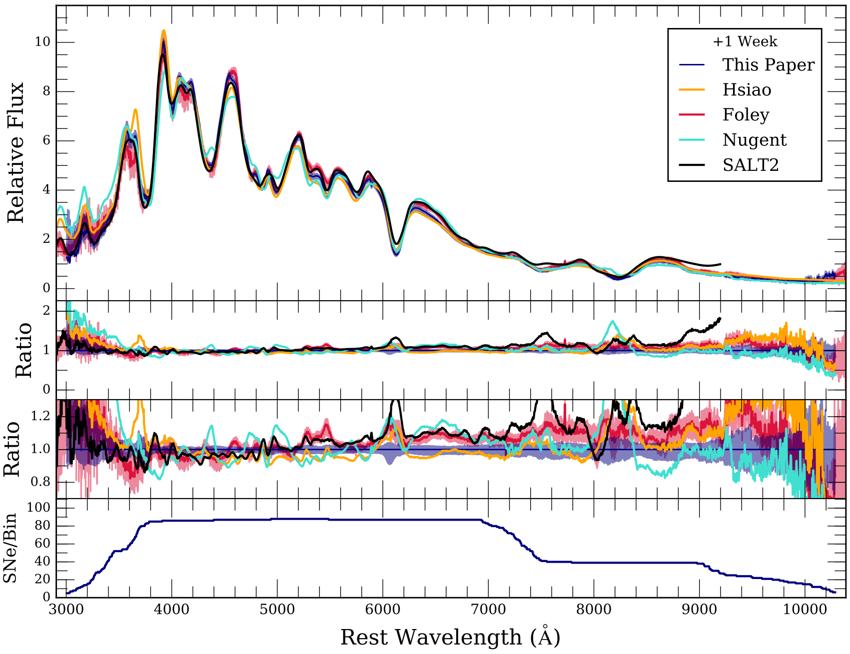

Figure 2.21: Same as Figure 2.18 except the composite spectrum (blue curve) is constructed using a phase bin of $+6 < \tau < +8$ days and $\Delta m_{15}(B) < 1.8$ mag.

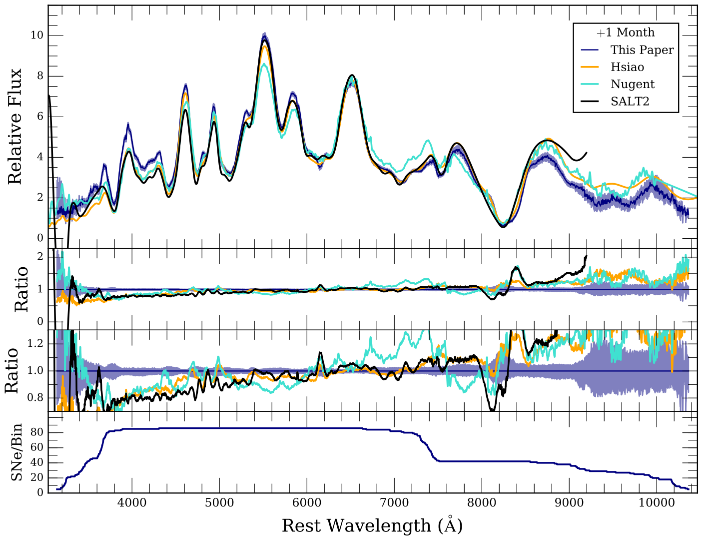

Figure 2.22: Same as Figure 2.18 except the composite spectrum (blue curve) is constructed using a phase bin of $+28 < \tau < +32$ days and $\Delta m_{15}(B) < 1.8$ mag.

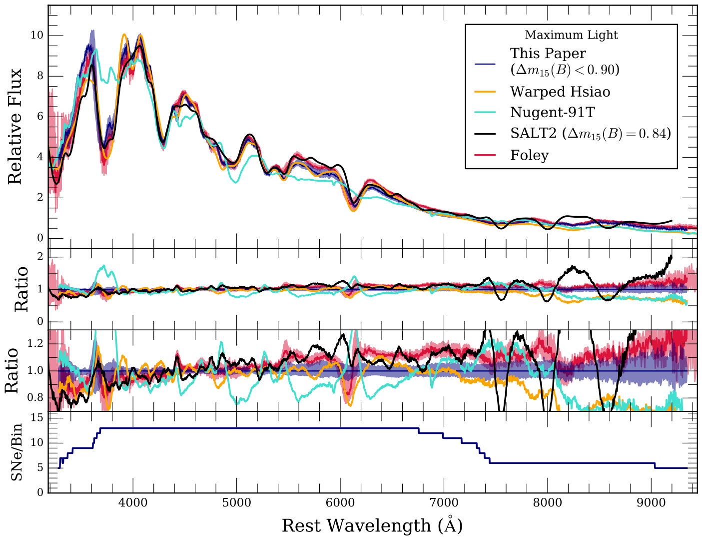

Figure 2.23: Same as Figure 2.18 except the composite spectrum (blue curve) is constructed using a phase bin of $-1 < \tau < +1$ days and a $\Delta m_{15}(B)$ bin of $\Delta m_{15}(B)$ < 0.90 mag. The maximum-light Hsiao template spectrum has been warped to match the B, V, and R-band photometry measured from the composite spectrum. The red curve is the Foley maximum-light, $\Delta = -0.27$ template spectrum. The light-blue is the Nugent-91T template spectrum, and the black curve is the maximum-light SALT2 model spectrum corrected for light-curve shape such that it has an effective $\Delta m_{15}(B)$ $= 0.84$ mag.

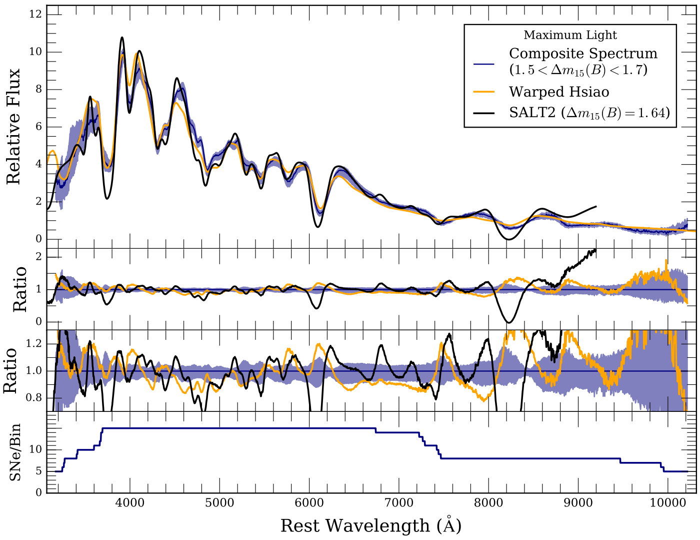

Figure 2.24: Same as Figure 2.23 except the composite spectrum (blue curve) is constructed using a phase bin of $-3 < \tau < +3$ days and a $\Delta m_{15}(B)$ bin of $1.50 < \Delta m_{15}(B) < 1.70$ mag. The maximum-light SALT2 model spectrum is corrected for light-curve shape such that it has an effective $\Delta m_{15}(B) = 1.64$ mag.

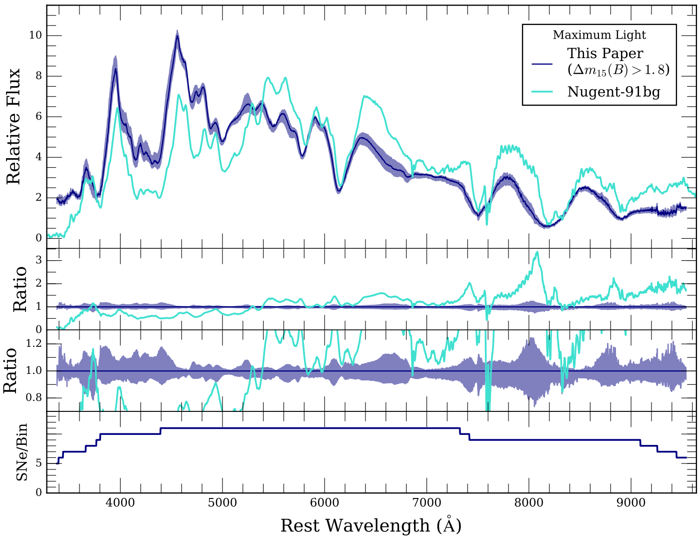

Figure 2.25: Comparison between a composite spectrum constructed from the fastest declining SNe Ia and the Nugent-91bg template spectrum. The composite spectrum (light-blue curve) is constructed using a phase bin of $-3 < \tau < +3$ days and a $\Delta m_{15}(B)$ bin of $\Delta m_{15}(B) > 1.80$ mag.

event with $\Delta m_{15}(B) = 0.84$ mag. This value of $\Delta m_{15}(B)$ is the average $\Delta m_{15}(B)$ of our composite spectrum. The value of x_1 was chosen using the polynomial relationship between $\Delta m_{15}(B)$ and x_1 shown in Figure 2.4. The Si II λ6355 feature is blueshifted 10,300 km s^{-1}, 11,000 km s^{-1}, 12,000 km s^{-1}, and 10,700 km s^{-1} for the composite spectrum, warped Hsiao template spectrum, Foley $\Delta = -0.27$ template spectrum, and SALT2 model spectrum respectively. Overall, the Foley $\Delta = -0.27$ template spectrum and SALT2 model reproduce the Si II λ6355 and λ5972 absorption features the best; however, both of these template spectra have slightly redder continua than the other spectra. The Nugent-91T template spectrum is almost exclusively constructed from SN 1991T which has $\Delta m_{15}(B) = 0.90$ mag. The Nugent-91T template spectrum reproduces the color of the composite spectrum, but does not do well reproducing individual absorption features. This difference is because our composite spectrum was constructing using all slow-declining events, and not just those from the SN 1991T-like subclass. The Foley $\Delta = -0.27$ template spectrum and our composite spectrum are well matched towards bluer wavelengths.

Similarly, we also compare template SN Ia spectra to a composite spectrum constructed from faster-declining events (Figure 2.24). In this case our composite spectrum created from a $\Delta m_{15}(B)$ bin of $1.50 < \Delta m_{15}(B) < 1.70$ mag. In this comparison we also warp the maximum-light ($\Delta m_{15}(B) = 1.1$ mag) template spectrum to the B, V, and R-band photometry of the composite spectrum. The SALT2 spectrum was created to represent a SN Ia with $\Delta m_{15}(B) = 1.64$ mag (the average $\Delta m_{15}(B)$ of the composite spectrum). It is important to note that the SALT2 template spectrum has $x_1 = -3.06$.

Since SALT2 training sample only included SNe Ia with $\Delta m_{15}(B) < 1.6$ ($x_1 > -3$)(Guy et al. 2007), we caution that the SALT2 template may not be adequately representative of these lower-luminosity SNe Ia. This SALT2 template spectrum does not match the composite spectrum as well as the slow-declining template spectrum matches the corresponding composite spectrum in Figure 2.23. Most of the absorption features of the faster-declining SALT2 template spectra are stronger than the respective features in the composite spectrum. However, the overall change in these features going from slow to faster declining events is similar between the composite spectra and SALT2 template spectra. Overall, after warping, the Hsiao template spectrum matches up well with our composite spectra for different values of $\Delta m_{15}(B)$. As expected, the largest differences between the Hsiao template spectra and our composite spectra occur in the features that strongly correlate with $\Delta m_{15}(B)$ (e.g., Si II and Ca II).

Finally, in Figure 2.25 we compare composite spectra for the fastest declining events $\Delta m_{15}(B) > 1.80$ mag to the Nugent-91bg template spectrum (Nugent et al. 2002). The Nugent-91bg template spectrum is constructed from SN 1991bg and SN 1999by and has telluric absorption included. Our composite spectrum has a bluer continuum and slightly larger line velocities. The composite spectrum also shows the Ti II absorption feature at ∼4300 Å characteristic of the SN 1991bg-like subclass.

2.5.4 Host-galaxy Morphology

In this section we investigate SN Ia spectral variations related to their host-galaxy environments. As seen above, SN Ia spectra strongly depend on phase and light-curve shape. We have shown that our composite spectra reproduce known spectral trends with these properties. Since low-luminosity SNe Ia tend to occur in early-type environments while high-luminosity SNe Ia tend to occur in late-type environments (Hamuy et al. 2000; Howell 2001), composite spectra (for a specific epoch) generated by solely splitting the sample by host galaxy morphology will reflect this correlation. Therefore, we must control for light-curve shape in order to uncover the differences between similar SNe Ia that occur in varying environments.

We make a single cut on host galaxy morphology via its Hubble classification. Our composite spectra represent SNe Ia originating from late-type galaxies classified as Sa to Sd/Irr and early-type galaxies classified as E to S0a. If we split our nominal sample into these two subgroups, we see the expected trend that SNe residing in late-type galaxies have an average $\Delta m_{15}(B) = 1.10$ mag and the SNe residing in early-type galaxies have an average $\Delta m_{15}(B) = 1.47$ mag. Since the spectral features of our composite spectra change significantly with $\Delta m_{15}(B)$ (section 2.5.2), we need to choose ranges of $\Delta m_{15}(B)$ that produce composite spectra with similar average properties. Since the two populations have differing average light-curve shapes we create our composite spectra to have an effective $\Delta m_{15}(B) \approx 1.3$ mag in order to incorporate the largest number of spectra. We match $\Delta m_{15}(B)$ between samples by making hard cuts on the allowed $\Delta m_{15}(B)$ ranges for each composite spectrum.

We have generated composite spectra for each host morphology subgroup at three separate epochs, $-6 < \tau < 0$ days (Figure 2.26), $0 < \tau < +6$ days (Figure 2.27), and $+6 < \tau < +11$ days (Figure 2.28). In each of these Figures the blue curve and shaded region are constructed from spectra of SNe Ia occuring in late-type galaxies and the red curve and shaded region are constructed from SNe Ia occuring in early-type galaxies. These Figures have similar format to Figure 2.7 where we presented our total maximum-light composite spectrum. The second panels show the ratio of the 1σ bootstrapping uncertainty regions relative to the late-type composite spectrum. The third panel shows the number of spectra contributing to each wavelength bin (we again require at least 5 spectra per wavelength bin). The other panels show the average values of phase, $\Delta m_{15}(B)$, and host-galaxy morphology as a function of wavelength for each composite spectrum. At all three epochs, we see evidence for stronger Na I D absorption in composite spectra representative of SNe residing in late-type galaxies which indicates more gas in the surrounding environment.

Overall we see very little difference between composite spectra constructed from SNe with differing host galaxy environments. In Figure 2.26 the late- and early-type composite spectra have effective phases of -2.4 and -2.7 days and an effective $\Delta m_{15}(B)$ of 1.28 and 1.29 mag respectively. The 1σ bootstrapping uncertainty region of the early-type composite spectrum is within the 1σ bootstrapping uncertainty region of the late-type composite spectrum at all wavelengths except for the red side of the Ca H&K absorption feature, and at the bluest wavelengths (<3500 Å). This Ca H&K feature is also double troughed in the early-type composite spectrum unlike the late-type composite spectrum. Since the average values of $\Delta m_{15}(B)$ are different by ∼0.1 mag at the bluest wavelengths, we may be able to attribute the differences in composite spectra at these wavelengths to a difference in average light-curve shape.

Post maximum light the host morphology-controlled composite spectra are

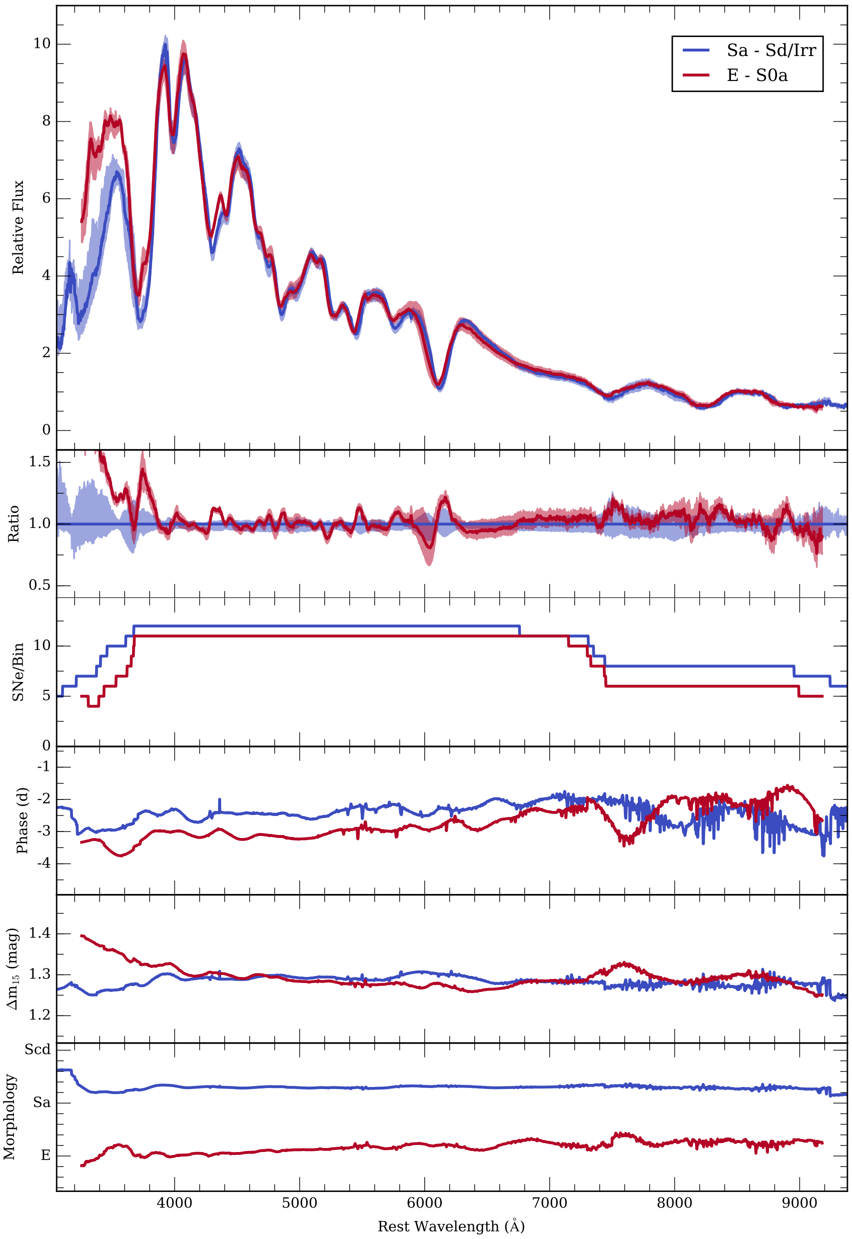

Figure 2.26: Same format as Figure 2.7 except the bottom panel now displays the average host-galaxy morphology of a given composite spectrum as a function of wavelength. The blue curves show the properties of our late-type composite spectrum and the red curves show the properties of our early-type composite spectrum. Both of these composite spectra were constructed using a phase bin of $-6 < \tau < 0$. The late-type composite spectrum was constructed using a light-curve shape bin of $1.20 < \Delta m_{15}(B)$ < 1.45 mag. The early-type composite spectrum was constructed using a light-curve shape bin of $1.15 < \Delta m_{15}(B) < 1.50$ mag.

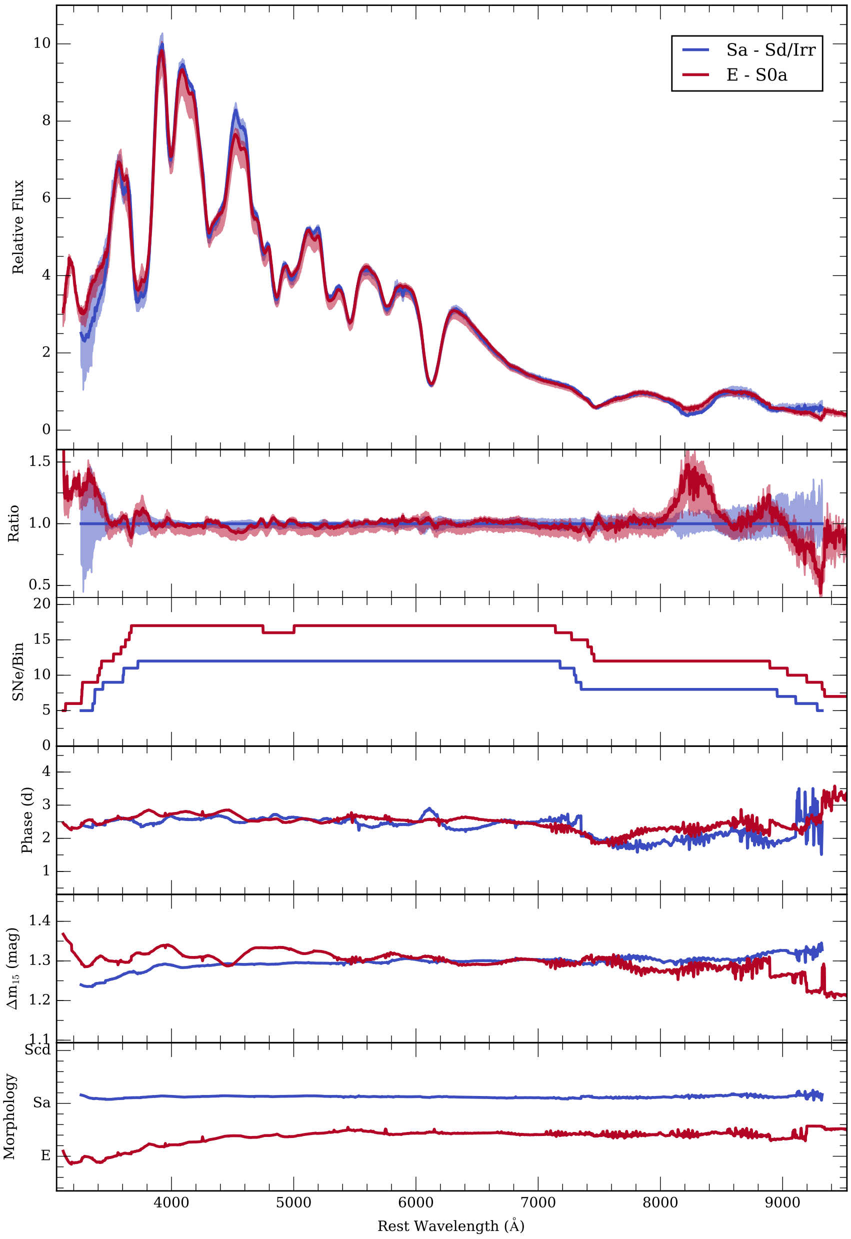

Figure 2.27: Same format as Figure 2.7. The blue curves show the properties of our late-type composite spectrum and the red curves show the properties of our early-type composite spectrum. Both of these composite spectra were constructed using a phase bin of $0 < \tau < +6$. The late-type composite spectrum was constructed using a light-curve shape bin of $1.20 < \Delta m_{15}(B) < 1.45$ mag. The early-type composite spectrum was constructed using a light-curve shape bin of $1.10 < \Delta m_{15}(B) < 1.50$ mag.

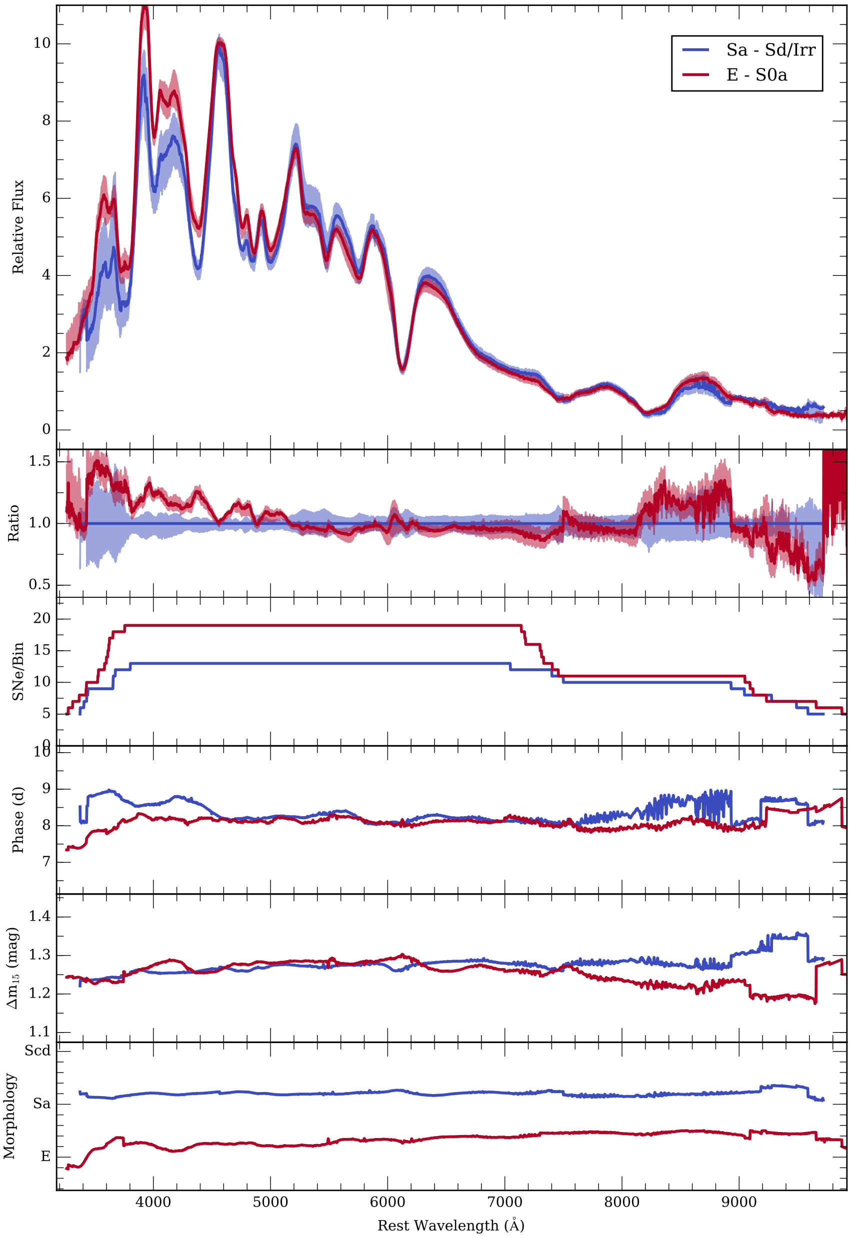

Figure 2.28: Same format as Figure 2.7. The blue curves show the properties of our late-type composite spectrum and the red curves show the properties of our early-type composite spectrum. Both of these composite spectra were constructed using a phase bin of $+6 < \tau < +11$. The late-type composite spectrum was constructed using a light-curve shape bin of $1.17 < \Delta m_{15}(B) < 1.48$ mag. The early-type composite spectrum was constructed using a light-curve shape bin of $1.15 < \Delta m_{15}(B) < 1.45$ mag.

also very similar with some consistent differences. The composite spectra in Figure 2.27 represent the late- and early-type subsamples and have effective phases of +2.35 and +2.52 days and an effective $\Delta m_{15}(B)$ of 1.30 and 1.29 mag respectively. There is one region near $\sim$ 4600 Å where the late-type composite spectrum has a slightly larger flux. There are also some slight differences in the Calcium absorption features. The early-type composite spectrum has slightly larger flux in the Ca II near-infrared (NIR) triplet absorption region.

Our final set of composite spectra for late and early-type host morphologies have effective phases of +8.4 and +8.1 days and an effective $\Delta m_{15}(B)$ of 1.28 and 1.25 mag respectively. The 1σ bootstrapping uncertainty regions are consistent at all wavelengths except in two regions. We see an excess flux in the early-type composite spectrum near the peak redward of the Si II λ4130 feature. Additionally, we see slightly weaker Ca near-infrared triplet absorption in the early-type composite spectrum. We see slightly weaker Ca H&K absorption in the early-type composite spectrum at +3 and +8 days, but these differences are consistent with the 1σ bootstrapping uncertainty regions of the late-type composite spectra at those epochs. It is important to note that while the spectra between each of these subsamples are different, some of the same SNe may contribute to the composite spectra at different epochs.

Across multiple epochs there is some evidence for weaker Ca II absorption in the early-type composite spectra. Since this difference is more evident in the Ca II NIR triplet absorption feature, we investigate the evolution of the equivalent width (EW) of this feature from the individual spectra contributing to these composite spectra.

These measurements are displayed in the left panel of Figure 2.29. Here, measurements coming from the same SNe are connected by lines and the black curve is the best fit linear evolution for the whole sample. We see a very slight tendency for the evolution of the Ca II NIR triplet EW for SNe residing in late-type galaxies (blue points) to lie above the mean evolution, and a very slight tendency for the evolution of the Ca II NIR triplet EW for SNe residing in early-type galaxies (red points) to lie below the mean evolution. To quantify this difference, we measure the mean residual per SN relative to our best fit evolution of the EW of the Ca II NIR triplet. In the right panel of Figure 2.29, we show the distribution of these residuals for two bins of host galaxy morphology. The mean Ca II NIR triplet EW residual for late- and early-type host galaxies are 29 ± 2 Å, and 4 ± 2 Å respectively. We perform a Kolmogorov-Smirnov test with these data and find a p-value of 0.60, suggesting that we cannot reject the hypothesis that these residual distributions are drawn from the same population. Nonetheless, the tentative evidence for a difference in the strength of the Ca feature is intriguing.

It is possible that these weaker Ca features can be explained by differences in progenitor metallicity. The simulations presented in De et al. (2014) and Miles et al. (2016) show decreasing ^{40}Ca yields with increasing metallicity while ^{28}Si yields stay constant. At each phase, our early-type composite spectra show weaker Ca II features than their late-type analogs and Si II features remain roughly constant (especially near maximum light). However, Miles et al. (2016) also predict that the the strongest effects of metallicity on spectra of SNe Ia should occur in the regions near ∼4200Å and ∼5200Å. Our early- and late-type composite spectra tend to be consistent and within

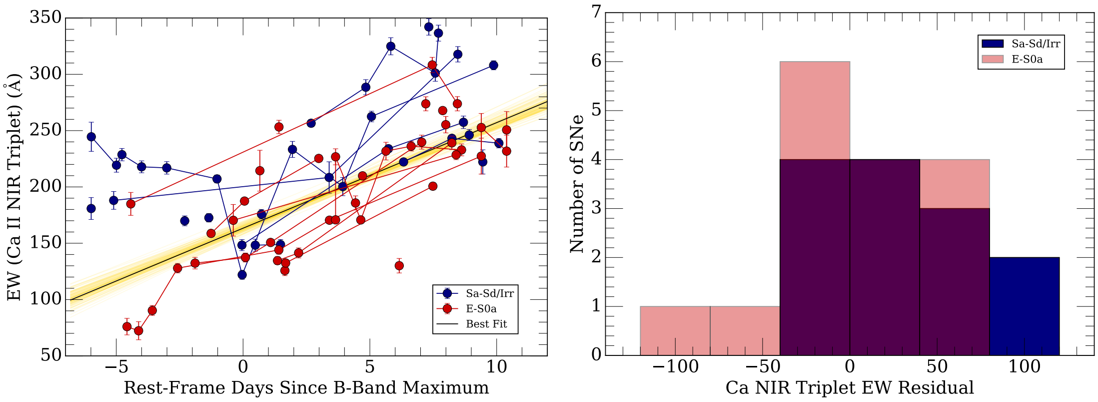

Figure 2.29: (*left*): Ca II NIR Triplet EW evolution for SNe residing in late (blue points) and early (red points) type galaxies. Measurements coming from the same SNe are connected by lines. The black curve is our linear best fit to the evolution of the whole sample ($y = (9.4 \pm 0.6)x + 163 \pm 4)$). The yellow curves are best fit lines generated from bootstrap resampling of the data. (*right*): Histograms of the late (blue) and early (red) type mean Ca II NIR Triplet EW residuals per SN.

the bootstrapping uncertainty regions in these wavelength regions.

The subdivision of our sample by host-galaxy morphology also shows our need for more data in these fine-grained groupings. Since there is a strong correlation between host-galaxy morphology and light-curve shape, disentangling effects of $\Delta m_{15}(B)$ from effects caused by the SN environment is difficult with our limited sample sizes. Although not significant, the differences that we see in Ca II absorption features between our late- and early-type composite spectra is intriguing and could be further investigated with more spectra. This analysis also shows the potential for our composite spectra to uncover minor trends in the spectral features of SNe Ia.

2.6 Discussion and Conclusions

We have compiled an open-source SQL relational database (`kaepora`) for observations of SNe Ia. We currently include all spectroscopic data from the largest low-z spectroscopic samples as well as UV data from HST and Swift. This amounts to 4975 spectra of 777 SNe. We have inspected these data for quality and enhanced the data by removing galactic emission lines and cosmic rays, generating variance spectra, and correcting for the reddening caused by both MW and host-galaxy dust. The resulting product is a fully homogenized and accessible sample of SN Ia spectra.

We construct Gini-weighted composite spectra from subsets of these data with sufficient metadata to estimate phase and correct for host-galaxy extinction. We generate 62 independent, phase-binned composite spectra with at least 20 contributing spectra covering phases -11 - $+271$ days. We also generate $\Delta m_{15}(B)$-binned composite spectra for a variety of effective light-curve shapes and phases. The maximum-light $\Delta m_{15}(B)$-binned composite spectra range from $\Delta m_{15}(B) = 0.86 - 1.87$ mag. Finally, we investigate the differences between composite spectra generated from SNe Ia residing and late-type and early-type galaxies. Wavelength ranges vary between composite spectra because we require at least 5 SNe to contribute at any given wavelength. Using these composite spectra we are able to reproduce and verify the following trends:

- General evolution of spectral features with phase for normal SNe Ia
- $B - V$ color evolution of normal SNe Ia
- Si II λ6355 velocity evolution of normal SNe Ia

- General spectral trends with $\Delta m_{15}(B)$ at maximum light
- Correlation of continuum with $\Delta m_{15}(B)$
- Correlation of $\mathcal{R}$ (Si II) with $\Delta m_{15}(B)$
- Lower Si II $\lambda6355$ velocities in SNe with extreme values of $\Delta m_{15}(B)$
- Na I D absorption in slower-declining SNe
- Na I D absorption in SNe residing in late-type galaxies

These numerous verifications assure us that the data in our database are of very high quality, which is encouraging for the large number of studies that we include. The additional metadata in our database (see Table 2.2) will be useful for future studies.

Our phase and $\Delta m_{15}(B)$-binned composite spectra are in good agreement with other template SN Ia spectra. In general the continua of composite spectra for normal SNe Ia are best matched by the Hsiao and Foley template spectra. This was achieved without any generic spectral warping. We have also demonstrated that larger bin sizes in phase and $\Delta m_{15}(B)$ can be used to produce composite spectra that are representative of SNe with the same average properties.

Finally, we examine the subtle spectral differences of composite spectra generated from samples with differing host-galaxy morphologies. Since we can control for both phase and light-curve shape, the remaining significant spectral differences should be related to the progenitor environments of these SNe Ia. Overall the composite spectra representing SNe occurring in late- and early-type environments are very similar at multiple epochs. We see a slight trend for weaker Ca II absorption in composite spectra representing SNe Ia occurring in early-type environments. However, by investigating the Ca NIR triplet EW evolution of these SNe, we do not find significant evidence for the association of these differences with two distinct populations.

Our primary goal for this work is to present `kaepora` to the community along with the tools that we developed for its validation. We encourage members of the community to use these tools where they see fit. We also strongly encourage the analysis of individual spectra which `kaepora` makes very easy.

We hope that our database will become a valuable tool for investigating the spectral properties of SNe Ia. We have demonstrated its utility for making template spectra with arbitrary average properties. While we have investigated some parameters here to demonstrate the power of this new database and technique, there are many potential future investigations using other parameters. Also, the large amount of photometric metadata present in the database should be useful for those not solely interested in spectra. Finally, we would like to emphasize that a particular strength this tool provides is fast testing of hypotheses. Since we have homogenized these observations, subsets of spectra with specific properties can be acquired and investigated via a few lines python code.

Chapter 3

A Possible Distance Bias for Type Ia Supernovae with Different Ejecta Velocities

3.1 Introduction

Type Ia supernovae (SNe Ia) are important tools for understanding the acceleration of the expansion of the Universe caused by dark energy (Riess et al. 1998; Perlmutter et al. 1999). SN Ia light-curve shape and color correlate with luminosity and a time series of photometric measurements of SNe Ia allow us to measure precise distances to these phenomena (Pskovskii 1977; Phillips 1993; Riess et al. 1996). As cosmological surveys continue to reduce their calibration uncertainty, systematic uncertainties related to the explosion physics of SNe Ia must also decrease or they will limit our ability to constrain dark energy properties (Jones et al. 2018a).

While light-curve shape and color are adequate to reduce the scatter in SN Ia distances to ∼8% (Scolnic et al. 2018; Jones et al. 2019), more parameters may be needed to further improve precision. Hubble residuals (HRs) are the differences between the measured distance moduli and distance moduli inferred from a cosmological model. After making corrections for light-curve shape and color, the HR scatter cannot be explained by photometric uncertainty alone, and this *intrinsic* scatter could be related to progenitor environmental properties or explosion physics (Conley et al. 2011; Scolnic et al. 2018). Several studies (e.g., Kelly et al. 2010; Lampeitl et al. 2010; Sullivan et al. 2010) have all found that the HR of a SN Ia is correlated with its host-galaxy mass. Other studies have found that host-galaxy metallicity also correlate with corrected SN Ia luminosity (D'Andrea et al. 2011; Childress et al. 2013c; Pan et al. 2014). These measurements should be a proxy for a physical property of the progenitor system. Current cosmological analyses treat the host-galaxy mass-HR relationship as a step function, yet we do not fully understand its origin or functional form (Childress et al. 2013c).

Rigault et al. (2013) first studied how SN properties correlated with local host-galaxy properties and found evidence for a HR step with local host-galaxy star formation rate (SFR). Rigault et al. (2018) found reduced evidence for a local SFR step after using an updated version of the SALT2 SN Ia model (Guy et al. 2010; Betoule et al. 2014), but found strong evidence for a local *specific* SFR (sSFR) step, and Roman et al. (2018) found similar evidence for a local step by measuring host-galaxy $U - V$ colors. Jones et al. (2018a) investigated the stellar masses and $u - g$ colors within 1.5 kpc of SN Ia explosion sites, finding evidence for a local mass step, but they could not definitively say that local properties are better correlated with SN Ia HRs than global properties or random information. Rose et al. (2019) found a correlation between HR and global host-galaxy age, but did not see evidence for a stronger local effect.

The UV spectra of SNe Ia could be a more direct probe of progenitor metallicity (e.g., Höflich et al. 1998; Lentz et al. 2000; Foley et al. 2008c; Sauer et al. 2008; Walker et al. 2012). Foley & Kirshner (2013b) found that two "twin" SNe Ia (SNe 2011by and 2011fe) have very similar light curves, colors, and spectra, but different UV continua. They attribute this difference to a difference in progenitor metallicity. Foley et al. (2020) then showed that these SNe have different intrinsic luminosities, indicating that progenitor metallicity could be related to intrinsic scatter. Similar results were found for a larger, but more diverse sample (Foley et al. 2016b). Pan et al. (2020) looked at a larger sample of SN Ia UV spectra and found that SN Ia HRs are positively correlated with progenitor metallicity; however, Brown et al. (2018) did not find evidence for this UV flux-metallicity correlation. Currently, spectral properties are infrequently used to calibrate SNe Ia.

Numerous studies have quantified the potential for spectroscopic measurements to improve HR intrinsic scatter. Bailey et al. (2009) found that measuring flux ratios in specific wavelength bins could improve upon using light-curve parameters alone. Blondin et al. (2011) confirmed this result and investigated the relationships of several other spectral properties with HR. They found marginal evidence that measuring line velocities or absorption strengths improves HR scatter. Silverman et al. (2012c) looked at an independent sample and found that velocity did not lead to significantly decreased HRs when applied in combination with SALT2 light-curve shape and color parameters. All of these studies found that flux ratios were the best spectral indicators for improving HR scatter. $\mathcal{R}(6520/4430)$, $\mathcal{R}^c(4610/4260)$, and $\mathcal{R}^c(3780/4580)$ (Bailey et al. 2009; Blondin et al. 2011; Silverman et al. 2012c, respectively) were found to reduce HR scatter at $> 2\sigma$ levels. Additionally, Zheng et al. (2018) modeled the relationship between peak magnitude, rise time, and photospheric velocity. They show that this model can significantly reduce HR scatter if high-velocity (HV) SNe are removed from the sample.

SNe Ia have a large diversity of observed ejecta velocities (Branch 1987). Benetti et al. (2005) found that a sample of SNe Ia have a large range of Si II λ6355 velocity gradients, where the amplitude of the gradient correlates with velocity at maximum light. Wang et al. (2009b) classified "High-Velocity" and "Normal" SNe Ia as SNe Ia above and below a velocity of ∼11,800 km s^{-1} respectively. For typical SNe Ia, the velocities derived from Si II λ6355 do not correlate with the decline-rate parameter $\Delta m_{15}(B)$ (Hatano et al. 2000). Some have suggested that "High-Velocity" SNe come from different progenitor channels than "Normal" SNe (e.g., Foley et al. 2012c; Maguire et al. 2013; Wang et al. 2013). Additionally, Foley & Kasen (2011) (hereafter FK11) found that HV SNe Ia have redder intrinsic $B - V$ colors than Normal SNe Ia. FK11 suggested that this effect could be reproduced with an asymmetric explosion viewed at different angles. Using a sample of 1630 optical spectra of 255 SNe, Foley et al. (2011) (hereafter FSK11) measured a correlation between maximum-light ejecta velocity and intrinsic $B-V$ color (the velocity-color relationship; VCR). This result was also verified for high-redshift SNe Ia (Foley 2012). If there are intrinsic differences between SNe Ia with varying velocities, we might expect that our cosmological distance corrections do not fully account for these effects.

In this work, we aim to investigate whether any optical spectral properties of SNe Ia correlate with HRs. This work makes use of `kaepora`, a public, open-source relational database of SN Ia spectra that was recently presented by Siebert et al. (2019) (hereafter S19). This tool provides a large sample of homogenized SN Ia spectra and their associated metadata. For this analysis, we have updated `kaepora` with new metadata from the output of SALT2 fits to SN light curves (Jones et al. 2018a). This new version of `kaepora` is available online[4]. Also included is a set of tools that is useful for spectroscopic analysis. In this work we primarily use composite spectra to investigate SNe Ia with varying HRs and control for spectral variation with phase and light-curve shape. These composite spectra cover a large wavelength range, and can provide more information about potential spectral feature trends than individual measurements (like ejecta velocities or equivalent widths).

In Section 3.2, we describe the subsample of SNe in `kaepora` that have HR measurements which we then use for this study. In Section 3.3, we present our HR-binned composite spectra and measure trends of spectral features with HRs. In Section 3.4, we summarize these spectral trends and discuss how they might impact cosmology. We conclude in Section 3.5.

---

[4] https://msiebert1.github.io/kaepora/

3.2 Methods

3.2.1 Sample

Version 1.1 of `kaepora` contains 4975 spectra of 777 SNe Ia. The majority of these data are sourced from the Center for Astrophysics (CfA) Supernova Program (Blondin et al. 2012b), the Berkeley SN Ia Program (BSNIP; Silverman et al. 2012b), and the Carnegie Supernova Project (CSP; Folatelli et al. 2013b) accounting for 51.9%, 25.6%, and 12.4% of the total spectra, respectively. While the CfA sample contains many spectra per SN (typically 7), the BSNIP spectra cover a much larger wavelength range (typical ranges of ∼3500 – 7500 Å and ∼3200 – 10000 Å, respectively). We also include data from Gomez et al. (1996); Riess et al. (1997); Leonard et al. (2005b); Blondin et al. (2006); Matheson et al. (2008); Foley et al. (2012c) and Silverman et al. (2015). This relational database allows for these data to be associated with a variety of useful SN-specific and spectrum-specific metadata.

The spectral sample for this work is a subset of the "nominal" sample described in detail by S19. The nominal sample required SNe with a calibrated light curve that covered the time of maximum light and an MLCS2k2 (Jha et al. 2007) host-galaxy extinction estimate in order to correct the spectra for host-galaxy dust reddening. The MLCS2k2 light-curve fits adopt $R_V = 2.5$ since typical cosmological analyses often exclude highly reddened SNe Ia that seem to favor lower values of R_V (Kessler et al. 2009b; Burns et al. 2014). We also correct each spectrum for Milky Way (MW) reddening using the Schlafly & Finkbeiner (2011) reddening map, a Fitzpatrick (1999) reddening law, and $R_V = 3.1$.

3.2.2 Hubble Residual Measurements

The HRs used in this analysis are from Jones et al. (2018b), with the SN light curves themselves originating from CfA surveys 1-4 (Riess et al. 1999; Jha et al. 2006a; Hicken et al. 2009, 2012) and CSP (Contreras et al. 2010; Folatelli et al. 2010; Stritzinger et al. 2011), with additional SNe from SDSS (Kessler et al. 2009b) and Pan-STARRS (Rest et al. 2014; Jones et al. 2018a; Scolnic et al. 2018) that are not included in this work. Notably, Foundation Supernova Survey light curves (Foley et al. 2018) are not included in this analysis, but will be in a future paper (Dettman et al., in prep.).

Light-curve fits to these data used the most recent version of the SALT2 model, SALT2.4 (Guy et al. 2010; Betoule et al. 2014). We also applied the selection criteria used in the Pantheon analysis (Scolnic et al. 2018) to ensure accurate distances. These include shape and color cuts that remove SNe with parameters outside the range for which the model is valid ($-3 < x_1 < 3$, $-0.3 < c < 0.3$) and cuts on the uncertainties of the shape and time of maximum light. We require MW reddening of $E(B-V) < 0.15$ mag and $z > 0.01$ to remove SNe that have distances with large peculiar-velocity uncertainties. The color cuts avoid SNe Ia with large dust reddening, which has been linked with atypical dust reddening and possible circumstellar scattering (e.g., Elias-Rosa et al. 2006b; Wang et al. 2008b; Phillips et al. 2013; Foley et al. 2014; Goobar et al. 2014) and has been linked to spectral differences (Wang et al. 2009b; Mandel et al. 2014).

SN Ia distances are derived from the light-curve parameters using a version of the Tripp (1998) formula that includes the host-galaxy mass step, γ and a bias correction, $\Delta_B(z)$:

$$\mu = m_B - \mathcal{M} + \alpha \times x_1 - \beta \times c + \Delta_B(z) + \gamma. \tag{3.1}$$

Here, m_B is the light curve amplitude, $\mathcal{M}$ is the SN absolute magnitude (whose exact value is degenerate with that of the Hubble constant and is irrelevant when only comparing HRs), and α and β are nuisance parameters that are determined from a fit to the full low-z sample. This fit is performed using the BEAMS with Bias Corrections (BBC) method of (Kessler & Scolnic 2017), which corrects for observational biases on the x_1, c, and m_B parameters as well as on α and β. Those biases are estimated using large Monte Carlo simulations, generated with the SNANA software (Kessler et al. 2009a), to match the low-z samples observations and sample demographics. Biases are corrected with the $\Delta_B(z)$ term. We estimate HRs relative to the maximum likelihood distances in three redshift bins to remove any dependence on cosmological parameters.

3.2.3 Hubble Residual Spectroscopic Sample

This work investigates the intersection of the S19 nominal sample with the sample of SNe Ia for which we have also measured HRs (named the HR sample). These requirements limit the HR sample to 1125 spectra of 126 SNe Ia. The properties of this subsample are compared to those of the S19 nominal sample in Figure 3.1. Overall, the distributions of the parameters of the HR sample is similar to the S19 nominal sample. Since cosmological analyses cut out the fastest-declining SNe, the HR sample does not cover as wide a range of $\Delta m_{15}(B)$ as S19. The HR sample also has a slightly larger

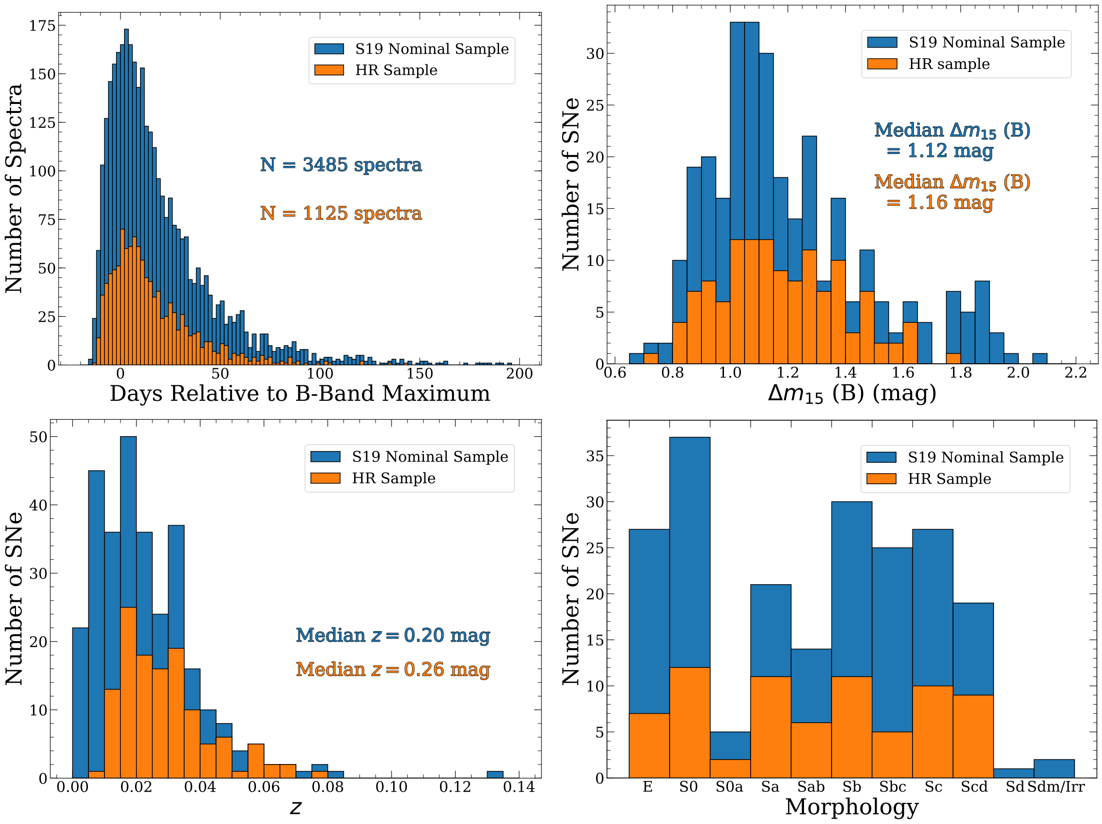

Figure 3.1: From top-left to bottom-right: Histograms of the number of individual spectra per SN, the number of SNe Ia per $\Delta m_{15}(B)$ bin, the number of SNe Ia per redshift bin, and the number of SNe Ia per bin in host galaxy morphology in the S19 nominal sample (blue) and HR sample (orange).

median redshift ($z = 0.026$ in the HR sample versus $z = 0.020$ in S19); this is because cosmological analyses only include SNe Ia in the Hubble flow where peculiar velocities of the SN host galaxies have a sufficiently small impact on distance measurements. It is also important to note that the HR sample only includes 7 spectra with $\tau > +100$ days compared to 131 spectra in the S19 nominal sample. Thus, analyses of the spectra in the HR sample at late phases are difficult to perform.

3.3 Analysis

The general goal of this work is take an agnostic approach to investigating the spectral properties of SNe Ia that could be related to HRs determined with current photometric-only techniques. Several of the studies discussed in Section 3.1 first form a hypothesis about how certain observables (e.g., host SFR, progenitor metallicity, etc.) may correlate with HRs, then focus on those individual measurements. Here, we take an alternative approach where we assume that the intrinsic scatter is caused by physical differences that can manifest as spectral differences. This approach minimizes the bias associated with determining the importance of specific pre-determined observables, can more easily discover unexpected results, and if no differences are found, produces a limit on the importance of spectral variability for reducing potential distance biases. `kaepora`, which both has tools to produce composite spectra for subsets of SNe and can easily control for properties known to correlate with the property in question (i.e., HR in this case), is uniquely designed for this kind of analysis. By looking at the average spectra of SNe with different HRs, we aim to determine which spectral properties (if any) correlate with HR.

3.3.1 Composite Spectra

In this work we generate Gini-weighted composite spectra using the methods presented by S19 for a variety of subsets of the HR sample. The Gini-weighting method provides a representative spectrum that maximizes the signal-to-noise ratio (S/N) while reducing the impact of individual high-S/N outliers. The basic algorithm is adapted from the methods used by Foley et al. (2008a) and Foley et al. (2012a). The composite spectra also contain information about the uncertainty and average properties (e.g., phase, $\Delta m_{15}(B)$, and redshift) as a function of wavelength. This information allows us to control for SN parameters that have known correlations with spectral features (such as phase and light-curve shape) as well as potentially unknown biases. S19 showed that a subset of spectra is well represented by a composite spectrum with the same average properties. We implement the same bootstrap resampling with replacement as in S19 in order to estimate the sample variation about the average spectrum.

In this work we use `kaepora` to provide subsets of SN Ia spectra that have similar average values of phase and $\Delta m_{15}(B)$ but different average HRs. By controlling for the main parameters that influence the diversity of SN Ia spectra, the remaining differences between composite spectra should be related to the parameter being varied. In this Section we present many of these Gini-weighted composite spectra. Due to the limitations of our sample size, we primarily present composite spectra generated using two HR bins (positive and negative). In Figure 3.2 we present five sets of maximum-light ($-2 < \tau < +2$ days) composite spectra constructed using these HR bins. From top to bottom, the composite spectra vary by the number of corrections that are made to the distance moduli of the contributing SNe.

First, we examine the composite spectra generated from SNe with positive and negative HRs when no light-curve shape, color, or mass-step corrections are applied. In this particular case, a SN with a negative HR has a higher peak luminosity and/or less host-galaxy dust extinction than a SN with a positive HR. The effective HR of

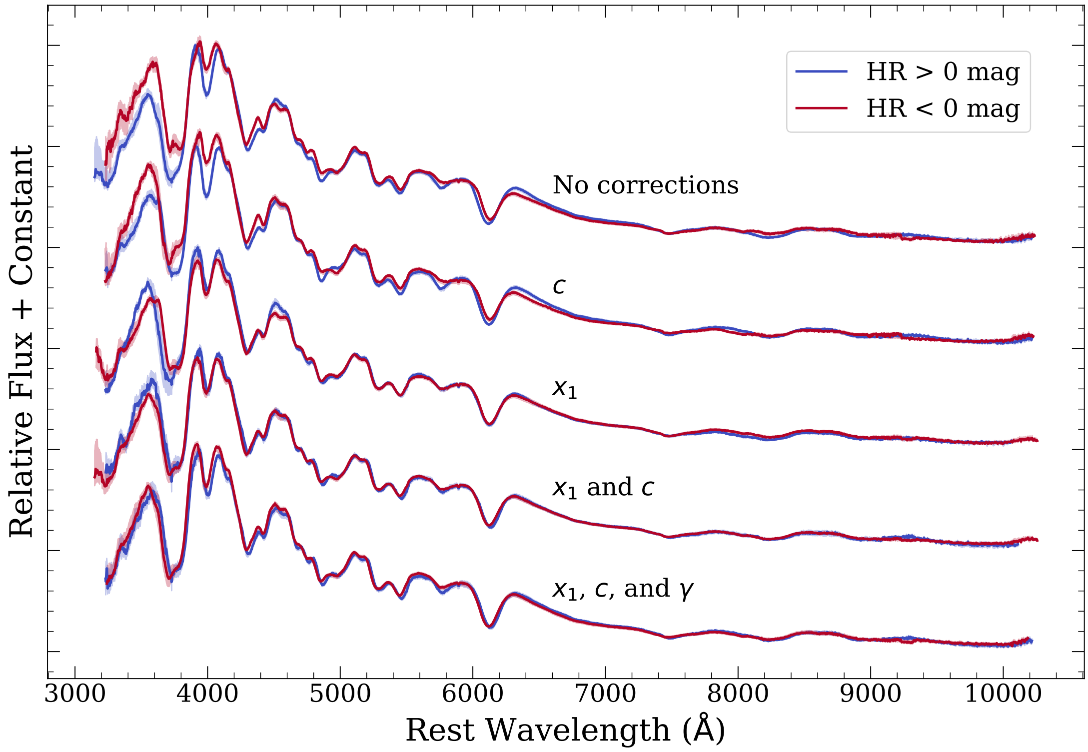

Figure 3.2: Four sets of maximum-light ($-2 < \tau < +2$ days) composite spectra constructed using positive- (blue) and negative-HR (red) bins. The shaded regions are the 1-σ bootstrap-sampling uncertainty for each composite spectrum. From top to bottom, the composite spectra vary in the distance modulus corrections that have been applied before measuring HRs. We start by using uncorrected luminosities, then subsequently correct for only light-curve shape (x_1); only color (c), light-curve shape and color (c); and light-curve shape, color, and host-galaxy mass step (γ). Most of the spectral variation between these two samples is removed after making the x_1 and c corrections.

these composite spectra are 0.22 and -0.24 mag, respectively. For these composite spectra, we see spectral differences between the positive-HR and negative-HR (higher peak luminosity) composite spectra that correspond to known trends in spectral features with light-curve shape. For example, the Si ratio ($\mathcal{R}$(Si II); Nugent et al. 1995) is smaller in the negative-HR composite spectrum. Additionally, the overall continua of the negative-HR composite spectrum is bluer than the positive-HR composite spectrum, consistent with intrinsic colors of different luminosity SNe Ia. These results confirm that our method can reproduce expected spectral differences.

Applying only a color correction (i.e., correcting μ by $c\beta$) provides the biggest reduction in HR scatter for a single correction. The positive-HR and negative-HR composite spectra have effective HRs of 0.03 and -0.10 mag, respectively. Applying only a light-curve shape correction (i.e., correcting μ by αx_1) decreases the spectral differences of the positive-HR and negative-HR samples, but the HR difference does not decrease as significantly. The effective HR of the composite spectra for these subsamples are 0.24 and -0.22 mag, respectively. The spectral features of these composite spectra are well matched and the most notable difference is in the continua. The negative-HR composite spectrum (red curve labeled "x_1 correction") appears to be slightly redder in color than its positive-HR counterpart. Naively one might expect the opposite relationship (the distances of bluer SNe after light-curve shape correction should be underestimated if the difference corresponds only to a lack of a dust-reddening correction). However, if the x_1 correction also accounts for continuum differences in some way, then it is possible to have this relationship with a color correction necessary to match continua. There is also a slight difference in the Ca H&K and Ca NIR triplet features. The Ca features in the negative-HR composite spectrum are slightly weaker and at lower velocity than the positive-HR composite spectrum.

Correcting distance moduli for light-curve shape and color (correcting μ for both αx_1 and $c\beta$) yields HR-binned composite spectra that are very similar. The continua are almost identical and the spectral feature strengths are well matched. The effective HR of these composite spectra are 0.10 and -0.12 mag, respectively, indicating that applying these distance modulus corrections has significantly reduced the HR scatter as expected.

Finally, introducing an additional host-mass step correction (γ) produces little change to the spectral features of the HR-binned composite spectra compared to those produced without making the host-mass correction. The effective HR of these composite spectra are 0.10 and -0.09 mag, respectively.

For the remainder of this work, composite spectra are generated using distance moduli that have been corrected for x_1, c, and γ, corresponding to the values used in cosmological analyses, unless otherwise noted.

3.3.2 Hubble Residuals and Velocity

Despite having similar continua and overall line strengths, we observe a general trend that composite spectra generated from SNe with differing HRs tend to have different line velocities in many of their spectral features. In Figure 3.3, we present composite spectra generated from samples of SNe with positive and negative HRs (blue curve) and spectra with phases of $+2 < \tau < +7$ days. The positive-HR and negative-

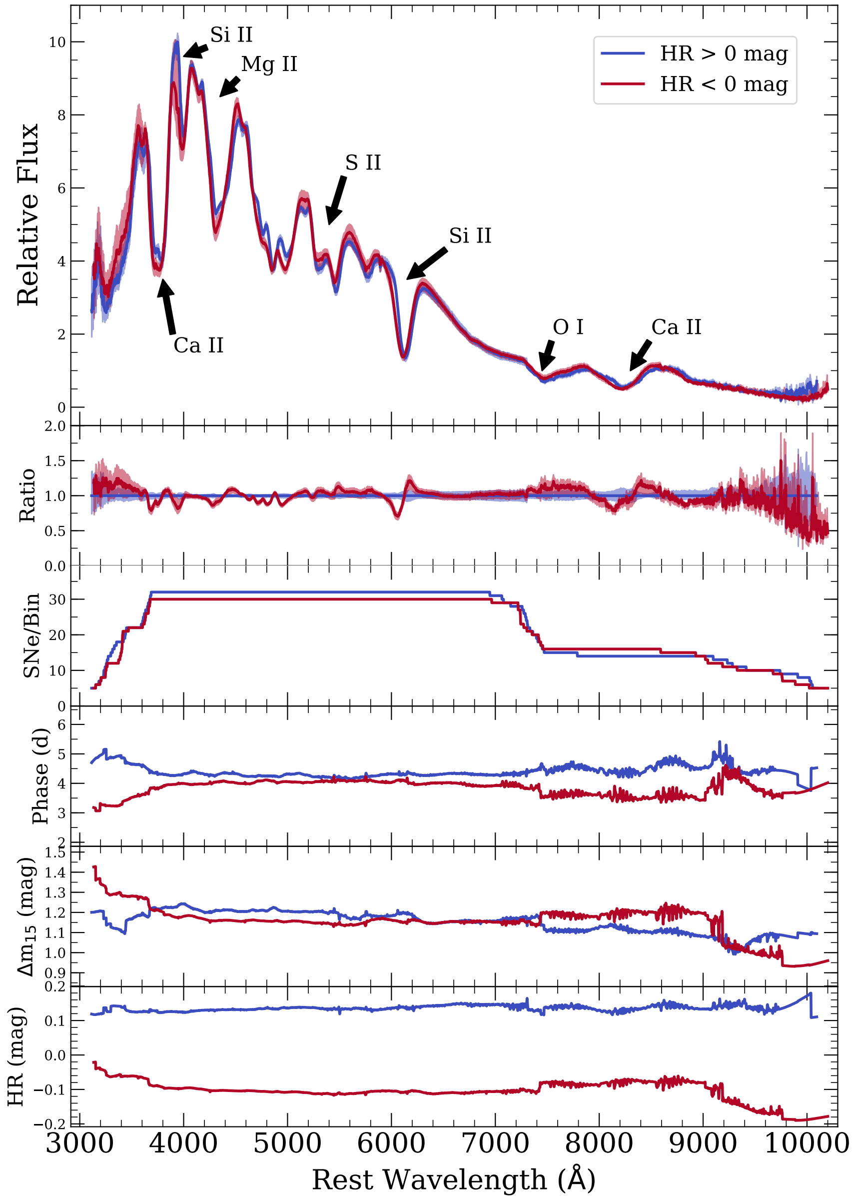

Figure 3.3: (*First panel*): +4-day composite spectra created from our nominal sample ($+2 < \tau < +7$ days, $0.7 \leq \Delta m_{15}(B) \leq 1.8$ mag). The blue curves show the properties of our positive-HR composite spectrum and the red curves show the properties of our negative-HR composite spectrum. The shaded regions are the 1-σ bootstrap sampling uncertainties. (*Second panel*): Ratio of the negative-HR composite spectrum relative to the positive-HR composite spectrum (red) and uncertainties on the positive-HR/negative-HR composite spectra (blue/red). (*Third panel*): Number of individual spectra contributing to each wavelength bin. (*Fourth panel*): Average phase relative to maximum brightness as a function of wavelength. (*Fifth panel*): Average value of $\Delta m_{15}(B)$ as a function of wavelength. (*Sixth panel*): The average HR as a function of wavelength.

HR composite spectra were constructed from 88 spectra of 30 SNe, and 65 spectra of 32 SNe, respectively. The composite spectra have effective phases of +4.4 and +3.8 days and effective values of $\Delta m_{15}(B)$ of 1.13 and 1.19 mag, respectively.

The positive-HR and negative-HR composite spectra have Si II λ6355 line velocities of $-10{,}600$ km s^{-1} and $-11{,}580$ km s^{-1}, respectively. Similar velocity shifts are also clearly visible for Ca H&K, Si II λ5972,6355, S II, and the Ca near-infrared (NIR) triplet (see the second panel of Figure 3.3). In regions where the continua are matched up well (e.g., Si II and the Ca NIR triplet), these differences are obvious in the ratio of the composite spectra.

Since the HR-binned composite spectra at +4 days show a dramatic difference in ejecta velocity, we also investigate the Si II line velocities of the individual SNe contributing to each composite spectrum. The +4-day composite spectra contain data from 62 SNe whose velocity and HR measurements are shown in Figure 3.4 as black points (hereafter the "+4-day" HR sample). The orange stars are the velocity measurements made directly from the composite spectra displayed in Figure 3.3 and the shaded-blue violin regions depict the distributions of velocities measured from the individual output spectra from our bootstrap resampling process of each sample. At the top of Figure 3.4, we display HR histograms for the sample divided at $-11{,}000$ km s^{-1}, the median velocity of the sample. We also display velocity histograms for positive-HR and negative-HR SNe on the right side of Figure 3.4.

There is no strong correlation between Si II velocity at +4 days and HR (absolute Pearson correlation coefficient of $\sim$0.30), however there is some intriguing structure

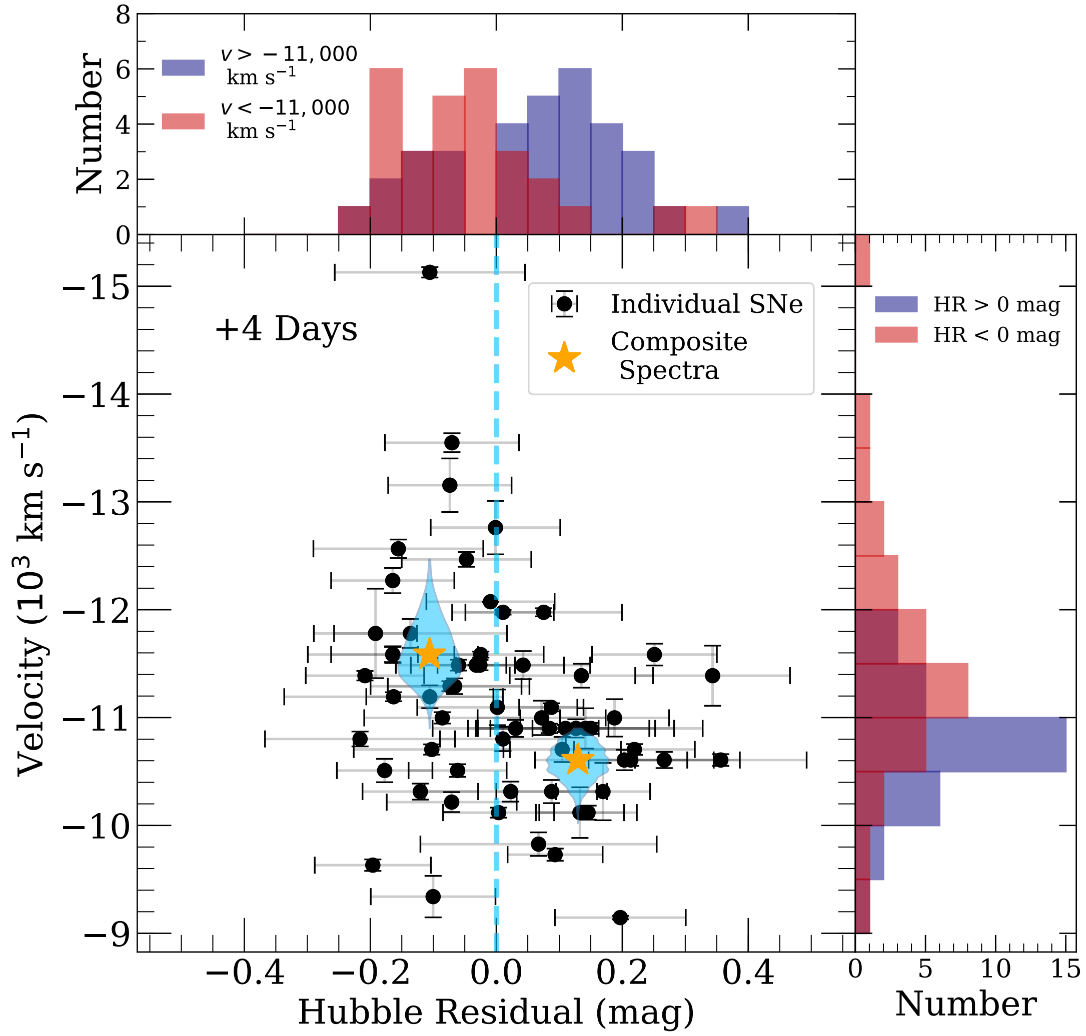

Figure 3.4: Si II velocity for individual SNe versus their HR (black points) for the sample of SNe contributing to our +4-day composite spectra in Figure 3.3. Orange stars correspond to the measurements from our composite spectra. The blue shaded region shows the distribution of velocities from bootstrap resampling. The vertical blue-dashed line at HR = 0 mag shows where the sample is divided. The top blue and red histograms display the distributions of HRs for SNe with $v > -11,000$ km s^{-1} and $v < -11,000$ km s^{-1}, respectively. The right blue and red histograms display the distributions of velocities for positive-HR and negative-HR SNe, respectively.

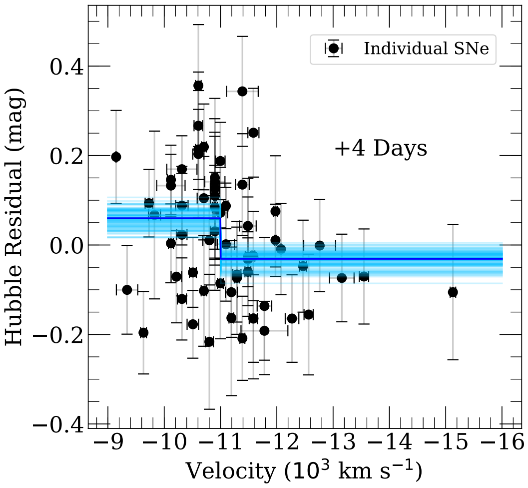

Figure 3.5: HR versus Si II velocity for individual SNe (black) in the +4-day sample. We fit a two-parameter step function (blue) to these data where we split the sample at the median velocity (−11,000 km s^{-1}). The light-blue lines represent a subset of fits to random realizations of the data. The orange stars show measurements from composite spectra where we separate the sample at the same velocity. The best-fitting offset between two subsamples is 0.091 ± 0.035 mag offset (2.7σ).

to the distribution of measurements. For example, there are no positive-HR SNe with velocities higher than −12,000 km s^{-1} in this phase bin. Using the uncertainties estimated from bootstrap resampling, we measure a velocity difference of 980 ± 220 km s^{-1} (680 ± 150 km s^{-1} after removing $>2\sigma$ velocity outliers) between the positive-HR and negative-HR composite spectra. We perform a Kolmogorov-Smirnov test with high/low-velocity ($v_{\mathrm{Si\,II}}$ below/above −11,000 km s^{-1}) samples and find a p-value of 0.00031 (3.4σ), suggesting that we can reject the hypothesis that the HR distributions of these samples are drawn from the same population. We also perform a Kolmogorov-Smirnov test with positive-HR/negative-HR samples and find a p-value of 0.00078 (3.2σ), suggesting that we can also reject the hypothesis that the velocity distributions of these samples are drawn from the same population.

Despite the formally high significance of these tests, the HR uncertainties for individual objects are relatively large (typically 0.12 mag), and a large fraction of SNe have a sizeable probability of truly belonging to the opposite group than it is assigned. To include this uncertainty in our significance tests, we generate 10^6 realizations of the HR values in the +4-day sample, varying the HRs by a Gaussian distribution with a standard deviation corresponding to the uncertainty of the HR measurement. In Figure 3.5, we display HR as a function of Si II velocity at +4 days after maximum light. The black points and error bars are the same data as in Figure 3.4 (but the axes are swapped). The dark-blue curve is a two-parameter step function fit to the original data where the sample is split at the median velocity ($-11{,}000$ km s^{-1}). The light-blue curves are 100 randomly chosen step-function fits to the resampled HR values. Using these data, we estimate a velocity step of 0.091 ± 0.025 mag (3.7σ). To investigate the importance of choosing the median velocity to separate the sample, we allowed the velocity that separates the samples to be a free parameter in our fit. Doing this, we measure a similar velocity step of 0.091 ± 0.027 mag (3.4σ), indicating that the exact choice of velocity to separate the sample is not driving the results. The removal of $>2\sigma$ velocity outliers also has a small impact on the step size (0.087 ± 0.025 mag). The low- and high-velocity samples have a sample intrinsic scatter of 0.108 mag and 0.064 mag, respectively. If we include the intrinsic scatter in the HR uncertainties, we measure a velocity step of 0.091 ± 0.035 mag (2.7σ).

3.3.3 Temporal Evolution of the Velocity-HR Trend

The velocity-HR trend is also visible over a large range of phases. In Figure 3.6 we present the Si II $\lambda6355$ feature in six positive-HR (blue curves) and six negative-HR (red curves) composite spectra representing phases of approximately -9 ($\tau < -7$), -5 ($-7 < \tau < -2$), 0 ($-2 < \tau < +2$), $+4$ ($+2 < \tau < +7$), $+9$ ($+7 < \tau < +13$), and $+15$ ($+13 < \tau < +21$) days. At all epochs prior to $+15$ days after maximum light, we see that the Si II feature appears more blueshifted in the negative-HR composite spectra (red) than the negative-HR composite spectra (blue). These differences are apparent across a large range of velocities and often can not be accounted for by the 1σ bootstrapping uncertainty regions. The velocity difference manifests as a shift in the wavelength of maximum absorption (from which we determine the velocity of the feature), the width of the feature, and the position of the blue edge of the feature. The full line profile provides additional information and evidence that the difference in ejecta velocity for the different HR subsamples is significant.

Using the relationships derived by Foley et al. (2011), we use the spectrum closest to maximum light to estimate $v^0_{\text{Si II}}$, the maximum-light Si II velocity, for each SN. With a sample of 115 SNe Ia we measure a $v^0_{\text{Si II}}$-HR step of 0.068 ± 0.027 mag when the sample intrinsic scatter is included in the HR uncertainties. This is consistent with our step measurement from the $+4$-day sample (0.091 ± 0.035 mag).

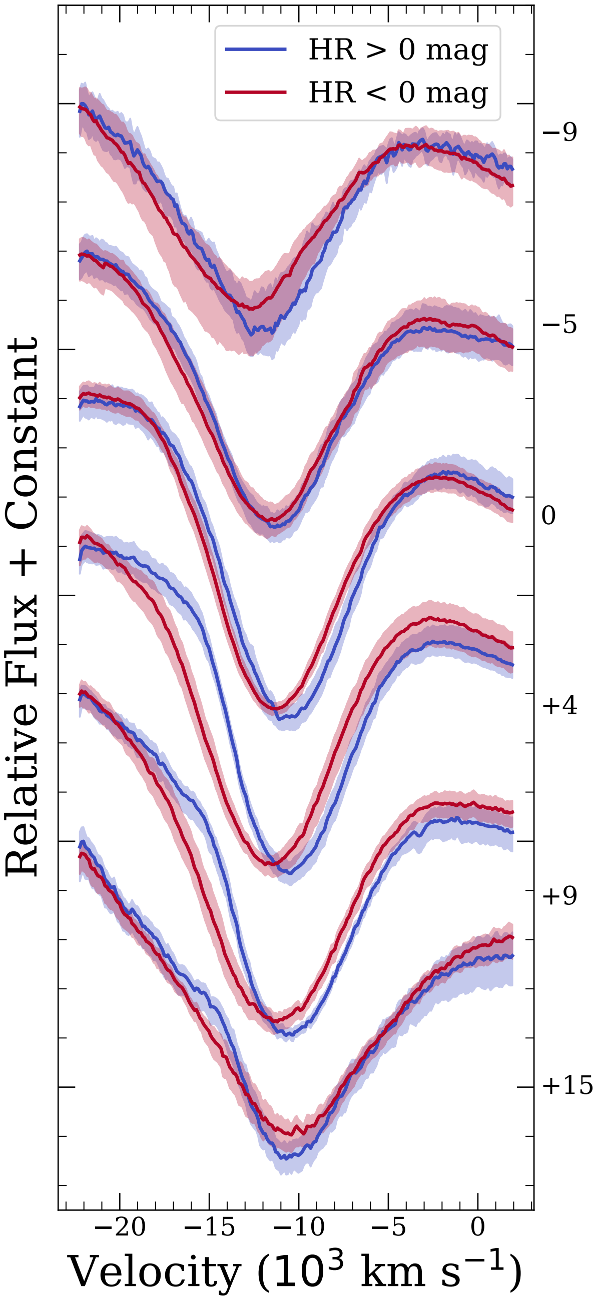

Figure 3.6: Time series of composite spectra created from subsamples of SNe with positive (blue) and (negative) HRs displaying the region around Si II λ6355. The blue- and red-shaded regions are the 1-σ bootstrap-sampling uncertainties of the positive- and negative-HR composite spectra, respectively. The right vertical axis indicates the effective phase in days of each set of composite spectra. At all epochs prior to +15 days, the minimum of the main Si II feature is more blueshifted in the negative-HR sample than the positive-HR sample.

3.3.4 Velocity-HR Trend Seen in Other Features

The velocity-HR trend is also visible in several absorption features besides Si II and over a large range of phases. Here we examine these other indicators of ejecta velocity correlating with HR.

In Figure 3.7 we display the spectral evolution of the Ca H&K, Si II λ4130, S II "W" feature, Si II λ5972, λ6355, and the Ca NIR Triplet in the same 6 sets of HR-binned composite spectra. We do not show composite spectra of the Ca NIR triplet at the earliest epoch because there are not enough SNe in the `kaepora` HR sample at that epoch to get 5 SNe per wavelength bin in that region. The fluxes of the HR-binned composite spectra have been rescaled in each absorption region to best compare the line profiles.

In the majority of the negative-HR composite spectra (red), the minima of these absorption features appear blueshifted relative to their positive-HR counterparts (blue). With the exception of S II, which shows a large velocity difference at −9 days, the largest discrepancies in velocity occur either in the maximum-light or +4-day composite spectra for each absorption feature. All of the Si II features (λ4130, λ5972, and λ6355) are more blueshifted in the negative-HR composite spectra at every epoch except +15 days where they have similar velocities. Ca H&K appears more blueshifted in the negative-HR composite spectra at every epoch. However, the Ca NIR triplet is more variable. The early-phase (−5 and 0 days) composite spectra of this feature are very similar, but the later-phase composite spectra show the same velocity trend as the other spectral absorption features.

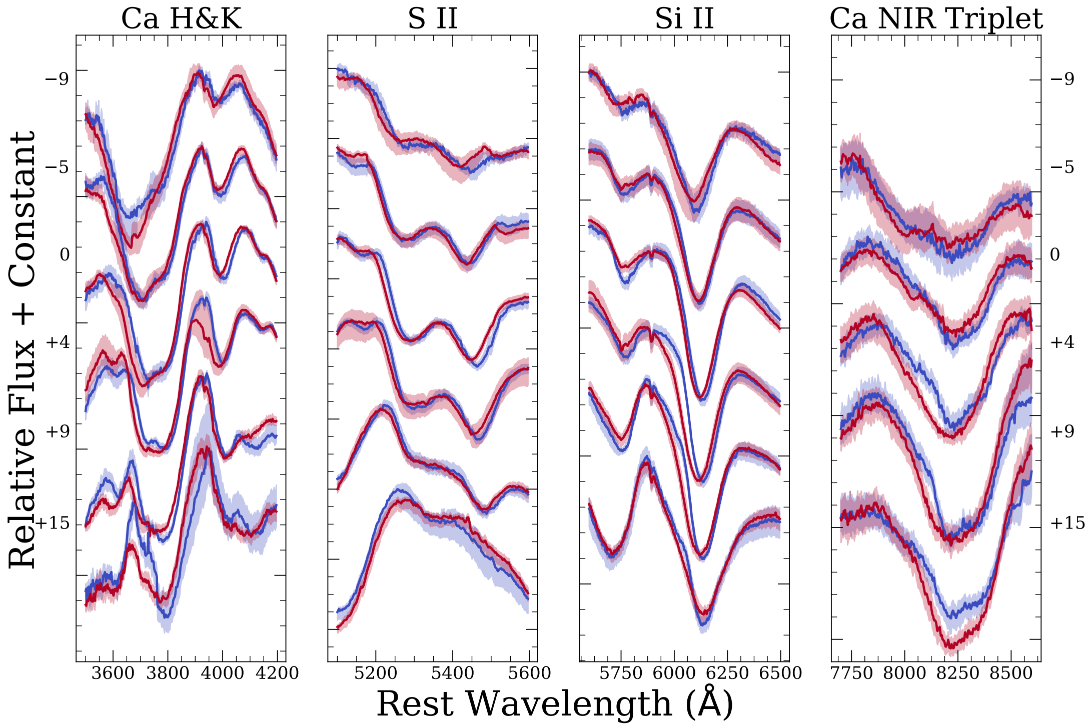

Figure 3.7: Time series of composite spectra created from subsamples of SNe with positive (blue) and (negative) HRs focusing on the Ca H&K (first panel), S II (second panel), Si II (third panel), and Ca II NIR triplet (fourth panel) features. Blue and red curves/shaded regions correspond to the positive-HR and negative-HR composite spectra respectively. The effective phase from top to bottom of the sets of composite spectra are −9 (excluding the Ca II NIR triplet), −5, 0, +4, +9, and +15 days.

We further examined color-corrected flux ratios other authors found to correlate with HRs. For the highest-significance ratios, we find differences in the +4-day composite spectra. Notably, the two wavelengths used for a flux ratio (e.g., 4260 and 4610 Å for $\mathcal{R}^c(4610/4260)$; Blondin et al. 2011) are at the edges of a spectral feature (in the example, Mg II). For these cases, the flux ratio changes significantly with velocity since the edge of a feature will shift, adjusting the flux at a particular wavelength. We do not find evidence for different line strengths beyond the velocity difference for these measurements.

3.3.5 Hubble Residuals and Color Curves

Despite the velocity differences observed in the spectral absorption features, the continua are similar. We examine this in more detail by synthesizing $B - V$ and $V - i$ color curves, which we present in Figure 3.8.

The color curves of the HR-binned composite spectra look very similar. There is some tentative evidence that the positive-HR sample is redder than that of the negative-HR sample at $\tau \gtrsim 30$ days, while the $V - i$ color of positive-HR sample is bluer. This potential trend is discussed further in Section 3.4.

3.3.6 Hubble Residuals and Absorption Strength

In addition to the velocity-HR relationship discussed above, we also see an indication of spectral deviations between HR-binned samples at phases 1–3 months after peak. In Figure 3.9 we present three sets of HR-binned composite spectra with effective phases of +37, +52 and +77 days from top to bottom, respectively.

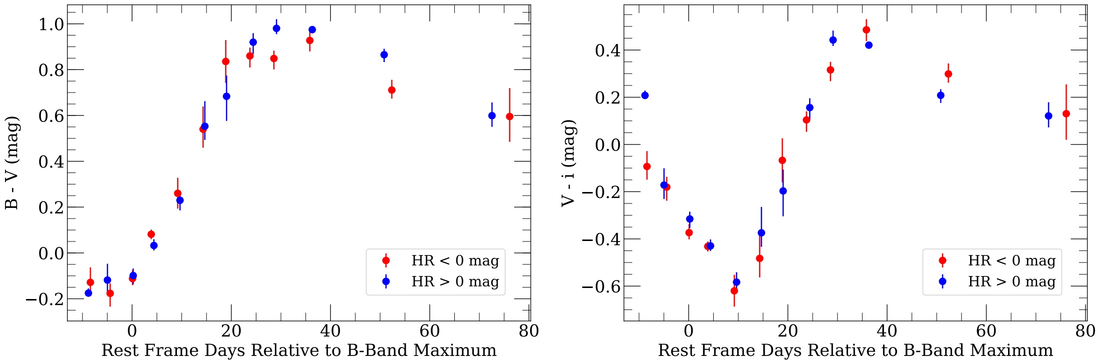

Figure 3.8: $B-V$ (left) and $V-i$ (right) color curves of our positive- (blue) and negative (red) composite spectra.

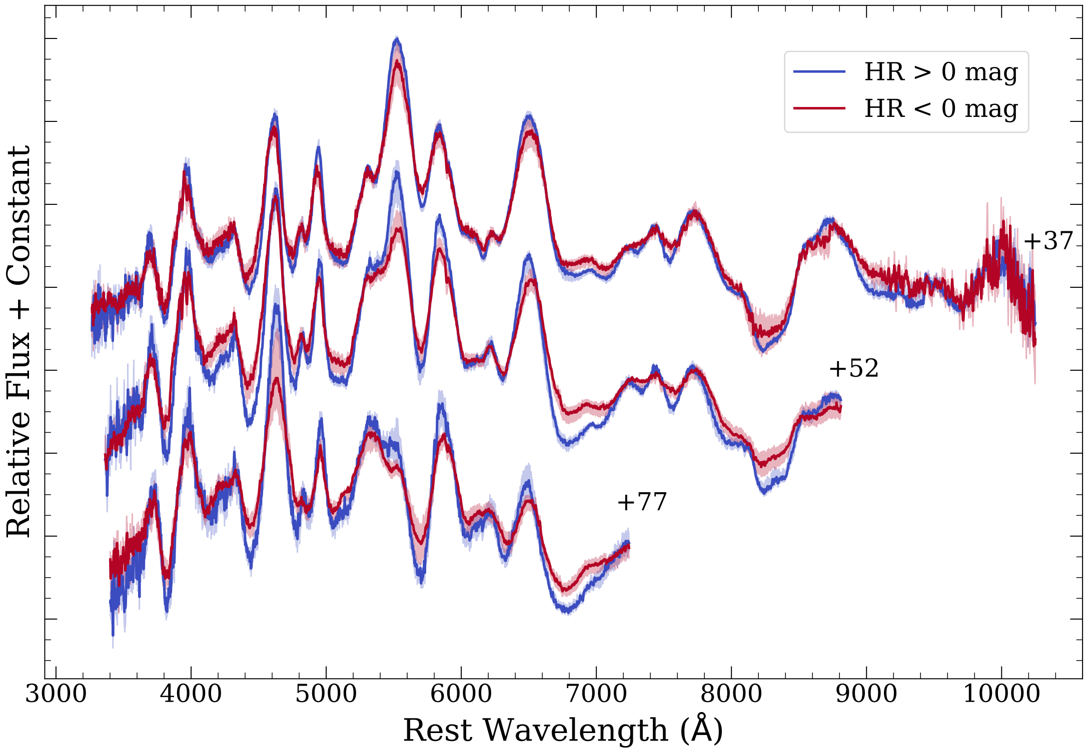

Figure 3.9: HR-binned composite spectra Composite spectra with effective phases of +37, +52, and +77 days from top to bottom. Blue and red curves/shaded regions correspond to the positive- and negative-HR composite spectra, respectively.

At +37 days, the positive-HR and negative-HR composite spectra look very similar. While there are some subtle differences, most of these deviations are contained within the 1-σ bootstrap resampling uncertainty regions. However, as the composite spectra progress to later phases, the differences become more significant.

In the three displayed spectra, the negative-HR composite spectrum has weaker features than the positive-HR composite spectrum. This relationship is most obvious in the +52-day HR-binned composite spectra, but is also significant in the +77-day HR-binned composite spectra, but with a limited wavelength range and fewer SNe contributing. For this reason, we chose to further examine this trend by examining the +52-day composite spectra in more detail.

Figure 3.10 is the same format as Figure 3.3 and shows these composite spectra along with some more detailed, wavelength-dependent information. These composite spectra were constructed using a phase bin of +42 – +62 days and $\Delta m_{15}(B)$ bins of 0.7 – 1.8 mag. The effective phase, $\Delta m_{15}(B)$, and HR of the positive-HR composite spectrum are 50.8 days, 1.11 mag, and 0.09 mag, respectively (52.4 days, 1.08 mag, and −0.11 mag, for the negative-HR composite spectrum, respectively). While the phase bin is large, the average phase only differs by more than 3 days (<5% of the time since explosion) in 6% of all wavelength bins. Similarly for $\Delta m_{15}(B)$ (fifth panel), the average $\Delta m_{15}(B)$ at every wavelength only differs by more than 0.1 mag in 14% of wavelength bins. It is also noteworthy that the positive-HR and negative-HR sample sizes are very different in this phase range. With the positive-HR sample containing 18 spectra of 11 SNe, and the negative-HR sample containing 60 spectra of 31 SNe. While these spectral

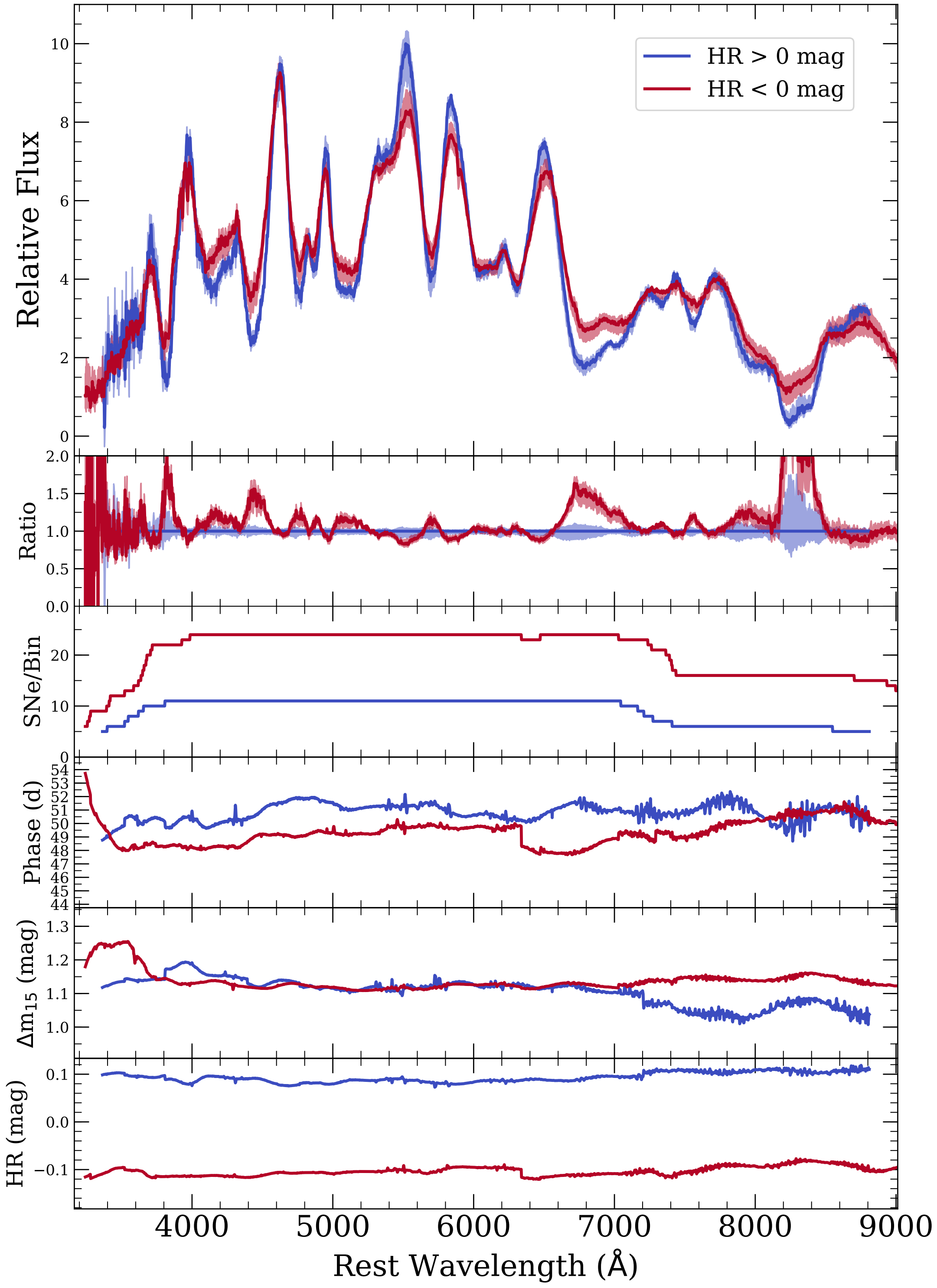

Figure 3.10: Same as Figure 3.3 but comparing the +52-day HR-binned composite spectra.

differences seen at these later epochs are intriguing, the small number of contributing SNe limits our inference.

A difference like this could be attributed to a difference in the overall continuum level of SNe with different HRs. The fractional depth of spectral features in SNe Ia with a larger overall flux levels should be smaller. Wang et al. (2019) has suggested that a *B*-band offset in HV SNe at phases $>+40$ days could be due to a light echo from circumstellar dust. A light echo could dilute the specral features. However, our composite spectra do not exhibit a large color difference at this phase (Section 3.3.5), disfavoring a light-echo explanation for the difference in spectral feature strength.

It is also possible that host-galaxy light contamination is causing the observed feature strength differences. This could also change the continuum level, diluting the strength of features. Since the difference between the spectra does not look like a galaxy spectrum, this scenario is less likely. Since there are only 11 SNe in the positive-HR sample, we caution interpretation of this difference until a larger sample is obtained.

3.4 Discussion

Composite spectra provide an agnostic approach to understanding spectral correlations with HR. Through this approach we find that velocity is the most important optical spectroscopic indicator of HR after all typical corrections are made. Quantifying the significance of the velocity-HR relationship is challenging since we observe this trend in several spectral absorption features and at several epochs. Most methods yield a statistically significant result.

We find that SNe with negative HRs tend to have higher ejecta velocity. Similarly, we find that SNe with higher ejecta velocity tend to have negative HRs after all light-curve and host-galaxy corrections are applied. That is, using modern techniques as done for cosmological analyses, SNe Ia with high (low) ejecta velocity have measured distance that are biased low (high).

In this section, we further discuss the significance of our results, and the implications a velocity distance bias would have on SN Ia cosmology results.

3.4.1 Temporal Velocity Evolution and HR Differences

In Figure 3.11, we further examine the evolution of $v_{\mathrm{Si\,II}}$. The individual blue (red) points correspond to Si II λ6355 velocity measurements from individual spectra whose SNe have positive-HR (negative-HR). The solid blue and red points connected by lines are the 2-day binned medians of these velocity measurements, and the error bars are the median absolute difference within each bin. While the scatter is large, it is clear that the negative-HR sample has consistently higher velocities on average than the positive-HR sample until ∼+15 days after maximum light. Over all bins in this phase range, the negative-HR sample is on average 500 km s^{-1} above the negative-HR sample, consistent with the +4-day subsample.

However, it is also important to note that these median measurements are correlated. While the phase bins do not overlap and individual measurements contribute to only a single median value, the same SN may have multiple spectra that cover a range of phases. We quantify this correlation with a simple Monte Carlo simulation. The positive-HR and negative-HR samples displayed in Figure 3.11 contain data from

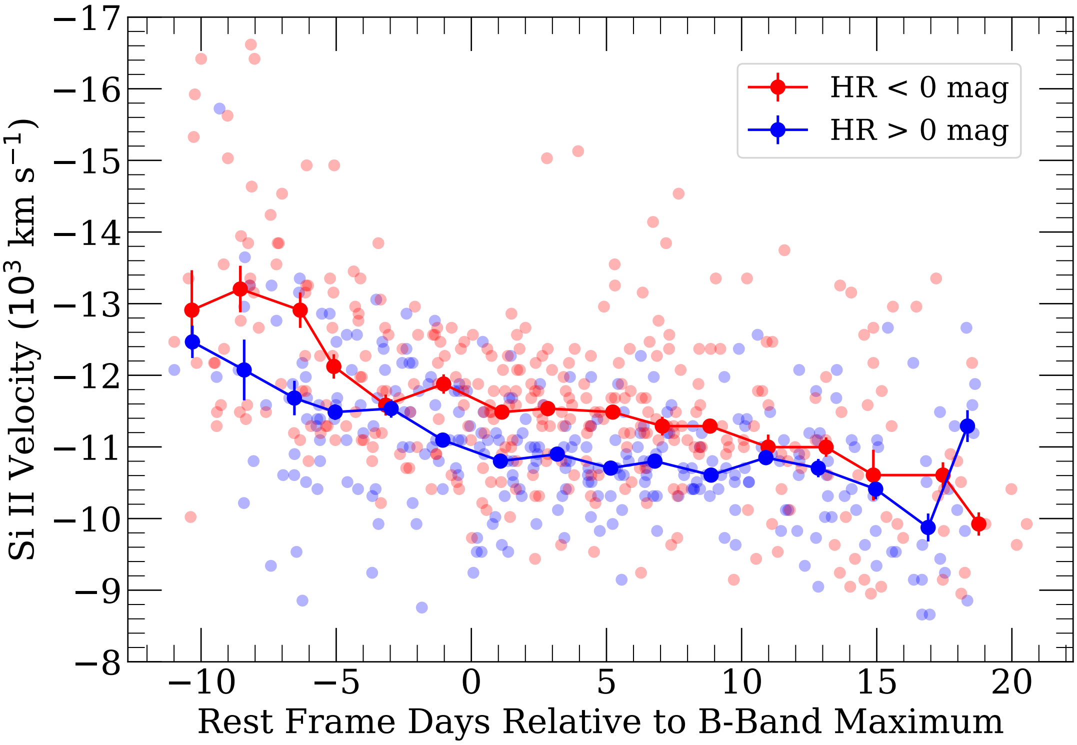

Figure 3.11: Si II velocity evolution for the HR sample. Individual points are measurements made from individual spectra. Solid connected points are binned medians using the bin sizes of 2 days and the error bars are the median absolute differences, dividing by the square-root of the number of points in a bin, for each bin. Blue and red points correspond to measurements from SNe in the positive-HR and negative-HR samples, respectively. We estimate that the negative-HR sample has a mean velocity that is at least 500 km s^{-1} larger than the negative-HR sample at the 2.8σ level.

52 and 62 SNe, respectively. From the full sample, we randomly generate two samples of SNe with these sample sizes. Each SN maintains all of its original velocity measurements. In our original measurements, the negative-HR sample has a higher median velocity in 14 out of 16 phase bins and has a median ejecta velocity higher by at least 500 km s^{-1} in 9 out of 16 phase bins. We find that the mock negative-HR sample produces a similar distribution of velocity residuals by chance in only 0.6% of trials.

3.4.2 Impact of SALT2 Corrections

We examine the impact of the velocity difference on distance modulus biases and cosmological analyses. In Figure 3.12 we present the maximum-light HR-binned composite spectra from Figure 3.2 focusing on the Si II λ6355 feature. As in Figure 3.2, the top to bottom sets of positive-HR (blue) and negative-HR (red) composite spectra have increasing corrections applied before calculating HRs.

We find that for both the x_1 and c-corrected and x_1, c, and γ-corrected composite spectra, the negative-HR composite spectra clearly have a higher $v_{\mathrm{Si\ II}}$ than positive-HR composite spectra. This means that the effect is present regardless of if a host-mass step (γ) correction is applied. Additionally, we are not introducing a velocity-HR correlation when accounting for the host-mass step. When we only apply the x_1 correction (third set of composite spectra), the velocity difference between the HR bins disappears indicating that, if there is still a velocity effect, it is not a dominant influence on HRs.

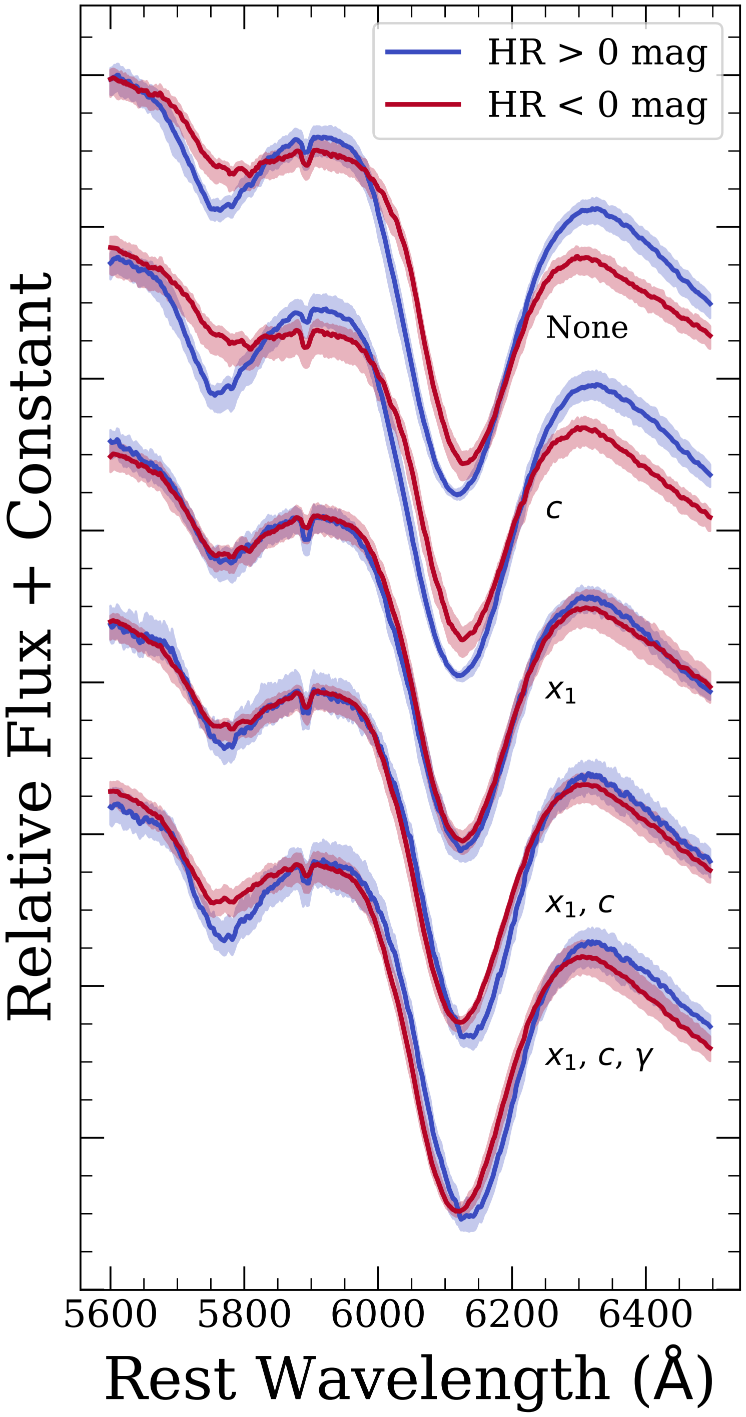

Figure 3.12: Same as Figure 3.2 but zoomed in on the Si II $\lambda6355$ feature.

3.4.3 Consistency with Predictions from FSK11

The trend between HR and velocity has important implications for cosmological analyses. Here we quantify the improvement of precision obtained by applying the velocity step presented in Figure 3.5.

The intrinsic HR scatter for a sample is defined as the additional uncertainty required to achieve $\chi^2_\nu = 1$. The intrinsic scatter in the +4-day sample improves from 0.094 mag to 0.082 mag after applying the velocity step. This improves the distance precision of each SN by 20%. However, this result is not significant (0.5σ). While potentially intriguing, this result is also still consistent with Blondin et al. (2011) and Silverman et al. (2012c), who found a <10% improvement in the HR weighted root-mean square (WRMS) when accounting for SN Ia maximum-light velocities. Despite the small improvement, Blondin et al. (2011) found evidence for a weak correlation between $v^0_{Si\ \mathrm{II}}$ and x_1/c-corrected HRs (absolute Pearson correlation coefficient of 0.40).

FSK11 noted a correlation between velocity and color (VCR), which could have implications for a HR bias. FSK11 measured an intrinsic color by comparing the color of a SN to the expected color for a SN with a similar light-curve shape corrected peak brightness that is only reddened and dimmed by dust. Deviations in color from the expected relationship were interpreted as intrinsic.

FSK11 found a linear correlation between Si II velocity at maximum light and $(B_{\mathrm{max}} - V_{\mathrm{max}})_0$, the intrinsic difference between maximum B- and V-band brightnesses (the velocity-color relationship; VCR). Specifically, they found

$$\begin{aligned}(B_{\max} - V_{\max})_0 = (-0.39 \pm 0.04) - (0.033 \pm 0.004) \\ \times \left(v^0_{\mathrm{Si\,II}}/1000 \text{ km s}^{-1}\right) .\end{aligned} \tag{3.2}$$

Since the SALT2 c parameter behaves in a similar way to $B - V$ color Guy et al. (2005), the VCR should produce, assuming SALT2 does not somehow account for this affect already, a step between low- and high-velocity SNe of

$$\mathrm{HR}_{\mathrm{low}} - \mathrm{HR}_{\mathrm{high}} \approx (0.033 \pm 0.004) \times \frac{v_{\mathrm{low}} - v_{\mathrm{high}}}{1000 \text{ km s}^{-1}} \times \beta, \tag{3.3}$$

where $\beta = 3.15$ and "low" and "high" subscripts correspond to average measurements from the $v_{\mathrm{Si\,II}} > -11{,}000$ km s^{-1} and $v_{\mathrm{Si\,II}} < -11{,}000$ km s^{-1} subsamples, respectively.

The prediction that higher-velocity SNe should have negative HRs is a direct prediction from the direction of the correlation between velocity and color and is independent of our measurements. However, we now use mean velocity measurements of the low- and high-velocity +4-day HR samples (−10,510 and −11,880 km s^{-1}, respectively) to estimate that VCR should produce a HR step of 0.14 ± 0.04 mag for our sample. This step size is consistent with the HR step that we observe (0.091 ± 0.025 mag) and has an important physical interpretation. Higher-velocity SNe Ia, which have redder intrinsic continua, are over-corrected for their color, making them appear closer away than they are. Notably, this would lead to corrected magnitudes that are brighter (negative-HR) than lower-velocity SNe Ia. Since the distribution of c values within our high- and low-velocity subsamples are very similar, we suggest that c does not fully account for intrinsic color differences due to velocity. The reduction in intrinsic scatter that we measure could indicate that chromatic scatter could account for ∼20% of the observed intrinsic scatter.

While our measurement is consistent with the prediction of FSK11, there is significant overlap between the FSK11 sample and the HR sample presented in this work. Although FSK11 did not examine HRs, it should not be surprising that we observed a similar HR offset *if* that offset is caused by VCR.

Given the VCR presented in Foley et al. (2011), we might expect the colors of our HR-binned composite spectra to be different. However, we do not see significant differences in the $B - V$ and $V - i$ colors curves presented in Figure 3.8. This may not be inconsistent since the continua are corrected using a reddening estimate from MLCS (Jha et al. 2007), while the HR is determined from SALT2 Guy et al. (2010). It is possible that MLCS, which attempts to separate intrinsic color and dust reddening is less affected by the VCR.

FK11 found that when using the rudimentary corrections of $\Delta m_{15}(B)$ and peak color, accounting for the VCR improved the HR scatter from 0.190 to 0.130 mag. By using velocity, our results do not rule out an improvement of this size. Again, this consistency is not unexpected since the samples in FK11 and this work are not completely independent.

3.5 Conclusions

We have used the open-source relational database `kaepora` to generate a variety of composite spectra with different average properties in order to investigate potential spectral variation with HRs. Using sets of composite spectra, we further examine how SNe Ia with different HRs differ spectroscopically. Our main results can be summarized as follows:

1. There are several spectral differences between SNe Ia with different HRs. This indicates both that current distance estimators that rely on photometric and host-galaxy measurements alone are not capturing the full physical diversity of SNe Ia and that measuring these spectral differences provides the possibility of improving distance measurements.

2. There exists a trend between Si II velocity and HR. Using a sample of 62 SNe Ia, we find that SNe with negative-HRs tend to have higher Si II $\lambda6355$ velocities. We measure a HR-Si II $\lambda6355$ velocity step at $-11,000$ km s^{-1} of 0.091 ± 0.035 mag. This step is consistent with a VCR (Foley et al. 2011), and correcting for the velocity step may improve distance precision by 20%.

3. Using all individual spectra ranging from -13 to $+22$ days, we find 2.8σ evidence for a Si II $\lambda6355$ velocity difference $>$500 km s^{-1} between the positive-HR and negative-HR samples at all epochs.

4. A similar velocity offset between positive-HR and negative-HR samples is observed at a variety of epochs and in multiple spectral features. For negative-HR compos-

ite spectra we observe larger blueshifts in Ca H&K, Si II λ4130, Si II λ5972 and λ6355, and the Ca II NIR triplet, and at phases of −9 to +15 days. The differences are apparent across the line feature, with the negative-HR spectra having broader features with bluer blue edges. In many different ways across phase, atomic species, and line profile, the negative-HR SNe have indications of higher ejecta velocity, making the above results more significant. Additionally, we use near-maximum light spectra to estimate $v^0_{\text{Si II}}$ for a sample of 115 SNe Ia. With these measurements we estimate a $v^0_{\text{Si II}}$-HR step of 0.068 ± 0.027 mag when sample intrinsic scatter is included in HR uncertainties.

5. Using our maximum-light composite spectra, we find that this velocity difference is apparent for HRs derived with and without accounting for the host-galaxy mass step. This indicates that the velocity difference is not induced by making this distance modulus correction, and the host-mass step is not caused by velocity.

6. At late epochs (+37 − 77 days) we observe that the negative-HR sample produce composite spectra that appear to have overall weaker spectral features than the positive-HR sample. This difference appears to strengthen with time, however, more spectra are needed validate this effect.

7. All results are consistent with a VCR (FSK11). In this scenario, high-velocity SNe Ia have intrinsically redder continua than low-velocity SNe. The redder continua is over-corrected using current distance estimators, causing a distance bias.

A velocity-HR step of ∼0.1 mag has important implications for cosmological analyses. Currently there is not significant evidence that the velocity distributions of SNe Ia evolve with redshift (Blondin et al. 2006; Foley 2012). However if the average velocity changes with redshift, we would introduce a systematic bias in our cosmological parameter estimates. We should gather more high-redshift spectra to further explore this effect. Specifically, we have presented evidence that the velocity-HR trend manifests as a velocity difference in numerous absorption features. These potential differences should be further explored in both low- and high-redshift samples. Also, Léget et al. (2019) recently developed SUGAR to improve the spectral description of SNe Ia. Using a “PCA-like” method, they showed that the second-most important factor was strongly correlated with Si II and S II velocity. The variation in this factor was also related to variation in color, and was not correlated with the SALT2 x_1 or c parameters. This supports our conclusion that SALT2 does not fully capture spectral variations associated with ejecta velocity.

Since ejecta velocity trends with HR, we encourage more spectral observations of SNe Ia, perhaps especially immediately after maximum light ($+2$ – $+7$ days) to provide the best unbiased distance measurements and to increase sample sizes. Since the VCR is consistent with our observations, it might be possible to glean additional distance information from color curves without directly measuring velocities. However with our current sample and techniques, we do not see significant differences in the $B-V$ or $V-i$ color curves of our HR-binned composite spectra at a variety of epochs. This indicates that spectra are likely needed to fully capture the velocity effect. While the spectral differences at later phases should be further explored, it is less feasible to get spectroscopic follow-up observations of SNe Ia in a cosmological sample at these late epochs.

Future cosmological experiments such as the Large Synoptic Survey Telescope (LSST) and the *Wide-Field InfraRed Space Telescope* (*WFIRST*) will discover and photometrically follow large samples of SNe Ia ($10^5 - 10^6$), but only a small fraction will have spectroscopy (Hounsell et al. 2018; The LSST Dark Energy Science Collaboration et al. 2018). Careful choices must be made, especially now that *WFIRST*'s spectroscopic capabilities are limited to a slitless prism and grisms, to fully sample the velocity distribution and to determine if that distribution changes with redshift. The velocity-HR effect must be analyzed in detail to properly plan for and leverage these experiments.

Chapter 4

Strong Calcium Emission Indicates that the Ultraviolet-Flashing Type Ia SN 2019yvq was the Result of a Sub-Chandrasekhar Mass

Double-Detonation Explosion

4.1 Introduction

Type Ia supernovae (SNe Ia) are energetic thermonuclear explosions that have produced roughly half of the iron conent of the local Universe (e.g., Tinsley 1980; Matteucci & Greggio 1986), shape and heat the interstellar medium (e.g., Springel & Hernquist 2003), and are excellent cosmological distance indicators from which we can constrain the nature of dark energy (e.g., Riess et al. 1998; Perlmutter et al. 1999; Scolnic et al. 2018; Jones et al. 2019). Major new facilities such as the Vera C. Rubin Observatory and the *Nancy Grace Roman Space Telescope* are being designed with SN Ia observations being a top priority (Spergel et al. 2015; Hounsell et al. 2018; Ivezić et al. 2019). Despite their critical importance in element creation, galaxy feedback, and cosmology, we still do not know the precise progenitor system and explosion mechanism for SNe Ia.

From both theory and observations, we know that SNe Ia come from C/O white dwarfs (WDs) in binary systems (Hoyle & Fowler 1960; Colgate & McKee 1969; Nomoto et al. 1984; Nugent et al. 2011; Bloom et al. 2012). The companion star may be another WD (i.e., the double-degenerate or DD scenario; Iben & Tutukov 1984; Webbink 1984) or a non-degenerate star (i.e., the single-degenerate or SD scenario; Whelan & Iben 1973; Iben & Tutukov 1996). There is strong observational evidence that DD progenitors are responsible for at least some individual SNe Ia (e.g., Li et al.

2011b; Schaefer & Pagnotta 2012; Kelly et al. 2014; Jacobson-Galán et al. 2018), while some SNe Ia almost certainly came from SD systems (e.g., Dilday et al. 2012; Graham et al. 2019; Kollmeier et al. 2019). Population studies also have somewhat conflicting results where SD and DD progenitor systems may produce SNe Ia at roughly similar rates (e.g., Maoz & Mannucci 2008; Foley et al. 2012c).

An additional dimension is the explosion mechanism. While the explosion must be triggered through mass transfer, this can be done quickly or slowly, with hydrogen or helium, and the explosion can start near the center of the star or at the surface, and the primary WD can vary in mass from about 0.7–1.4 $M_{\odot}$.

Despite the mélange of progenitor systems and explosion mechanisms, the near-peak luminosity spectral-energy distributions from multi-dimensional radiative-hydrodynamical explosion simulations appear generally similar to each other and observations. These predicted observables diverge some for epochs only a few days after explosion. In particular, some models predict a smooth increase in flux from explosion to peak, while others have "excess" flux relative to the smooth models for the first few days after explosion. In particular, this excess flux can be generated by interaction with a non-degenerate companion (if viewed from a particular position; Kasen 2010), interaction with circumstellar material (Raskin & Kasen 2013; Piro & Morozova 2016), a violent merger of two WDs (Kromer et al. 2016), radioactive ^{56}Ni in the outer layers of the ejecta (Piro & Morozova 2016; Noebauer et al. 2017), or a "double-detonation" where a surface He layer explosively burns, causing a second explosion in the interior of the WD (Woosley & Kasen 2011; Nomoto & Leung 2018; Polin et al. 2019).

Wide-field, high-cadence surveys have recently discovered several examples of SNe Ia with this signature (Marion et al. 2016; Hosseinzadeh et al. 2017; Dimitriadis et al. 2019a; Shappee et al. 2019) and additional peculiar thermonuclear WD SNe with excess flux (Cao et al. 2015; Jiang et al. 2017). While the different scenarios described above predict different durations, luminosities, and colors, the differences are subtle enough that current data sets cannot adequately distinguish between the scenarios (or the predictions all diverge significantly from the observations). However, these models predict vastly different observables at late times ($\gtrsim$150 days after explosion). In particular, interaction models predict strong H or He emission lines (Mattila et al. 2005; Leonard 2007a; Botyánszki et al. 2018), the violent merger should have significant unburned material and thus strong [O I] lines (Maeda et al. 2008; Taubenberger et al. 2009), while a double-detonation can have incomplete core burning and produce a significant amount of Ca throughout the ejecta leading to strong [Ca II] lines (Polin et al. 2021). Such analyses were performed for the normal SNe Ia 2017cbv and 2018oh that had early excess flux, but none of the signatures outlined above were seen (Sand et al. 2018; Dimitriadis et al. 2019b; Tucker et al. 2019).

While [O I] and Hα emission lines have been detected in nebular spectra of SNe 2010lp (Taubenberger et al. 2013b) and 2018fhw (Kollmeier et al. 2019; Vallely et al. 2019), respectively, there has not been an unambiguous detection of strong [Ca II] similar to predictions for models of double-detonations. The [Ca II] $\lambda\lambda$7291, 7324 doublet overlaps with the 7300 Å emission complex which is often understood to be the blending of [Fe II] and [Ni II] emission lines in normal SNe Ia. This feature appears stronger in low-luminosity SNe Ia and is likely caused by the additional presence of a [Ca II] component (Mazzali et al. 1997; Blondin et al. 2018). The detection of [Ca II] is further complicated by diversity in morphologies observed in the 7300 Å feature. This feature often exhibits multiple peaks which are commonly attributed to different elemental species, however, in some cases studies have suggested that asymmetric ejecta distributions could be the cause of double-peaked nebular features (Dong et al. 2015; Mazzali et al. 2018; Vallely et al. 2020).

Radiative transfer calculations of bare low-mass C/O WD detonations and double-detonations of WDs with thin He shells reproduce many of the photospheric properties of typical and low-luminosity SNe Ia (Shen et al. 2018a; Townsley et al. 2019). Specifically, the light curves presented in Shen et al. (2018a) exhibit a relationship between peak luminosity and decline rate that is in general agreement with the Phillips (1993) relation. Their synthetic spectra of normal and low-luminosity SNe Ia also show similar line ratios and velocities to observed SNe Ia. However, Polin et al. (2019) show that double-detonation explosions from progenitors with thin or thick He shells may produce a subclass of SNe Ia with distinct properties of velocity, color, and polarization (Cikota et al. 2019). They also show that massive He shells are needed in order to produce the early-time "flux excess" seen in several SNe Ia. These models also predict a strong component of [Ca II] emission in the nebular phase (Polin et al. 2021).

SN 2019yvq, which had a flash of ultraviolet and blue light a few days after explosion (Miller et al. 2020), provides an excellent opportunity to test these theories through its nebular spectrum. SN 2019yvq is relatively normal, but has some remarkable features in addition to its early light curve. In particular, it has a relatively low peak luminosity of $M_g \approx -18.5$ mag but high ejecta velocities (Miller et al. 2020). Nevertheless, SN 2019yvq is not so obviously distinct from typical SNe Ia as to be removed from cosmology samples. At a phase of 152.7 days after peak luminosity, we obtained a Keck spectrum of SN 2019yvq, which has strong [Ca II] emission unlike typical SNe Ia.

We present observations of SN 2019yvq, including the late-time Keck spectrum in Section 4.2. We compare SN 2019yvq to other SNe Ia and models in Section 4.3, demonstrating that SN 2019yvq was likely casued by a double-detonation explosion. We discuss the implications of our observations and conclude in Section 4.4.

Throughout this paper, we adopt the AB magnitude system, unless where noted, and 33.14 ± 0.11 mag as the distance modulus to NGC 4441 (the host galaxy of SN 2019yvq; Miller et al. 2020).

4.2 Observations & Data Reduction

We obtained two optical spectra of SN 2019yvq on 2020 Jun 17 UT, with the Low Resolution Imaging Spectrometer (LRIS; Oke et al. 1995), mounted on the 10-meter Keck I telescope at the W. M. Keck Observatory. At that date, the SN was ~153 rest-frame days past peak brightness (2020 Jan 15.25 UT; Miller et al. 2020). We observed SN 2019yvq with a low-resolution setting (1800 and 1430 s blue channel exposures with the B600/4000 grism and two 525 s red channel exposures with the R400/8500 grating, with pixel scales of 0.63 and 1.16 Å/pixel, respectively) and a high-resolution setting (two 825 s red channel exposures with the R1200/7500 grating, with a pixel scale of 0.4 Å/pixel). We used the 1.0″-wide slit and the D560 dichroic for all observations, and oriented the slit to include the host-galaxy nucleus. The atmospheric dispersion corrector unit was deployed. The low-resolution spectrum covers 3,400 – 10,056 Å, while the high-resolution spectrum covers 6,200 – 7,800 Å, including Hα, He I λ6678, [O I] $\lambda\lambda$6300, 6364 and the 7300 Å line complex, the primary focus of our current analysis. All data were reduced using standard IRAF[5] and python routines for bias/overscan corrections, flat fielding, flux calibration and telluric lines removal, using spectro-photometric standard star spectra, obtained the same night (Silverman et al. 2012b)

We present the low-resolution spectrum in Figure 4.1. The high-resolution spectrum is nearly identical other than its resolution and limited wavelength range.

The nebular spectrum of SN 2019yvq is generally similar to those of other SNe Ia at a similar epoch, including strong line emission from forbidden singly- and doubly-ionized Fe-group elements. At this epoch, the spectrum is likely still evolving, but the lack of obvious P-Cygni profiles indicates that the ejecta are mostly or completely optically thin.

Unlike other “normal” SNe Ia, SN 2019yvq has clear and strong [Ca II] $\lambda\lambda$7291, 7324 and Ca II NIR triplet emission. We discuss these feature, the connection to a double-detonation explosion, and the lack of signatures from other progenitor channels in the following sections.

---

[5] IRAF is distributed by the National Optical Astronomy Observatory, which is operated by the Association of Universities for Research in Astronomy (AURA) under a cooperative agreement with the National Science Foundation.

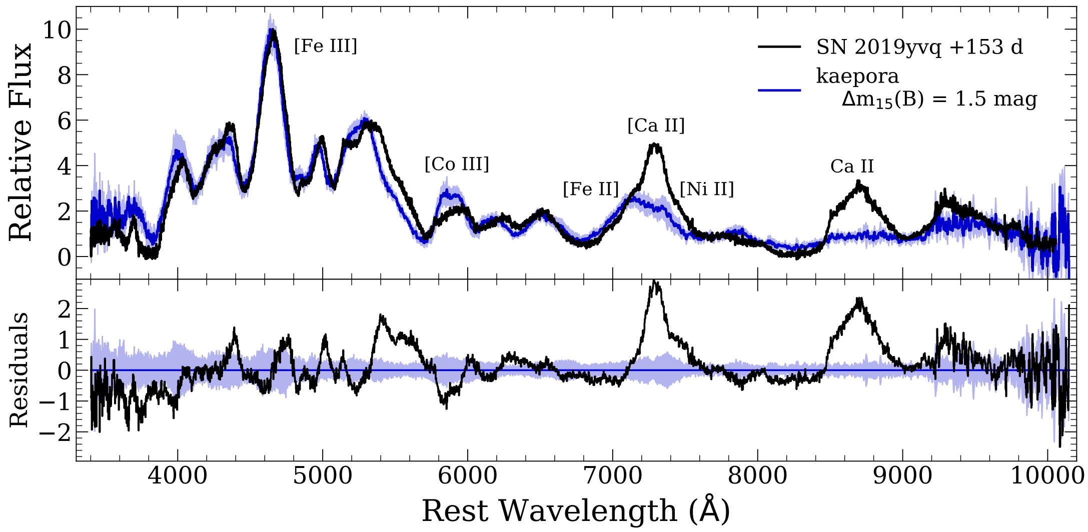

Figure 4.1: *Top Panel*: Spectrum of SN 2019yvq (black) observed 153 rest-frame days after peak brightness. The kaepora $\Delta m_{15}(B) = 1.5$ mag (the same decline rate as SN 2019yvq) composite spectrum (Siebert et al. 2019) is also displayed (blue) along with the $1-\sigma$ scatter of the spectra used to produce the composite spectrum. *Bottom Panel*: Residual spectrum of SN 2019yvq relative to the kaepora comparison spectrum.

4.3 Analysis

4.3.1 Photometric comparisons

SN 2019yvq had a lower peak luminosity than typical SNe Ia ($M_{g,\text{ peak}} \approx -18.5$ mag; Miller et al. 2020). Miller et al. (2020) measured a corresponding, relatively fast g-band ($\Delta m_{15}(g) = 1.3$ mag). Most historical SNe Ia lack a $\Delta m_{15}(g)$ measurement, and so it is difficult to make direct comparisons with other SNe Ia with similar light-curve shape. Miller et al. (2020) used the Yao et al. (2019) relationship between $\Delta m_{15}(g)$ and $\Delta m_{15}(B)$ to estimate $\Delta m_{15}(B) \gtrsim 1.6$ mag for SN 2019yvq. This analysis was limited by the lack of fast-declining SNe Ia in the Yao et al. (2019) sample, preventing a precise measurement.

Using a sample of SNe Ia with both g and B light curves (Folatelli et al. 2013b), we select a subset of five SNe Ia with similar g-band light curves. These SNe Ia have an average $\Delta m_{15}(B) = 1.54$ mag with an RMS of 0.07 mag, consistent with the Miller et al. (2020) estimate. We use our derived estimate as the B-band decline rate for SN 2019yvq.

4.3.2 Spectroscopic comparisons

Using the methods of Siebert et al. (2019), we generate a composite spectrum using kaepora[6] to best match the phase and decline rate of SN 2019yvq and compare in Figure 4.1. Aside from the clear Ca emission, SN 2019yvq has remarkably similar line shifts, line widths, and relative feature strengths to those in the kaepora $\Delta m_{15}(B) = 1.5$ mag composite spectrum.

While the optical spectrum of SN 2019yvq at +153 days is generally similar to other SN Ia spectra at similar epochs, the morphology of the 7300 Å line complex is unique compared to all other known SN Ia nebular spectra. In Figure 4.2 we compare this spectrum to a diverse set of SN Ia nebular spectra. The SN 2019yvq spectrum is similar to those of typical SNe Ia and composite spectra in regions without Ca emission. While some peculiar SNe Ia appear more similar to SN 2019yvq in wavelength regions corresponding to Ca emission, their spectra are less similar at other wavelengths.

Examining the peculiar SNe Ia in more detail, we highlight similarities and differences with SN 2019yvq. Figure 4.2 displays spectra from SNe 1999by ($M_{B,\text{ peak}} = -17.2$ mag; Garnavich et al. 2004), a low-luminosity SN 1991bg-like SN Ia; 2010lp

---

[6] `https://msiebert1.github.io/kaepora/`

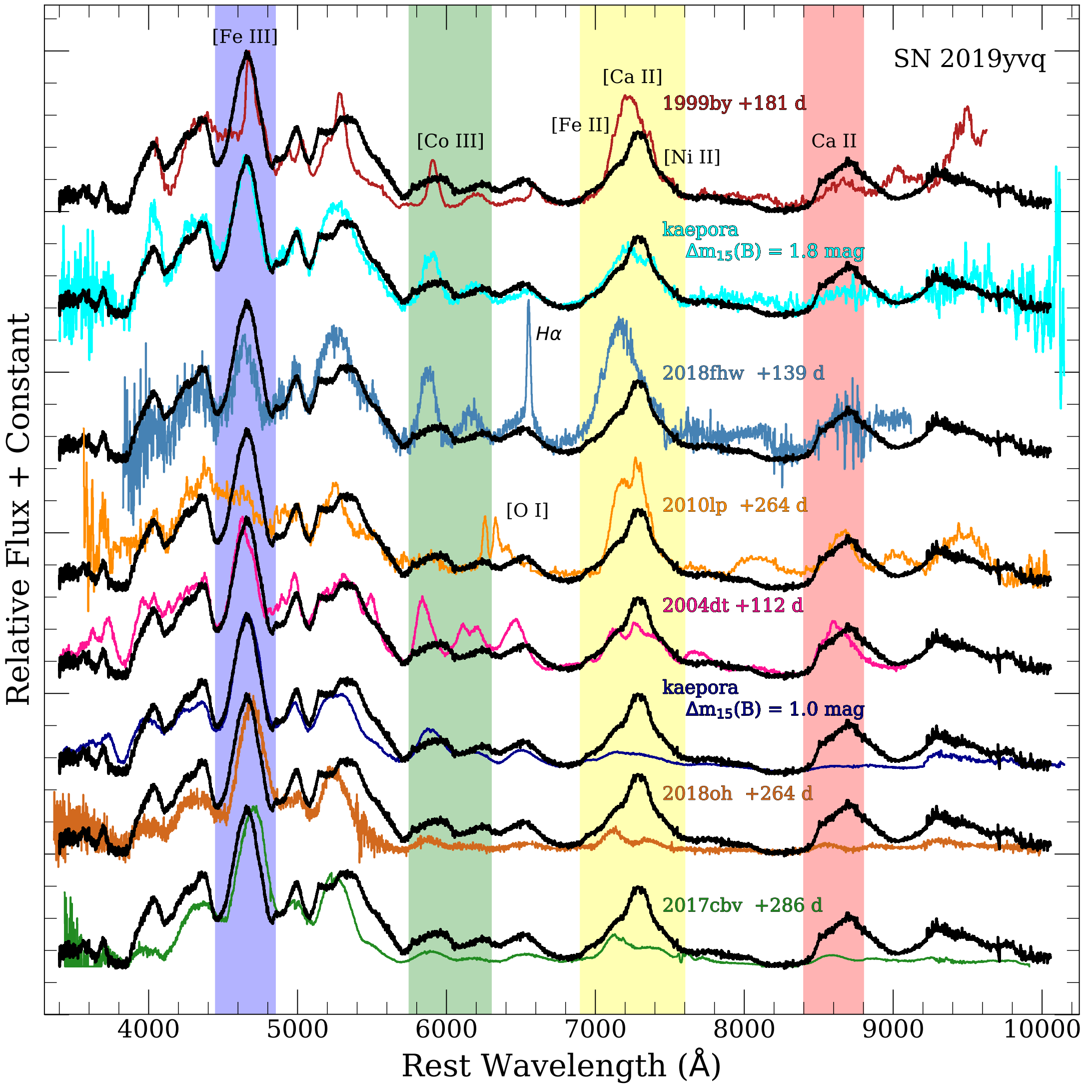

Figure 4.2: Optical spectrum of SN 2019yvq (black curve) at +153 days after peak brightness compared to those of other SNe Ia at similar phases. From top to bottom we compare to scaled nebular spectra of the SN 1991bg-like SN 1999by (red); the kaepora composite spectrum with $\Delta m_{15}(B) = 1.8$ mag (cyan); SN 2018fhw, which had late-time Hα emission (blue); SN 2010lp, a peculiar SN 2002es-like SN which had nebular [O I] emission (orange), we have clipped emission lines from the host galaxy for better visualization; the high-polarization and peculiar SN 2004dt (fucsia); the kaepora composite spectrum with $\Delta m_{15}(B) = 1.0$ mag (dark blue); SN 2018oh, which had an early-time flux excess (dark orange); and SN 2017cbv, which also had an early-time flux excess (green). Several spectral regions are highlighted: [Fe III] λ4701 (blue); [Co III] λ5888; the feature at 7300 Å complex which includes possible contributions from [Fe II] λ7155, [Ni II] λ7378, and [Ca II] $\lambda\lambda$7291, 7324 (yellow); and the Ca II NIR triplet (red).

($M_{B,\text{ peak}} = -17.7$ mag; Kromer et al. 2013; Pignata et al., in preparation), a peculiar SN 2002es-like (Ganeshalingam et al. 2012) SN Ia that had strong [O I] $\lambda\lambda$6300, 6364 emission in its late-time spectrum (Taubenberger et al. 2013a) indicating significant unburned material; and 2018fhw ($M_{B,\text{ peak}} = -17.7$ mag; Kollmeier et al. 2019), which had strong Hα emission in its late-time spectrum indicating circumstellar interaction (Kollmeier et al. 2019; Vallely et al. 2019). The nebular spectra of SNe 1999by and 2018fhw are very similar overall, except for the strong Hα emission seen for SN 2018fhw. These spectra show the general trends seen in other SN 1991bg-like nebular spectra of narrower features, stronger [Co III] emission relative to [Fe III], and a stronger 7300 Å emission complex. SN 2010lp is somewhat different with very weak (perhaps absent) [Fe III] emission, but shares other characteristics. Other than the strong emission near 7300 Å, the SN 2019yvq spectrum does not have the distinct properties of low-luminosity SN Ia spectra, including the peculiar SNe 2010lp and 2018fhw. Of these comparison spectra, the kaepora composite spectrum with $\Delta m_{15}(B) = 1.8$ mag best reproduces the ratio of the 7300 Å line complex to the [Fe III] peak, and it is possible that the SNe contributing to the composite spectrum contain a similar contribution from [Ca II] as for SN 2019yvq.

Alternatively, Figure 4.2 also compares the spectrum of SN 2019yvq to higher-luminosity SNe Ia, including some relatively peculiar SNe. We compare to SNe 2004dt, a high-velocity and high-polarization SN Ia (Wang et al. 2006; Altavilla et al. 2007) that is an outlier when comparing its peak-light velocity gradient and nebular-line velocity shifts (Maeda et al. 2010a); 2017cbv, which had an early blue flux excess days after explosion (Hosseinzadeh et al. 2017); and 2018oh, which also had a distinct flux excess at early times (Dimitriadis et al. 2019a; Shappee et al. 2019). Except for the Ca features, the SN 2019yvq spectrum is similar to that of these comparison SNe (although SN 2004dt shows more differences, which may be caused by its relatively early phase). We also compare the SN 2019yvq spectrum to a kaepora composite spectrum with $\Delta m_{15}(B) = 1.0$ mag showing striking similarity except for the Ca emission. We note that the flux at ∼5500 Å appears to be strongly correlated with phase. SN 2019yvq shows the best agreement in this wavelength range with SNe 2018fhw and SN 2004dt, which have phases of 139 and 112 days, respectively, significantly earlier than many of the other comparison spectra.

The width and relative strength of [Fe III] λ4701 in SN 2019yvq is most similar to SNe 2004dt, 2011fe, and 2017cbv. Both SN 2019yvq and SN 2017cbv exhibited early blue bumps in their light-curves, however, only SN 2019yvq shows prominent Ca II features. Of the SNe displayed, only SNe 2004dt, 2010lp, and 2019yvq show prominent Ca II near-infrared triplet emission.

We examine the 7300 Å emission feature in detail in Figure 4.3. The spectra of the higher-luminosity comparison SNe (SNe 2011fe, 2017cbv, 2018oh, and the kaepora $\Delta m_{15}(B) = 1.0$ mag composite spectrum) are distinct from that of SN 2019yvq with the comparison spectra having obvious [Fe II] and [Ni II], but lacking significant [Ca II] emission. This is in contrast to SN 2019yvq, which has strong [Ca II] emission in addition to the [Fe II] and [Ni II] emission.

In Figure 4.3, we also display the 7300 Å emission feature, comparing SN 2019yvq

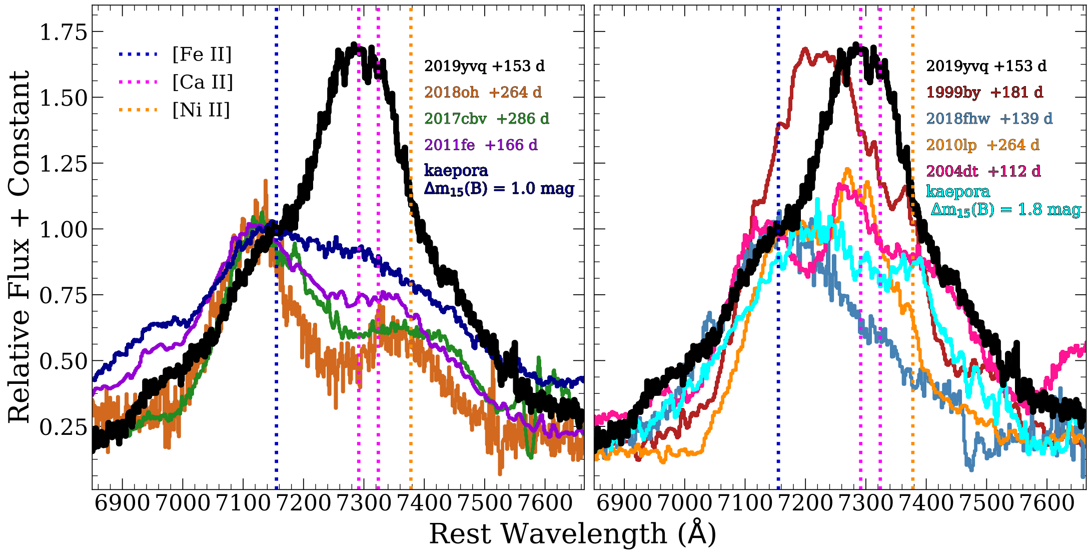

Figure 4.3: (*left panel*): Comparison of the 7300 Å line complex of higher-luminosity SNe (SNe 2011fe, 2017cbv, 2018oh, and the kaepora $\Delta m_{15}(B) = 1.0$ mag composite spectrum). These spectra have been scaled such that their peak [Fe II] flux match the the peak of the [Fe II] component in SN 2019yvq. (*right panel*): Comparison of the 7300 Å line complex of SNe that may have strong [Ca II] components (SN 1999by, SN 2018fhw, SN 2010lp, and SN 2004dt). The 7300Å line complex in SN 2018fhw and SN 1999by is relatively dominant in comparison to [Fe III] as shown in Figure 4.2. Thus these spectra have been scaled such that their peak [Ca II] flux matches the the peak of the [Ca II] component in SN 2019yvq and SN 2004dt and SN 2010lp have been scaled to match the [Fe II] emission. The rest wavelengths of prominent Fe II, Ca II, and Ni II are displayed as vertical dashed lines in both panels.

to the lower-luminosity and peculiar SNe Ia from Figure 4.2. Each of these SNe has possible [Ca II] emission, but all comparison spectra are still distinct from the SN 2019yvq spectrum. In particular, SNe 1999by and 2018fhw have strong emission peaking around 7220 and 7160 Å, respectively, much bluer than SN 2019yvq, which peaks at 7287 Å. While it is possible SNe 1999by and 2018fhw have strong [Ca II] $\lambda\lambda$7291, 7324 emission, the emitting material would be blueshifted by -3500 and -5900 $\mathrm{km\,s^{-1}}$, respectively, which would be some of the highest velocity shifts seen for a SN Ia (Maeda et al. 2010b; Maguire et al. 2018), and is inconsistent with shifts from other spectral features. Instead, it is more likely that there is significant contribution from [Fe II] λ7155.

SNe 2004dt and 2010lp have more obvious [Ca II] $\lambda\lambda$7291, 7324 emission with peaks at ∼7290 Å, corresponding to velocity shifts of -1400 and -1100 $\mathrm{km\,s^{-1}}$, respectively. However, SN 2019yvq has significantly stronger [Ca II] emission relative to [Fe II] and [Ni II] than SNe 2004dt and 2010lp. We also caution that SN 2004dt has significant velocity offsets and polarization, and it is possible that the emission peak for that particular spectrum is caused by an asymmetric and kinematically extreme ejecta distribution.

There is a general trend between peak luminosity and the 7300 Å profile shape with lower-luminosity SNe Ia having stronger emission at these wavelengths relative to other features (see Figure 4.2; Polin et al. 2021). SN 2019yvq conforms to this trend. However, no other SN Ia is so sufficiently dominated by [Ca II] emission at these wavelengths.

SN 2019yvq has a similar [Ca II]/[Fe II] strength to some SNe Iax (Foley et al.

2016a), albeit the lines have much larger velocity widths for SN 2019yvq. Other (presumably) white-dwarf SNe such as Ca-rich SNe (e.g., Perets et al. 2010) and SN 2016hnk (Jacobson-Galán et al. 2020) also have strong [Ca II] emission at late times, but are generally different from SN 2019yvq and SNe Ia in most regards (e.g., peak luminosity, light-curve behavior, He abundance).

The blue and red slopes of the Ca-deficient spectra in this wavelength range seem to agree well with the shoulders of the line complex of SN 2019yvq. Additionally, the spectrum of SN 2011fe and the kaepora composite spectrum with $\Delta m_{15}(B) = 1.0$ mag show some evidence for excess emission from 6900-7050 Å. These spectra have phases of +166 days and +140 days, respectively, which are very similar to the spectrum of SN 2019yvq at +153 days. Therefore, this could be a feature that is more likely to be observed at early times. All of the Ca-deficient spectra have [Fe II] emission components that appear blueshifted relative to SN 2019yvq.

4.3.3 Fitting the 7300 Å Line Complex

The complicated morphology of the 7300 Å line complex allows us to decompose it into emission from different species. Doing this, we can examine the contribution from [Ca II].

We fit this feature using the following methodology. First, we smooth the spectrum with a 15 Å scale and choose continuum points on the red and blue sides of the feature. We divide by this linear continuum and use Gaussian profiles to approximate the forbidden line emission from [Fe II], [Ca II], and [Ni II]. For this analysis we assume that the following lines dominate this fitting region: [Fe II] (7155, 7172, 7388, 7453 Å),

Table 4.1: Parameters for Multiple-Gaussian Decomposition of the 7300 Å line Profile

Species	Velocity Offset (km s^{-1})	Width (km s^{-1})
Fe II	-1210 ± 90	4170 ± 70
Ni II	-1210 ± 90	3960 ± 20
Ca II	-600 ± 90	2400 ± 40

[Ca II] (7291, 7324 Å), and [Ni II] (7378, 7412Å). We used the rest wavelengths and transition probabilities from the NIST Atomic Spectra Database[7]. The strengths of lines for each element are defined relative to the strongest line, which is a single free parameter for each species. We assume that lines produced by unique ionization states of each element are produced in the same regions of the ejecta, and we therefore require that the velocity offsets and widths relative to the rest-frame wavelength of each line be the same for lines coming from the same species. Since [Fe II] and [Ni II] emission are likely produced in the same region of the ejecta (Maeda et al. 2010b), we fit for a single [Fe II] and [Ni II] velocity offset. Thus, we fit for a total of 8 parameters: the emission strength, velocity offset ([Fe II] and [Ni II], and [Ca II]), and velocity width of each species. To estimate uncertainties for these parameters, we performed a simple Monte-Carlo algorithm to vary the blue and red continuum points randomly by up to 100 Å and repeating the analysis

Figure 4.4 displays the best-fit Gaussian component model to the 7300 Å line complex. The best-fit values of velocity offsets and widths are presented in Table 4.1. This simple model matches the line profile extremely well.

To match the data and in particular the peak of the emission, a strong [Ca II]

---

[7] `https://www.nist.gov/pml/atomic-spectra-database`

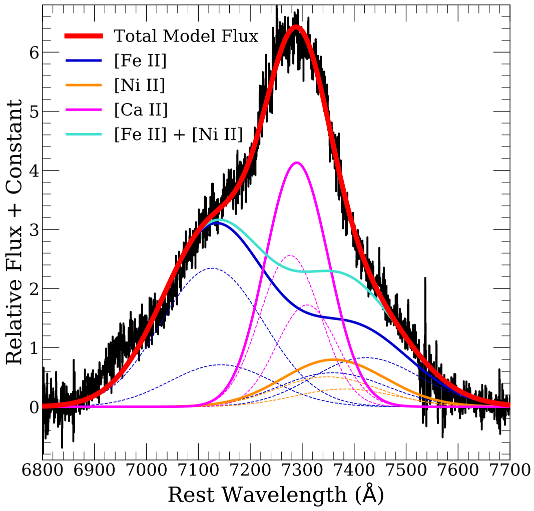

Figure 4.4: Multiple Gaussian-component fit (red) to the 7300 Å line complex in the LRIS high-resolution nebular spectrum of SN 2019yvq (black). Emission from the [Fe II], [Ni II], and [Ca II] and shown as solid blue, teal, and magenta curves, respectively, while dotted lines represent the emission from individual line transitions. A strong [Ca II] emission component is needed to reproduce explain the emission seen for SN 2019yvq.

component is necessary. Since Fe-group elements are expected to be produced in similar regions of the ejecta, it is reassuring that our fit produces similar velocity widths for [Fe II] and [Ni II] (4400 ± 100 and 3910 ± 40 $\mathrm{km\,s^{-1}}$, respectively). Additionally, the relative strength of [Fe II] to [Ni II] is consistent with other fits in the literature that use similar methods to fit this feature (Maguire et al. 2018). The sum of the the [Fe II] and [Ni II] components result in a profile that is qualitatively similar to 7300 Å line profiles of typical SNe Ia at similar epochs. In particular, the kaepora $\Delta m_{15}(B) = 1.0$ mag composite spectrum, and the nebular spectrum of SN 2011fe (Figure 4.3, left panel, blue curve and purple curve, respectively) have the most similar morphology to our [Fe II] + [Ni II] component. Similar to the nebular spectrum of SN 2019yvq at +153 days, the kaepora $\Delta m_{15}(B) = 1.0$ mag composite spectrum has a effective phase of

+138 days, and the SN 2011fe spectrum is at +166 days.

All three species (Fe II, Ni II, and Ca II) are blueshifted relative to the rest frame. Maeda et al. (2010b) found that nebular line shifts are correlated with velocity gradient. Blondin et al. (2012b), Silverman et al. (2013b), and Maguire et al. (2018) supported this result by showing that high-velocity SNe Ia are more likely to have redshifted nebular lines. Given that SN 2019yvq exhibited a high ejecta velocity at peak brightness of about $-15{,}000\ \mathrm{km\,s^{-1}}$ (Miller et al. 2020), a blueshifted nebular velocity is atypical — similar to how its red intrinsic color at peak is atypical for this high velocity (Foley & Kasen 2011; Foley et al. 2011).

The full complex of SN 2019yvq cannot be fit without [Ca II] emission, unlike what is seen for most SNe Ia (e.g., Maguire et al. 2018; Flörs et al. 2020). Furthermore, the additional presence of strong Ca II near-infrared triplet emission provides more evidence that the strong component of the 7300 Å line profile is caused by [Ca II]. Other low-luminosity SNe Ia such as SNe 1991bg and 1999by have strong emission in this region reminiscent of SN 2019yvq and this is often attributed to [Ca II] (e.g., Filippenko et al. 1992b; Turatto et al. 1996), it is not easily reproduced by (only) [Ca II] (Mazzali et al. 1997). However, Blondin et al. (2018) presented model spectra of SN 1999by where [Ca II] dominated this feature with an additional strong component from [Ar III] λ7136. Currently there is no unambiguous, dominant [Ca II] emission in a SN 1991bg-like SN Ia. Moreover, [Ar III] λ7136 is not a strong line in the SN 2019yvq spectrum.

Alternatively, [Ca II] has been clearly detected in several peculiar SNe Ia and

SNe Iax (Taubenberger et al. 2013b; Foley et al. 2016a; Galbany et al. 2019; Jacobson-Galán et al. 2020), indicating that this feature is detectable at the expected wavelength under the correct physical conditions. SN 2016hnk and SNe Iax are both connected to He burning (Foley et al. 2013, 2016a; Jacobson-Galan et al. 2019a; Jacobson-Galán et al. 2020), perhaps further indicating SN 2019yvq is the result of a double-detonation.

Wilk et al. (2020) argued that the presence of [Ca II] blended with the 7300 Å line complex allows for the constraint of the ionization ratio. They suggest that for $N(\mathrm{Fe}^{+})/N(\mathrm{Ca}^{+}) \geq 50$, [Fe II] is expected to dominate this feature yet for $N(\mathrm{Fe}^{+})/N(\mathrm{Ca}^{+}) \leq 100$ prominent [Ca II] blending is expected. Thus, the unambiguous detection of both [Fe II] and [Ca II] in SN 2019yvq may allow us to constrain the number ratio of ionized Fe to Ca, $N(\mathrm{Fe}^{+})/N(\mathrm{Ca}^{+})$, to between 50 and 100. Wilk et al. (2020) also found that significant clumping of the ejecta is a natural way to decrease ionization resulting in stronger Ca emission as [Ca II] becomes the dominant cooling for regions rich in IMEs.

4.3.4 Mass Limits For Swept-up Circumstellar Material

A visual inspection of the late-time SN 2019yvq spectra shows no obvious hydrogen or helium emission at the redshift of the SN. We can, alternatively, constrain the amount of swept-up material from a potential companion to the exploding WD, following the procedure described in several SNe-Ia nebular studies (Mattila et al. 2005; Leonard 2007a; Shappee et al. 2013; Maguire et al. 2016; Graham et al. 2017; Sand et al. 2018; Dimitriadis et al. 2019b; Tucker et al. 2020) as follows: Firstly, we estimate the brightness of SN 2019yvq at +200 days past explosion in order to compare our data with

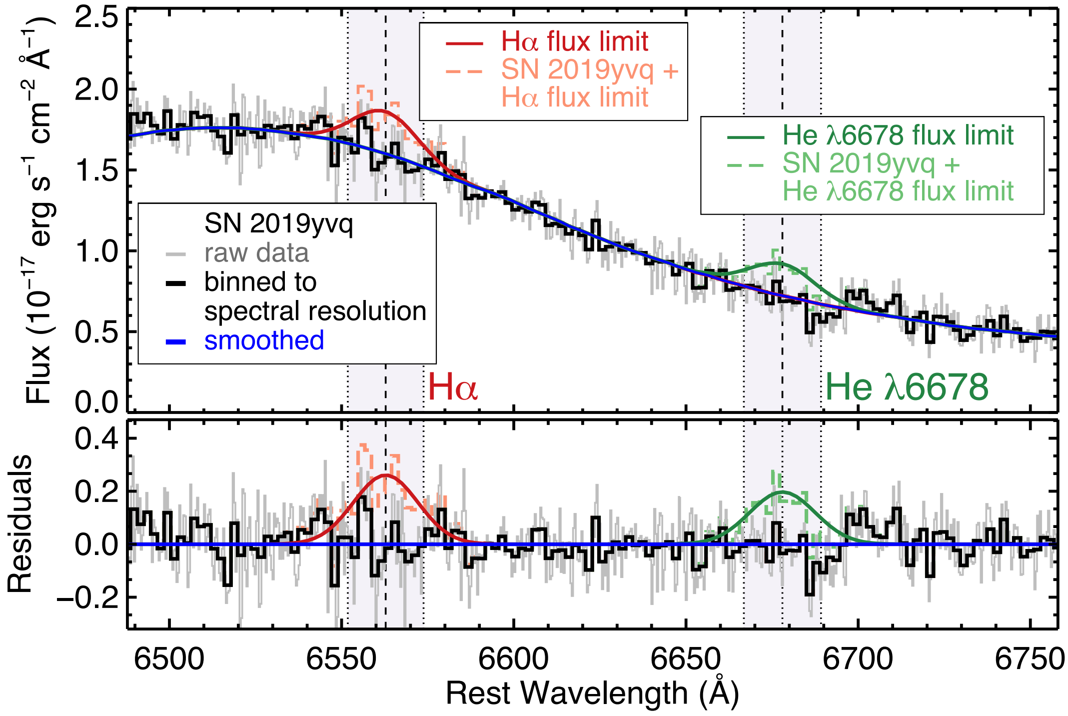

Figure 4.5: The LRIS high resolution spectrum of SN 2019yvq, at the spectral region of Hα and He I λ6678. The solid gray line corresponds to the raw data, and the solid black line to the raw data binned to the spectral resolution. The underlying continuum is shown as a solid blue line. The gray-shaded region corresponds the ±22 Å (1000 km s^{-1}) region around the rest wavelength of each line. Solid red and green lines represent the artificially-inserted Hα and He I λ6678 features, corresponding to our 3-σ detection limit above the smoothed continuum, with the dashed red and green lines showing how these features would appear in our spectrum. On the bottom panel, we additionally show the residuals relative to the continuum.

the models from Botyánszki et al. (2018). While our spectrum was taken at ∼170 days from explosion, the late-time spectral features of SNe Ia do not change significantly between these epochs, thus the general spectral shape of SN 2019yvq at +200 days should be similar. We use the public $g_{\rm ZTF}$ and $r_{\rm ZTF}$ photometry after +60 days from maximum, when the SN is in the radioactive cobalt decay regime, correct for MW and host extinction (using the values from Miller et al. 2020) and linearly fit, estimating $g_{+200\ \rm d} = 19.67 \pm 0.10$ mag and $r_{+200\ \rm d} = 20.77 \pm 0.14$ mag. Finally, we warp our late-time spectrum to match these estimated photometric colors.

To determine the mass limits, we follow the procedure outlined by Dimitriadis et al. (2019b). Briefly, using the flux-calibrated, extinction- and redshift-corrected spectrum, we bin to the spectral resolution. Our high-resolution spectrum has FWHM spectral resolution of ∼1.95 Å (as determined from isolated night-sky lines). The pixel scale is ∼0.4 Å, and thus not limiting the resolution. We determine the continuum by smoothing on a 195 Å scale. Comparing the smoothed spectrum to the unsmoothed version, we do not detect any significant emission features expected from the interaction scenario. Approximating possible emission features as Gaussians with FWHMs of $1000\ \rm km\,s^{-1}$, we determine the 3-σ flux limit. Using the luminosity distance from Miller et al. 2020, we estimate the Hα and He I $\lambda\lambda$6678 luminosity limits (at 200 days) to be 1.33 and 1.01×10^{37} erg s^{-1}, respectively. Using Equation 1 of Botyánszki et al. (2018), we convert these luminosity limits to mass limits, and we determine that SN 2019yvq had stripped hydrogen and helium mass of $<4.0 \times 10^{-4}$ and 3.4×10^{-4} $\rm M_{\odot}$, respectively. These results are displayed in Figure 4.5.

4.3.5 Comparison to Double-Detonation Model

In this section we examine SN 2019yvq in the context of double-detonation explosions. The double-detonation scenario requires a WD to accrete a surface shell of helium from a binary companion. An ignition in this helium shell can send a shock front into the WD which ignites the C/O core when it converges (Woosley & Weaver 1994; Nomoto 1982). The double-detonation mechanism has been considered as a possible channel for some Type Ia SNe, and recently the presence of strong [Ca II] emission has been pointed to as an identifying signature of these explosions in the nebular phase (Polin et al. 2021).

We compare the event to the explosion models of Polin et al. (2019) who use the hydrodynamics code `Castro` (Almgren et al. 2010) to simulated double-detonation explosions for a large parameter space of WD and He shell masses. Polin et al. (2021) examines these explosion models in the nebular phase using the radiation transport code `Sedona` (Kasen et al. 2006) paired with the NLTE nebular tool `SedoNeb` (Botyánszki & Kasen 2017) to evolve the homologus ejecta to nebular times while calculating the gamma-ray transport of radioactive decay products. Then `SedoNeb` is used to calculate the emissivities of each atomic transition by solving for the temperature, ionization state, and NLTE level populations. The final step is to integrate this emission to determine the wavelength-dependent flux.

Miller et al. (2020) examined the Polin et al. (2019) models to determine the consistency of SN 2019yvq with a double-detonation explosion given the observational properties in the photospheric phase. The best-fit model, a 0.92 $M_\odot$ WD with a

0.04 $\mathrm{M}_\odot$ Helium shell (or a total mass of $M_{\mathrm{tot}} = 0.96\ \mathrm{M}_\odot$), was able to explain most, though not all of the features of SN 2019yvq. Specifically the models showed that a double-detonation can produce the early UV flash exhibited by SN 2019yvq and the best 0.92+0.04 model reproduced the optical brightness during the early flux excess period and at peak brightness. The model, however, struggled to reproduce the velocity evolution of SN 2019yvq exhibiting significantly slower Si II absorption features than the observed event.

There is an inherent velocity-luminosity relationship in the 1D double-detonation models of Polin et al. (2019). As a consequence of the WD exploding purely as a detonation the amount of ^{56}Ni created during core burning is simply a function of the central density (or total mass) of the progenitor. The amount of ^{56}Ni determines both the peak luminosity of the transient as well as the kinetic energy allowing for the velocity-luminosity relationship to result from a one-parameter function determined by the total mass of the progenitor.

Polin et al. (2019) further points to a population of SNe Ia that follow this relationship and a separate group of SNe Ia that have $M_B = -19.5$ mag and a peak-brightness Si II λ6355 velocity around -11,000 $\mathrm{km\,s^{-1}}$. This cluster contains most normal SNe Ia, such as SN 2011fe, indicating these are likely not of double-detonation origin. This relationship is, however, based on a set of 1D simulations and has the potential to become more complicated when multi-dimensional effects are introduced. Furthermore, SN 2019yvq does not follow this relationship, having fast ejecta velocity at peak ($v_{\mathrm{Si\ II}} \approx -15{,}000\ \mathrm{km\,s^{-1}}$) that is associated with a high-mass WD, paired with a low luminosity ($M_{g,\text{ peak}} \approx -18.5$ mag) that is associated with a low-mass WD. This combination is not just peculiar in the context of a double detonation, but for all SNe Ia. SN 2019yvq does not lie in the cluster of normal SNe Ia but rather in a relatively un-populated regime in this parameter space (Miller et al. 2020).

Because of the favored photospheric double-denotation model's inability to explain the velocity evolution of SN 2019yvq, we chose to compare our nebular spectrum to the entire suite of Polin et al. (2021) models as well as the best-fit model from Miller et al. (2020) to independently determine which model best matches the nebular features of SN 2019yvq. Figure 4.6 shows the result of this comparison. The best-matching photospheric model, $M_{\text{tot}} = 0.96$ $\text{M}_\odot$, has [Ca II] $\lambda\lambda$ 7291, 7324 emission that is much stronger than that of SN 2019yvq, while the best-matched nebular model, $M_{tot} = 1.15$ $\text{M}_\odot$ (determined by the [Ca II]/[Fe III] ratio) is too luminous in the photospheric phase.

The [Ca II] emission feature is highly sensitive to both the precise amount of Ca produced in the explosion and the distribution of that Ca throughout the ejecta (Polin et al. 2021). [Ca II] is a very efficient cooling line, and tends to dominate the emission features when Ca is co-existent with other coolants. The over production of [Ca II] in the $M_{\text{tot}} = 0.96$ $\text{M}_\odot$ model could indicate that the 1D double-detonation models distribute too much Ca in the innermost ejecta, allowing for some flux to cool through [Ca II] when it would otherwise cool through Fe-group elements. However, the $M_{\text{tot}} = 1.15$ $\text{M}_\odot$ model provides a better match to the velocity of SN 2019yvq, exhibiting a Si II λ 6355 of approximately $-14{,}500$ km s^{-1} at peak brightness, favoring

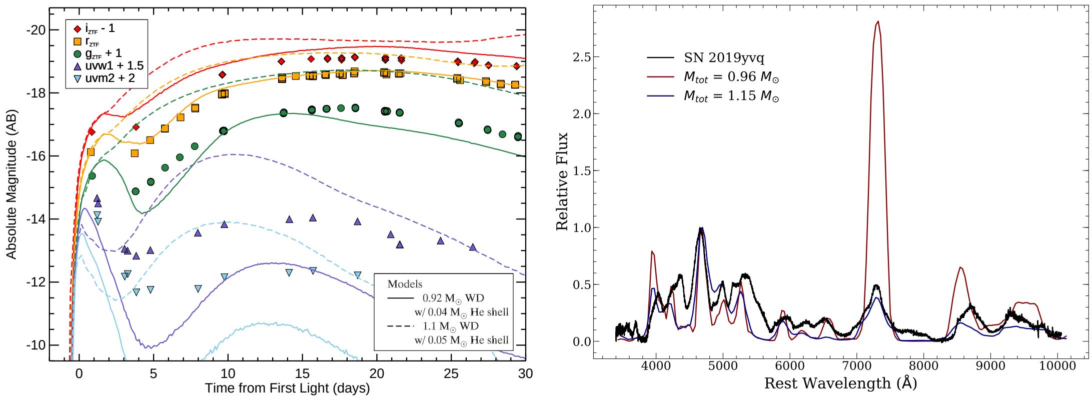

Figure 4.6: SN 2019yvq light curves (left) and nebular spectrum (right) compared with double-detonation models. The light curves of the Miller et al. (2020) model (a 0.92 $M_\odot$ WD with 0.04 $M_\odot$ He on its surface) are displayed as solid lines, while the spectrum is displayed as a red curve. The light curves of an additional model that is well matched to the nebular spectrum (a 1.1 $M_\odot$ WD with 0.05 $M_\odot$ He on its surface) is displayed as dashed curves, and its nebular spectrum is a blue curve. The Miller et al. (2020) model has nebular [Ca II] emission that is much stronger than observed. However, the model with the best-matching nebular spectrum is more luminous near peak than SN 2019yvq.

a higher-mass progenitor for SN 2019yvq.

It is also possible that this discrepancy is due to asymmetries in the explosion and line-of-sight differences not captured in our 1D models. Townsley et al. (2019) perform a 2D simulation of the double-detonation of a 1.0 $M_\odot$ WD with 0.02 $M_\odot$ He on its surface. They show that at the time of peak brightness the Si II velocity is fastest along the pole (in the direction of the initial helium ignition) and slower for viewing angles away from the pole. The bolometric luminosity behaves inversely, such that it is least luminous along the pole and most luminous when viewed from the opposite direction. It is possible that SN 2019yvq is viewed along a line of sight close to the pole, such that it exhibits the rare combination of high Si II velocity paired with lower luminosity. Future work is necessary to determine how such asymmetries would affect the nebular features of these events. We therefore suggest that while the presence of strong [Ca II] emission is enough to classify SN 2019yvq as a double-detonation explosion, the exact mass of the progenitor is less certain.

4.4 Discussion & Conclusions

We have gained significant insight about the SN 2019yvq progenitor system and explosion from its nebular spectrum. There are also broader implications for all SNe Ia. SN 2019yvq is another example of a "normal" SN Ia that exhibits an early blue flux excess, but the first with an atypical late-time spectrum.

In almost every case where there is an early flux excess for a SN Ia, and in all cases where the SN may be considered "normal," the nebular spectra had no obvious peculiarity. Similarly, the SNe Ia with peculiar nebular spectra generally lacked evidence of an early flux excess (often because of a lack of data covering the relevant epochs). The previous exception was the the atypical SN 2002es-like iPTF14atg that had both an early blue flash (Cao et al. 2015) and [O I] nebular emission (Kromer et al. 2016) similar to SN 2010lp (Taubenberger et al. 2013a). SN 2019yvq is the first relatively normal SN Ia with both an early flux excess and a peculiar nebular spectrum.

Notably, none of the "flux excess" SNe show evidence for hydrogen or helium emission indicative of swept-up material. SN 2018fhw had strong H emission at late times, but lacked an early flux excess one might expect from companion interaction (Vallely et al. 2019). SN 2015cp also had strong H emission at very late times (∼650–800 days after peak), but lacks any pre-peak data (Graham et al. 2019). Neither

SN 2015cp nor SN 2018fhw had any interaction signatures in their early spectra, unlike SNe Ia-CSM (Silverman et al. 2013a). Some SN Iax spectra have He emission lines consistent with swept-up material (Foley et al. 2009b, 2016a; Jacobson-Galán et al. 2019b), but none have yet had a clear early flux excess.

The most popular progenitor/explosion models for producing excess flux at early times (companion/circumstellar material interaction, surface ^{56}Ni mixing, double detonation, and violent mergers) have difficulty explaining the nebular spectra of SNe 2017cbv and 2018oh, two normal SNe Ia with well-observed early flux excess (Hosseinzadeh et al. 2017; Dimitriadis et al. 2019a; Shappee et al. 2019). In particular, neither SN had detectable [Ca II] emission, expected for double-detonation explosions (Polin et al. 2021). Additionally, SN 2018oh had early blue colors that were inconsistent with double-detonation models (Dimitriadis et al. 2019a). Other SNe Ia that feature early blue colors (but no obvious excess flux) such as SN 2009ig (Foley et al. 2012b), SN 2013dy (Zheng et al. 2013), and ASASSN-14lp (Shappee et al. 2016) also lack evidence of companion interaction or Ca emission in their nebular spectra (Pan et al. 2015a; Black et al. 2016; Maguire et al. 2018; Tucker et al. 2020).

In stark contrast to the other flux-excess SNe, the 7300 Å line complex of SN 2019yvq cannot be explained without strong [Ca II] emission, a signature of double-detonation explosions (and explicitly outlined by Miller et al. (2020) for SN 2019yvq). All observations of SN 2019yvq, and particularly the early-time flux excess and late-time [Ca II] emission, are consistent with a thick He shell double-detonation explosion of a sub-Chandrasekar-mass WD in a binary system.

The double-detonation mechanism requires mass transfer of He onto the primary WD. Several theoretical studies have indicated that little to no He on the surface of exploding low-mass WDs is needed to reproduce the photospheric properties of normal SNe Ia (Shen & Moore 2014; Townsley et al. 2019; Leung & Nomoto 2020). Double detonations with minimal He can be initiated dynamically via an explosion in the accretion stream (Guillochon et al. 2010), however, these systems are expected to strip He from the companion WD with masses of $\sim10^{-2}$ to 10^{-1} $M_{\odot}$ (Shen & Schwab 2017; Tanikawa et al. 2019), inconsistent with what is seen for SN 2019yvq. Alternatively, the He can ignite after a large enough He shell is developed (Shen & Moore 2014). Polin et al. (2019) showed that minimal-mass shells do not produce early flux excesses like that seen for SN 2019yvq, further excluding a dynamically driven detonation.

SNe 2016hnk and 2018byg are two similar-to-each-other, yet peculiar overall, SNe Ia that are likely the result of He-shell detonations on the surface of relatively low-mass WDs (De et al. 2019; Jacobson-Galán et al. 2020). Combined, they had early-time excess flux, strong nebular [Ca II] emission, and early spectra that demonstrated strong line blanketing from iron-group elements. Jacobson-Galán et al. (2020) modeled the light curves and spectra of SN 2016hnk, finding that the SN was likely the result of a 0.02 $M_{\odot}$ He-shell explosion on the surface of a 0.85 $M_{\odot}$ WD. De et al. (2019) estimated that SN 2018byg was produced by the detonation of a massive He shell (0.15 $M_{\odot}$) on a 0.75 $M_{\odot}$ WD. These SNe share many features with SN 2019yvq, but the lack of enhanced iron-group elements in the early spectra of SN 2019yvq (Miller et al. 2020) indicates that SN 2019yvq likely had a significantly larger WD mass than SNe 2016hnk or 2018byg (i.e., >0.85 $M_\odot$).

Polin et al. (2019) also provided evidence that double-detonation SNe originating with varying He-shell masses can be differentiated by their velocity and color. Given the high photospheric velocities, red optical colors, and qualitative similarity to the nebular model of a 1.1 $M_\odot$ WD with a 0.05 $M_\odot$ He shell (Figure 4.6), we argue that SN 2019yvq was in the distinct thick He shell subclass detailed in Polin et al. (2019). This may also provide evidence that a subset of early "flux-excess" SNe Ia are produced by progenitors with thick He shells. There may exist a continuum of thick He shell double-detonation progenitors that ranges from lower-mass events (<0.85 $M_\odot$) like SNe 2016hnk and 2018byg to higher-mass events (>1.1 $M_\odot$) like SN 2019yvq. Furthermore, given the likely [Ca II] presence in some fast-declining SNe Ia (e.g., SN 1999by; Blondin et al. 2018), it is reasonable to expect that they may be produced by a double-detonation progenitor. However, since these SNe do not show prominent early excess flux, they are likely not produced through the thick He shell channel.

Assuming that the progenitor system of SN 2019yvq is unique compared to the population of normal SNe Ia with nebular spectra, and SN 2019yvq is consistent with a thick He shell double-detonation explosion, we can estimate the fraction of normal SNe Ia that arise from this progenitor channel. The nebular spectrum of SN 2019yvq was acquired +153 days after peak brightness and SN 2019yvq had $M_g = -14.0 \pm 0.1$ mag at this time. Given a typical nebular spectroscopy survey limiting magnitude of 21.5 mag, the nebular phase spectrum of SN 2019yvq would have been detectable to 124 Mpc. The comprehensive nebular sample provided by Tucker et al. (2020) contains 94 normal

SNe Ia within this volume. Using Poisson statistics, we determine that the fraction of normal SNe Ia that are SN 2019yvq-like double-detonation SNe is $1.1^{+2.1}_{-1.1}\%$ (90th-percentile confidence range).

The simulations in Shen et al. (2018a) favor a ∼1.0 $M_\odot$ progenitor for typical SN 2011fe-like SNe Ia. Since SNe Ia typically do not show strong [Ca II] emission, they must either originate from a channel that does not have a double-detonation explosion or must come from WDs more massive than the progenitor of SN 2019yvq (i.e., >1.1 $M_\odot$). This presents a problem for minimal He mass double-detonation explosions as the dominant path to creating normal SNe Ia since >1.1 $M_\odot$ WDs are rare (Kilic et al. 2018). While the WDs may be born at a lower mass and accrete to a higher mass, reaching this higher mass can still be difficult, especially if the accretion is from a low-mass He WD. Furthermore, their synthetic spectra in the photospheric phase of massive WD explosions tend to generate higher velocities than observed in normal SNe Ia. Surviving WD companions of double-degenerate systems have been detected (Shen et al. 2018b), but it is still uncertain whether the implied rate of these progenitors can account for the majority of SNe Ia.

Shen et al. (2018b) used *Gaia* parallaxes and proper motions to search for hyper-velocity stars that could be the surviving companion star from a double-detonation progenitor system. They estimated that if all SNe in the Milky Way originated from the dynamically driven double-degenerate double-detonation (D^6) channel, they would detect 22 runaway WDs within 1 kpc of the Sun in the *Gaia* DR2 sample. Shen et al. (2018b) found three likely runaway WDs, however, these ranged from a distance of 1.0

to 2.3 kpc from the Sun and were only detectable because of their higher luminosity than normal WDs. This was an incredible success of the theory, but the detection rate, when considering the higher luminosity, is consistent with only 1.1% of SNe Ia producing runaway WDs. Assuming Poisson statistics, we determine that 95% confidence interval of the observed-to-predicted rate is $0.35 - 3.0\%$. While there are several selection effects that we ignore for both measurements, we note that the rate of SN 2019yvq-like events is consistent with the rate of hyper-velocity white dwarfs in the Milky Way. Since the rates are similar, it is possible that all double-detonation explosions (those with stable and unstable mass transfer) account for only a fraction of normal SNe Ia, with an additional channel possibly necessary to produce the bulk of normal SNe Ia.

The diversity of SNe Ia in the nebular phase, and particularly the tell-tale signs of different progenitor/explosion scenarios for SNe 2010lp, 2018fhw, and 2019yvq, point to a variety of paths to have SNe Ia with similar near-peak observables. These SNe provide some of the strongest support for violent-merger, single-degenerate, and double-detonation models, respectively. Yet the rarity of these kinds of SNe and the divergence from the majority of SNe Ia suggests that these channels are either not the dominant channels producing most SNe Ia, or these examples are extrema of the most-common channel.

While some of these rare SNe Ia would likely be excluded from cosmological samples, SN 2019yvq is not clearly an outlier. Although its decline rate is faster than the average SN Ia (Miller et al. 2020), it is not large enough to be clearly rejected, especially for lower signal-to-noise ratio or more sparsely covered light curves. Additionally, its red color and low peak luminosity are consistent with its decline rate. Future detailed simulations will reveal if SN 2019yvq-like SNe impact cosmological measurements.

We summarize our analysis of the SN 2019yvq nebular spectrum below:

- The +153-day nebular spectrum of SN 2019yvq exhibits strong [Ca II] $\lambda\lambda$7291, 7324 and Ca NIR triplet emission features. The nebular spectra of some other fast-declining SNe Ia likely have contributions from [Ca II] $\lambda\lambda$7291, 7324 emission, but the relative strengths of the [Ca II] to [Fe II] and [Ni II] in these SNe are more difficult to determine. In some more extreme SNe Ia such as SN 1999by, [Ca II] likely dominates in this region, but the narrow Fe and Co features in other region of the spectra are inconsistent with SN 2019yvq.
- We fit a multiple-component Gaussian emission model to the 7300 Å line complex consisting of [Fe II], [Ni II], and [Ca II] emission, finding that all components are blueshifted relative to their rest-frame wavelengths. Blueshifted nebular lines are atypical for high-velocity SNe Ia such as SN 2019yvq.
- We find no evidence for swept-up material in the nebular spectrum of SN 2019yvq. Our limits on the amount of hydrogen and helium mass are $<2.8 \times 10^{-4}$ and 2.4×10^{-4} $M_\odot$, respectively.
- We also do not detect [O I] $\lambda\lambda$6300, 6364 emission, an expected feature if there is significant unburned material in the ejecta.
- A comparison to the double-detonation models from Polin et al. (2021) reveals that SN 2019yvq was likely the result of double-detonation explosion. The strength of

the Ca emission indicates a larger progenitor mass (1.15 $M_\odot$), however, a lower progenitor mass still better reproduces the early light-curve and low peak luminosity.

- The rarity of SN 2019yvq-like events suggests that thick He shell double-detonations make up $1.1^{+2.1}_{-1.1}\%$ of the normal SN Ia population.

Continued observations of SN 2019yvq will further enhance this picture with future observations potentially revealing additional insight into the progenitor system and explosion. Continued monitoring of the [Ca II] emission will allow models to better separate abundance, ionization, and asymmetry. Additional data such as spectropolarimetry of similar events will be especially valuable to untangle the early-time emission.

More photometric observations of SNe Ia in their infancy are needed to better understand the population with early excess flux. Several subclasses of SNe Ia have both early excess flux and spectral signatures in the nebular phase that indicate a variety of progenitor channels (Taubenberger et al. 2013a; Cao et al. 2015; Kromer et al. 2016; De et al. 2019; Jacobson-Galan et al. 2019a). More typical SNe Ia with early excess flux lack clear late-time signatures (Hosseinzadeh et al. 2017; Sand et al. 2018; Dimitriadis et al. 2019a,b; Shappee et al. 2019; Tucker et al. 2019). And some SNe Ia with peculiar nebular spectra (Taubenberger et al. 2013b; Kollmeier et al. 2019) do not have detected early-time excess flux, often to deep limits. High-cadence surveys of the local volume where one can hope to obtain a nebular spectrum will be critical.

Chapter 5

The Foundation/Swope SN Ia Host Galaxy Sample: The Definitive Measurement of How Environment Influences SN Ia Distance Measurements

5.1 Introduction

Type Ia Supernovae (SNe Ia) provide a remarkable avenue for investigating the expansion history of the Universe. Through relationships of their peak luminosity with light-curve shape and color, SNe Ia are standardizable candles (Pskovskii 1977; Phillips

1993; Riess et al. 1996). These methods were used prove the accelerating expansion of the Universe (Riess et al. 1998; Perlmutter et al. 1999). Modern cosmological analyses use thousands of spectroscopically confirmed SNe Ia to measure cosmological parameters like the expansion rate of the Universe (H_0), and the equation of state parameter (w) to within precision of a few percent (Riess et al. 2021; Scolnic et al. 2021).

As sample sizes have increased, it has become clear that photometric uncertainty cannot account solely for the observed scatter in SN Ia distance measurements. Hubble residuals (HRs) are the differences between the measured distance moduli and distance moduli inferred from a cosmological model. The *intrinsic* scatter of HR measurements is potentially related to properties of the progenitor environment or explosion physics (Conley et al. 2011; Scolnic et al. 2018).

Hamuy et al. (1996) showed that SN Ia luminosities depend on host galaxy morphology. In particular, bright slow declining SNe Ia are more likely to occur in late type galaxies, and faint fast declining SNe Ia are more likely to occur in early type galaxies. Similar trends have also been observed with host galaxy mass, and/or metallicity (Hamuy et al. 2000; Gallagher et al. 2005). While these effects are accounted for in the standardization of SN Ia luminosities, they are still indicative of physical differences in SN Ia populations that correlate with environment. However, several studies have shown that even after standardization SN Ia corrected luminosities still correlate with host galaxy properties like mass, star-formation rate (SFR), and metallicity (Kelly et al. 2010; Sullivan et al. 2010; Lampeitl et al. 2010; Gallagher et al. 2008; D'Andrea et al. 2011; Childress et al. 2013c; Pan et al. 2014).

Current cosmological analyses include a correction to SN luminosities based on the relationship between HR and host galaxy mass, yet we still do not know the physical origin or functional form of this relationship. Host galaxy mass must be a proxy for an underlying cause such as progenitor metallicity or age (Childress et al. 2014; Graur et al. 2015). The UV spectra of SNe Ia are likely a more direct probe of progenitor metallicity (Höflich et al. 1998; Lentz et al. 2000; Foley et al. 2008c). Foley & Kirshner (2013b) showed that SNe Ia with different metallicities (measured from the UV continuum) have different peak luminosities without affecting light-curve shape. Pan et al. (2020) analyzed a larger sample of UV spectra and found that SN Ia progenitor metallicities are correlated with HR. Additionally, Siebert et al. (2020a) observed a correlation of HR with SN Ia ejecta velocity, further indicating that progenitor explosion physics may be a source of HR intrinsic scatter.

It is still not clear whether host galaxy mass is the best parameterization of the relationship between HR and environment, or if another property such as specific SFR (sSFR), or gas-phase metallicity would be better suited. Furthermore, a detailed understanding of how SN environments evolve with redshift is critical for understanding potential distance biases induced by these SN Ia luminosity corrections.

Low-z samples of SNe Ia are an ideal testing ground for understanding environmental dependencies of SN Ia luminosities. SNe Ia explode in a large diversity of host environments and, in many cases, one can directly study the local SN environment. Several studies have looked for evidence of HR relationships with local SFR, sSFR, and color. Notably, Rigault et al. (2013) found evidence for a HR step with local SFR, Rigault et al. (2018) found strong evidence for a local sSFR step, Roman et al. (2018) found evidence for a local $U - V$ color step, and Jones et al. (2018b) found evidence for local $u - g$ color and local mass steps. Briday et al. (2022) showed that the accuracy of an environmental property tracer depends on its ability to distinguish between two populations. They found that local sSFR is the most accurate tracer indicating that that progenitor age may be responsible for the environmental correlations with HR. Galbany et al. (2016) measured local metallicities for a sample 58 SN Ia host galaxies and found that local metallicities were on average slightly smaller than global metallicities. So far, no effort has been made to measure a HR step using local metallicities.

In this work we aim to characterize both global and local host galaxy environments of SNe in the low-z Foundation Survey (Foley et al. 2018) and Swope Supernova Survey (Rojas-Bravo et al. in prep). In Section 5.2, we describe the demographics of the SN and host galaxy samples, we describe our spectroscopic data reduction techniques, and outline our process for measuring host galaxy environmental properties from optical spectra. In Section 5.3, we compare the properties of our spectroscopic host galaxy sample to those of field galaxies and those of the SN host galaxies from P14. We also characterize the global and local relationships of each environmental tracer with HR. We summarize our findings and their relevance to next-generation cosmological surveys in Section 5.4. Throughout this paper, we assume $H_0 = 70$ km s^{-1} Mpc^{-1} and a flat universe with $\Omega_M = 0.3$.

5.2 Methods

5.2.1 Host Galaxy Sample

In this analysis, we combine photometric and spectroscopic observations of 517 total SNe Ia from the Foundation survey (Foley et al. 2018) and the Swope supernova survey (Rojas-Bravo et al. in prep). These surveys contribute 327 and 189 total SNe, respectively. The Foundation survey used the Pan-STARRS1 (PS1) telescope to obtain light-curves of low-z SNe Ia. Foundation SNe were observed on the well-calibrated PS1 system and have thus been used to reliably measure distances. Observations using the Swope natural system have been placed on the same photometric system as PS1 using Supercal transformations (Scolnic et al. 2015).

86% (N=443) of our combined SN sample overlaps with the PS1 footprint. In Figure 5.1, we present the redshift, apparent brightness and absolute brightness distributions of the host galaxies in the Foundation and Swope samples. Apparent and absolute brightnesses have been estimated from integrated photometry on Kron radius (Kron 1980) sized apertures using PS1 images. The Foundation and Swope SN samples both have median redshifts of 0.033 and the total SN sample redshift range is $0.003 < z < 0.15$. The Foundation and Swope luminosity distributions show no significant differences.

Using PS1 gi-band photometry and Equation 8 from Taylor et al. (2011), we estimate the global masses of 419 galaxies from the Foundation/Swope combined sample. The mass distributions of the Foundation and Swope samples are shown in Figure 5.2. A K-S gives a 58% probability that Foundation and Swope host galaxy samples are

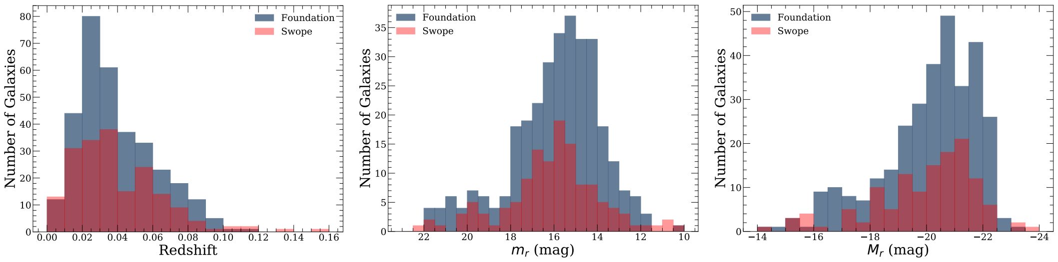

Figure 5.1: From left to right: The distributions of redshift, apparent r-band brightness (m_r), and absolute r-band brightness (M_r) for the Foundation (blue) and Swope (red) host galaxy samples.

drawn from the same stellar mass distribution.

5.2.2 Spectroscopic Sample

In total we have obtained optical spectroscopy of 372 host galaxies in the Foundation/Swope combined SN sample (72% of the full SN sample). With the available PS1 photometry, we have estimated masses for 322 host galaxies in our spectroscopic sample and compare to that of the sample from P14 in Figure 5.3. Our spectroscopic sample is 4.5 times larger than P14 and has a slightly lower median stellar mass of $\log(M_*/M_\odot) = 10.0$ (10.4 for P14). We also find that 10% of our spectroscopic observations come from galaxies with $\log(M_*/M_\odot) < 8.5$ (4% in P14). In both our total and spectroscopic samples we see a slight preference for lower mass galaxies in comparison to P14. This is more evident in the right panel of 5.3 which shows the cumulative distribution functions (CDFs) of these measurements. K-S tests yield 2.2% and 0.28% probabilities that our total and spectroscopic host galaxy samples are drawn from the same population as P14, respectively. The increased preference for lower mass galaxies in our spectroscopic sample may be related to our desire to probe environmental effects in the most extreme

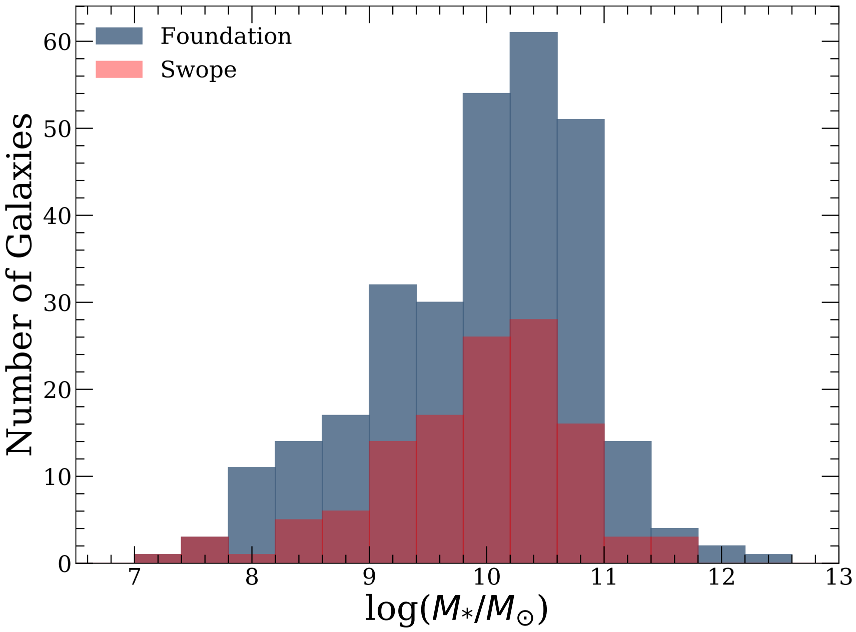

Figure 5.2: Host galaxy mass distributions measured from PS1 gi-band photometry for our Foundation (blue) and Swope (red) host galaxy samples.

environments. However, we caution that these mass distributions have been derived using different methods.

5.2.3 Observations & Data Reduction

Our host-galaxy observations were obtained using optical spectrographs on five different telescopes (Table 5.1). Targets were observed in longslit mode with the slit oriented to align with both the host galaxy nucleus and SN position. To minimize slit losses, observations were taken either using an ADC, at low airmass (≤ 1.1), or by timing the observation such that the position angle was within 10 degrees of the parallactic angle.

A breakdown of the fraction of the observations using each instrument is shown

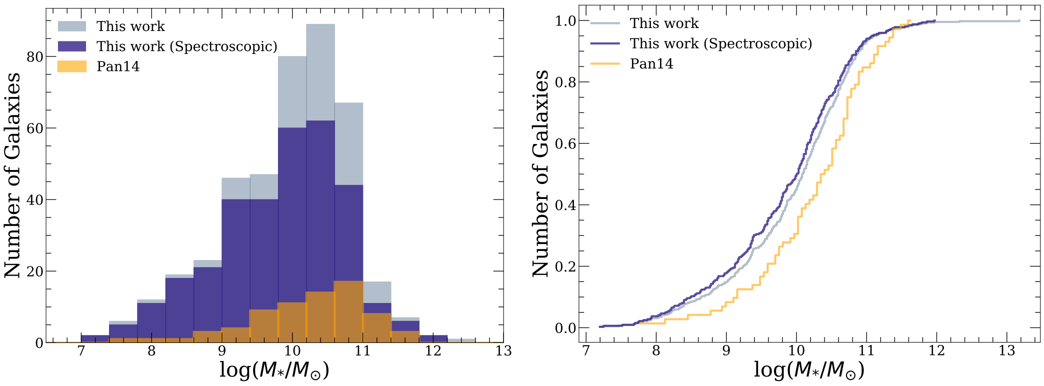

Figure 5.3: (*left panel*): Host galaxy mass distributions of our combined Foundation/Swope sample (blue), our spectroscopic sample (purple), and the sample from P14. (*right panel*): CDFs of these stellar mass measurements.

Table 5.1: The instrumental setups used for the combined Foundation/Swope spectroscopic sample.

Telescope	Spectrograph	Gratings/Grisms		λ coverage	# of Galaxies
		(Red)	(Blue)	(Å)	
Lick	Kast	300/7500	452/3306	3000–11000	177
Keck	LRIS	400/8500	600/4000	3200–10000	119
SOAR	Goodman	400 m2	400 m1	3700–9000	41
Mayall	KOSMOS	Red VPH	Blue VPH	3600–9600	28
Gemini	GMOS	R400	B600	3600–9400	7

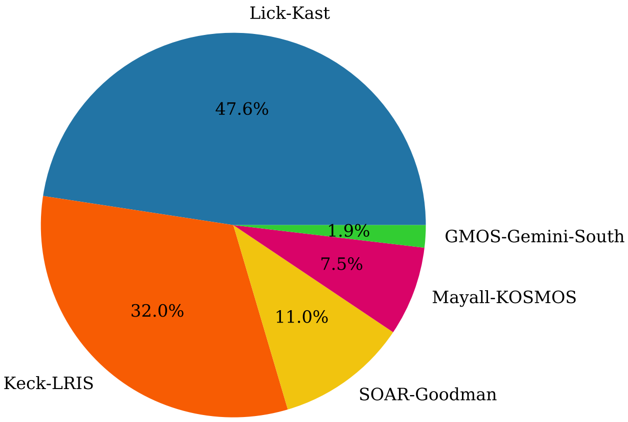

Figure 5.4: Contributions of each telescope/spectrograph to the Foundation/Swope combined sample. Lick and Keck contribute the largest number of spectra to the sample.

in Figure 5.4. In total we have acquired 177, 119, 41, 28, and 7 follow-up host galaxy spectra from Lick, Keck, SOAR, Mayall, and Gemini, respectively. The two largest contributors are Kast and LRIS comprising 47.6% and 32% of our host-galaxy sample, respectively. LRIS was critical for obtaining redshifts and properties of 86% of all targets with r > 18.5 mag. GMOS was used to obtain spectra of the faintest Swope survey host galaxies in the southern hemisphere.

All data were reduced using standard IRAF[8] and python routines for overscan corrections, flat fielding, flux calibration and telluric lines removal, using spectrophotometric standard star spectra, obtained the same night (Silverman et al. 2012b). For each galaxy, we have performed a total of 9 extractions with different aperture sizes and locations. We center four of the apertures on the host galaxy nucleus and four apertures on the SN position with physical sizes of 1 kpc, 1.5 kpc, 2 kpc, and 3 kpc.

---

[8] IRAF is distributed by the National Optical Astronomy Observatory, which is operated by the Association of Universities for Research in Astronomy (AURA) under a cooperative agreement with the National Science Foundation.

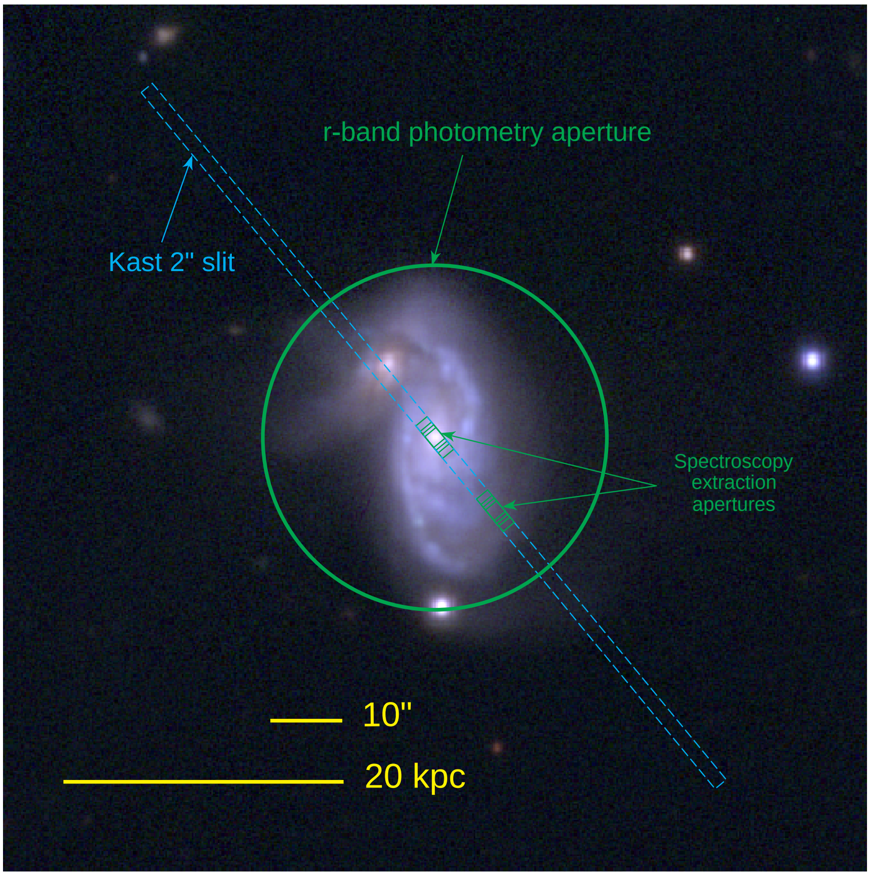

Figure 5.5: PS1 *gri*-band color composite of the host galaxy of SN 2017mf (NGC5541). The blue-dashed rectangle represents the Lick-Kast 2" wide slit projected on the sky. The green rectangles represent our 1, 1.5, 2, and 3 kpc extraction apertures centered on the galaxy nucleus and SN location. The green circle is the aperture from which we derive our galaxy photometry. We also extract host galaxy spectroscopy using a rectangular aperture with length corresponding to the diameter of the green circle.

The final aperture is defined by the PS1 r-band Kron radius and centered on the galaxy nucleus. Reductions using apertures whose widths were smaller than the seeing on a given night are not used in the final analysis.

To illustrate our observing and data reduction strategy, in Figure 5.5, we show a PS1 gri-band color composite of the host galaxy of SN 2017mf (NGC 5541) with various spectroscopic and photometric apertures overlaid. This galaxy was observed with KAST with the 2” slit (blue-dashed rectangle) oriented to include the SN location. Green rectangles represent the extraction apertures described above, and the green circle is the aperture from which we derive our photometry.

5.2.4 Host galaxy property determination

In this section we describe our process for measuring both the global and local spectroscopic properties of our sample. Accurate emission line flux measurement require careful treatment of stellar absorption, therefore, we first describe the techniques used for stellar population fitting. We then detail our method for measuring emission line fluxes that allow us to determine star formation rates (SFRs) and a variety of gas-phase metallicity calibrators.

Stellar population properties

In order to properly account for stellar absorption in emission line flux measurements we fit stellar population models to each of our host galaxy spectra. We use the code `FIREFLY`[9] (Wilkinson et al. 2017), a χ^2-squared minimization spectral fitting

---

[9] https://github.com/FireflySpectra/firefly_release

code for the purposes of deriving properties of stellar systems. The fitting routine first removes the low-order continuum shape and uses this to estimate the interstellar attenuation curve (and subsequent best-fit E($B-V$)). Thus, higher frequency modes are used to estimate stellar ages and metallicities. FIREFLY implements the single stellar population (SSP) models from Maraston & Strömbäck (2011) and iteratively adds SSPs with different ages and metallicities until there is little improvement in χ^2. To limit systematic biases associated with the presence of strong emission lines, we mask the mask emission lines before fitting. Our host galaxy spectra are also corrected for Milky Way extinction prior to fitting a stellar population. In Figure 5.6, we show an example fit to the stellar continuum of the host galaxy of SN 2017gfl (GALEXASC J215518.30-261846.9). The blue curve is our original spectrum, the magenta curve is the FIREFLY model of the stellar component, and the black curve is the difference where we have removed larger scale differences with a 200 pixel median filter, as in (Tremonti et al. 2004). We derive several spectroscopic environmental properties from emission lines in "gas-only" best fitting spectra like this.

Prior to fitting, reductions are scaled such that the r-band magnitude matches that measured from the PS1 kron-radius aperture. This is primarily important for the later estimation of stellar properties from kron-radius aperture spectroscopic reductions. Using this method we produce gas-only best fitting spectra for all 9 reductions of each galaxy.

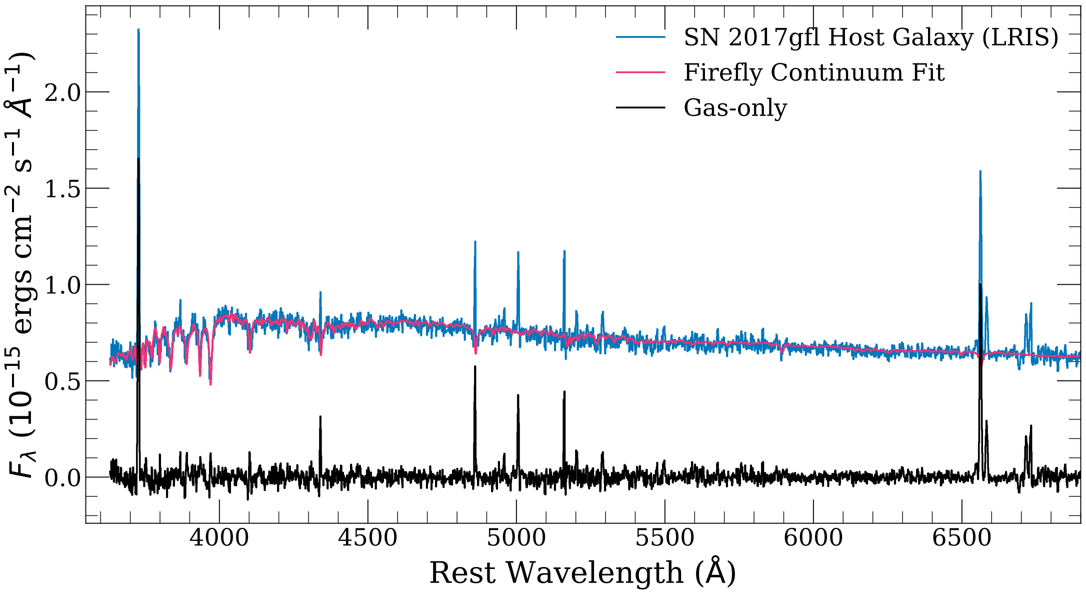

Figure 5.6: Example stellar continuum fit to Keck-LRIS spectrosocopy of the host galaxy of SN 2017gfl using FIREFLY (Wilkinson et al. 2017). The blue curve is the data, the magenta is the stellar continuum fit, and the black is our "gas-only" spectrum, the difference between the data and the fit where additional residuals have been removed using a 200 pixel median filter.

Estimation of emission line fluxes

Following a similar procedure to Tremonti et al. (2004), we simultaneously fit Gaussian profiles to a sample of emission lines necessary for several metallicity calibrators ([O II] $\lambda\lambda3726, 3729$, [O III] $\lambda\lambda4959, 5007$, $H\beta$, $H\alpha$, [N II] $\lambda\lambda6548, 6584$, and [S II] $\lambda\lambda6717, 6731$). We require that lines from the same atomic species have the same velocity and width. This allows use to lower the number of free parameters, and use the properties of stronger lines to constrain weaker lines. First, the gas-only spectrum is normalized to the strongest emission line. An initial χ^2-minimization fit is performed with loose priors to ensure that line amplitude and width are non-negative. The results of this fit then serve as input to a simple Markov Chain Monte Carlo algorithm using the python package `emcee`[10] (Foreman-Mackey et al. 2013). Walkers are initialized in Gaussian distributions centered on the result from the initial fit with widths of the flux uncertainty, 5 km s^{-1}, and 20 km s^{-1}, for amplitude, velocity, and velocity width, respectively. For each fit we use 50 walkers run for 100 iterations.

Figure 5.7 shows zoom in on our Gaussian fits to the[O II] $\lambda3727$ (purple), [O III] $\lambda\lambda4959, 5007$ (pink), $H\beta$, $H\alpha$ (blue), [N II] $\lambda\lambda6548, 6584$ (yellow), and [S II] $\lambda\lambda6717, 6731$ (green) emission lines from the gas-only spectrum in Figure 5.6. The thin dashed lines represent random realizations from the posterior distributions of the Gaussian parameters. We use the full posterior distribution to estimate both the the fluxes and uncertainties of each emission line. In Figure 5.8, we show the relationship between the O II and $H\alpha$ line fluxes derived using this fitting method. We do not see

---

[10] https://github.com/dfm/emcee

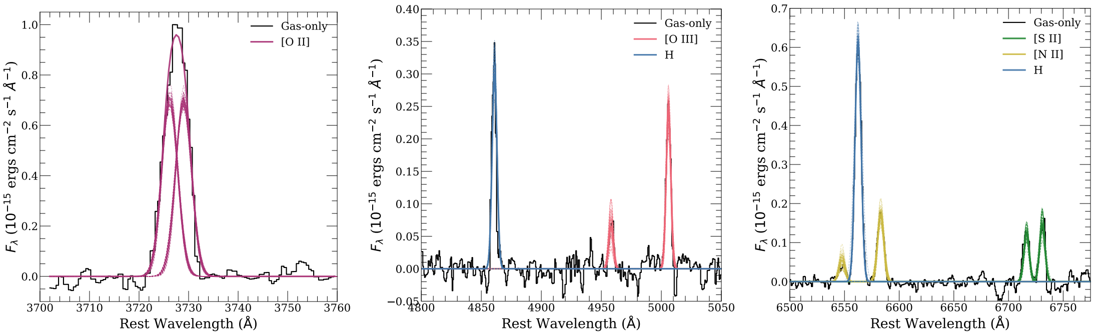

Figure 5.7: Example Gaussian fits to emission lines in our gas-only spectrum (black) from Figure 5.6. The purple, blue, pink, yellow, and green curves correspond to best-fit Gaussian profiles of lines from [O II], H, [O III], [N II], and [S II], respectively. The dashed curves represent 100 random realizations from the MCMC posterior distribution.

evidence for significant biases with flux. Furthermore, we observe a RMS scatter of 0.30 dex.

Star formation rate

We characterize the SFR of a host galaxy via its $H\alpha$ emission strength. Using our r-band kron-radius aperture reduction that has been scaled to the PS1 r-band flux, we determine the luminosity of $H\alpha$, L($H\alpha$). We adopt the conversion of Kennicutt (1998) to relate L($H\alpha$) to the SFR.

$$SFR = 7.9 \times 10^{-42} \times L(H\alpha) M_{\odot} yr^{-1} \tag{5.1}$$

This relation assumes case B recombination and a Salpeter (1955) initial mass function (IMF). Based on Brinchmann et al. (2004), we assume a systematic uncertainty of 0.2 in log(SFR). Kewley et al. (2005) found that selecting samples with covering fractions that capture $>$ 20% of the galaxy light is necessary to avoid systematic uncertainties

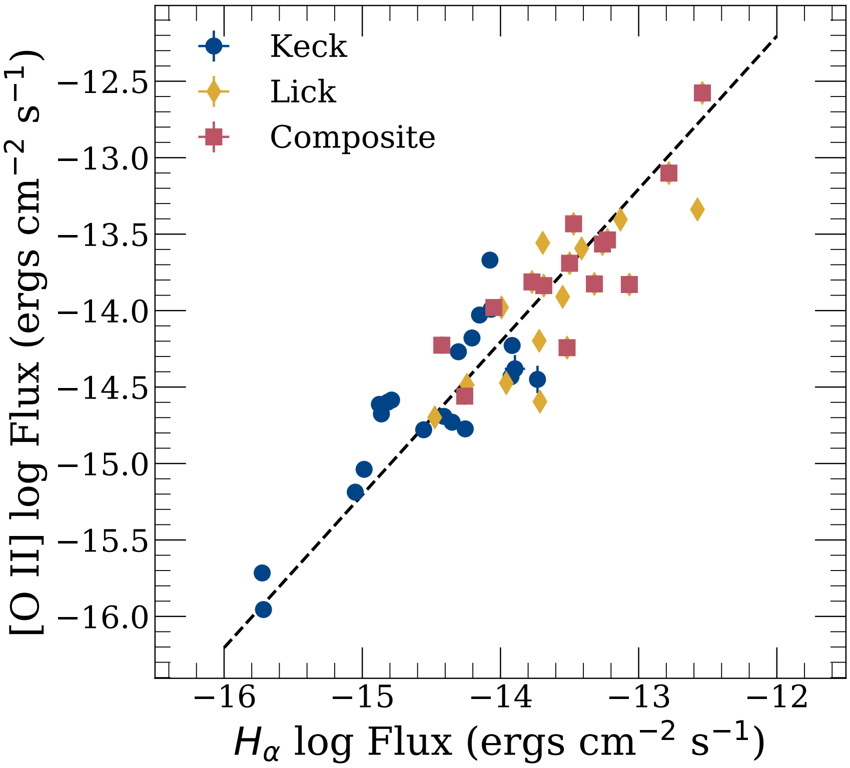

Figure 5.8: Comparison of fitted [O II] and $H\alpha$ emission line fluxes. Blue circles are measurements made from Keck-LRIS spectroscopy, gold diamonds are measurements made from Lick-Kast spectroscopy, and red squares are measurements from the composite galaxies identified in Figure 5.10. The dashed line is the 1:1 relation offset by the mean difference in flux.

from aperture effects. These biases are strongest for closest and most massive galaxies. In the left and center panels of Figure 5.9, we show our measurements of SFR and sSFR in comparison to those measured from Sloan Digital Sky Survey (SDSS) fiber spectroscopy (Tremonti et al. 2004). Our measurements were derived from longslit spectroscopy using a rectangular aperture with a size of the r-band Kron radius (see Figure 5.5). The mean differences in log(SFR) and log(sSFR) are -0.09 ± 0.08 and -0.02 ± 0.06 dex, respectively. This is reassuring that despite differences from SDSS in aperture size and orientation, we do not see significant differences in host galaxy properties that are derived from $H\alpha$ luminosities.

Gas-phase metallicity

There are numerous different prescriptions for calibrating gas-phase metallicities measured from emission line ratios. Once can directly determine the electron temperature (T_e) metallicity from the auroral [O III] λ4363 line, but this line is very weak. For the Foundation/Swope combined host galaxy sample, we opt to use indirect methods following the work of Kewley & Ellison (2008) (KE08). KE08 determined that the absolute metallicity scale varies up to 0.7 dex in 12+log(O/H) and created conversions among these different calibrations that remove this discrepancy. While absolute metallicity varies among methods, the relative differences are often consistent. Thus, all metallicity measurements and comparisons in this work are done using common calibrators.

To quantify each of these different diagnostics, we implement the code `pyMCZ`[11]

---

[11] https://github.com/nyusngroup/pyMCZ

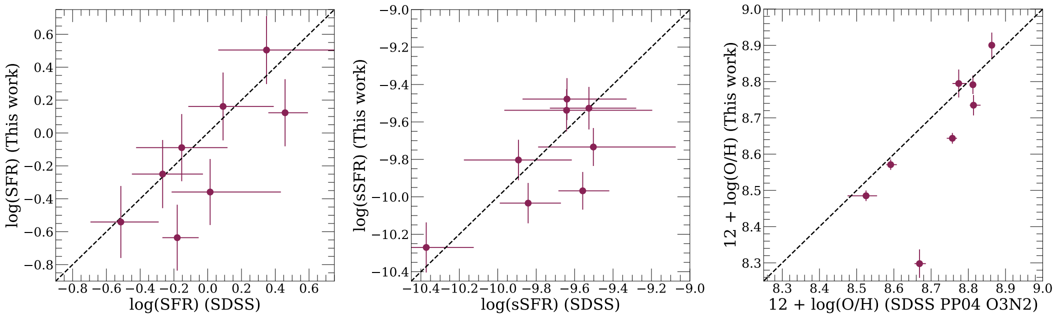

Figure 5.9: Comparisons of our SFR, sSFR, and gas-phase metallicity (left, center, right) measurements to those from SDSS spectra of the same galaxies (Tremonti et al. 2004). The dashed-lines show the 1:1 relation in each panel. For metallicity, we have converted values derived from Tremonti et al. (2004) to the PP04 O3N2 calibrator using the appropriate formula from KE08.

(Bianco et al. 2016). This code takes our emission line fluxes and uncertainties as input, uses the Balmer decrement to estimate E($B-V$) and correct for interstellar reddening, and outputs a variety of strong line diagnostics used to estimate oxygen abundance. Uncertainties are estimated via a Monte Carlo method. In this work we primarily focus on the Pettini & Pagel (2004) (PP04) calibrators PP04 N2 and PP04 O3N2 based on the [N II]/Hα and [O III]/$H\beta$ / [N II]/$H\alpha$ line ratios, respectively. These calibrators are most commonly used in analyses of SN and GRB environments (Modjaz et al. 2011; Childress et al. 2013b; Pan et al. 2014; Galbany et al. 2016), and benefit from using lines that are close in wavelength and less susceptible to uncertain reddening and scaling between blue and red CCDs.

In the right panel of Figure 5.9, we compare a subset of our PP04 O3N2 gas-phase metallicity measurements to those measured by Tremonti et al. (2004). We have converted the metallcities of Tremonti et al. (2004) to the PP04 O3N2 calibrator so that the measurements can be directly compared. Similar to our $H\alpha$-derived galaxy properties, we do not see any evidence for a significant difference between our measurements and SDSS (mean offset $= 0.07 \pm 0.04$ dex).

AGN Contamination

In some of our spectroscopic sample, non-thermal emission from active galactic nuclei (AGN) can dominate over emission from hot stars. This effect can cause measure emission line ratios to not accurately reflect the gas-phase metallicity. To identify and remove AGN from our host sample, we use a BPT diagram (Baldwin et al. 1981). In Figure 5.10, we show the relationship between [N II]/Hα and [O III]/Hβ for our host galaxy sample. The two black curves are the criteria proposed by Kewley et al. (2001) and Kauffmann et al. (2003) for identifying AGN. We define galaxies lying to the right of the Kewley et al. (2001) curve as potential AGN, and galaxies in the region where the two criteria disagree as “composite” (as in Brinchmann et al. 2004).

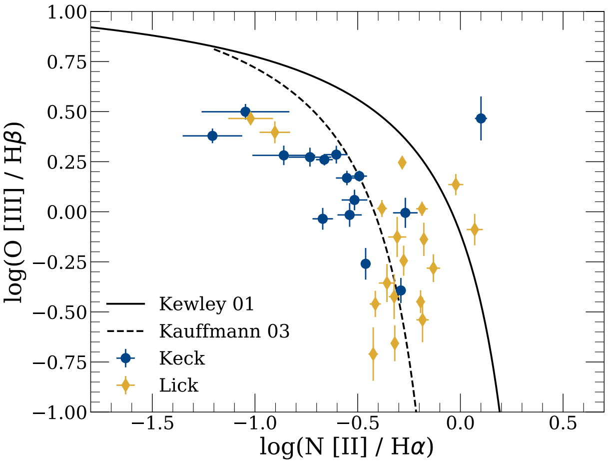

Figure 5.10: The BPT diagram that we use to classify AGN host galaxies in our sample. Blue circles are measurements made from Keck-LRIS spectroscopy and gold diamonds are measurements made from Lick-Kast spectroscopy. We over-plot the Kewley et al. (2001) (solid curve) and Kauffmann et al. (2003) (dashed curve) criteria. We identify galaxies located between the two criteria as "composite" galaxies, and galaxies to the right of Kewley 01 as AGN. Lick observations contribute most of the composite galaxies and AGN in our sample.

5.3 Results and Discussion

Here we examine the global and local environmental properties of the preliminary Foundation/Swope spectroscopic host galaxy sample. We first compare the mass-SFR and mass-metallicity relations measured from our sample to those of field galaxies drawn from SDSS and those derived measured from another SN host galaxy sample (P14). We then use these measurements to assess the impact of host galaxy environment on SN distance measurements. We derive HR step measurements as a function of global and local metallicity, and global sSFR.

5.3.1 The Mass-SFR relationship

In Figure 5.11 we display a comparison of the SFRs of our host galaxies derived from Hα to the relationship from the Galaxy And Mass Assembly survey (GAMA; Foster et al. 2012, red line), and the measurements from P14 (black points). Similar to P14, our data show lower star formation in galaxies with $\log(M_*/M_\odot) > 10$ relative to the results from GAMA. We note that 50% of our galaxies that in this mass range are classified as "composite" as outlined in section 5.2.4. We also find that SN host galaxies at the low-mass end of this relationship tend to have higher star formation than GAMA. Combining with P14, there are 8 total galaxies with ($\log(M_*/M_\odot) < 8.5$) that lie above the GAMA relation. Further quantitative assessment of these results is complicated by the potential for aperture effects stemming from the limitations of longslit spectroscopy. Some light of the host is lost due to the fixed slit width of each spectrograph. In future analyses, careful aperture corrections should be made to account for this effect. The full Foundation/Swope sample will provide important constraints low mass end of the mass-SFR relationship for SN Ia host galaxies.

5.3.2 The Mass-Metallicity relationship

In Figure 5.12, we show mass-metallicity relations using two different calibrators, PP04 N2 (left) and PP04 O3N2 (right). The solid red curves represent the respective mass-metallicity relationships derived for field galaxies in KE08 and the dashed curves represent the rms uncertainty. In the left panel, measurements have been obtained in the same manner as in P14. In the right panel, the measurements from P14

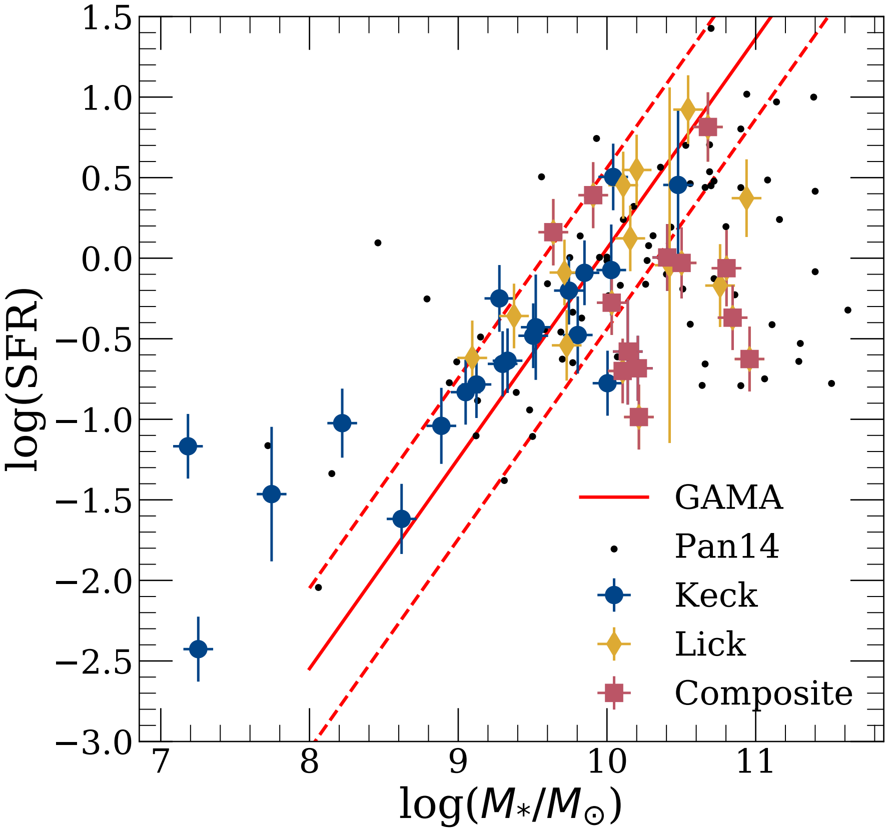

Figure 5.11: The SFR measured from Hα as a function of host galaxy stellar mass measured from PS1 photometry. Blue circles are measurements made from Keck-LRIS spectroscopy, gold diamonds are measurements made from Lick-Kast spectroscopy, and red squares are measurements from the composite galaxies identified in Figure 5.10. We compare to the relation derived by the Galaxy and MASS Assembly survey (GAMA; Foster et al. 2012, red curve), and the data from P14 (black points). Similar to P14, we find that SN host galaxies at the higher mass end of this relationship tend to have lower SFRs.

have been recalibrated using the metallicity conversion formula derived in KE08. In both cases, it is clear that our mass-metallicity relationship is consistent with both KE08 and P14. This is also in agreement with Childress et al. (2013b) who find a similar mass-metallicity relationship to that of SDSS DR7 field galaxies. In the valid KE08 mass range we observe a slightly smaller rms scatter of 0.13 dex using the PP04 O3N2 method (0.14 dex for PP04 N2) and mean offset of 0.07 ± 0.02 dex (0.08 ± 0.02 dex for PP04 N2), consistent with the KE08 relation. KE08 found that in the relationships between metallicity calibrators, the KK04, M91, PP04 O3N2, and KD02 methods had the smallest residual scatter, and were therefore the most reliable base calibrations. Given the lower rms scatter in our PP04 O3N2 mass-metallicity relationship, we choose this as our primary metallicity indicator in later sections and analysis.

We find that there is good agreement of the Foundation/Swope mass-metallicity relationship with the fiducial normal mass-metallicity relationship measured by KE08. This supports the results of other SN Ia host galaxy population studies (Childress et al. 2013b; Pan et al. 2014) and indicates that SN Ia on average do not prefer low- or high-metallicity environments.

5.3.3 Global and Local Metallicities

Significant differences in the global vs. local properties of SN Ia host galaxies could be troubling for cosmology. Host galaxies of high-z SNe Ia are faint and have smaller angular diameters, making detailed characterization of their local SN environments very difficult. By studying low-z analogues of these galaxies, we can begin to understand how this loss of information potentially affects our cosmology.

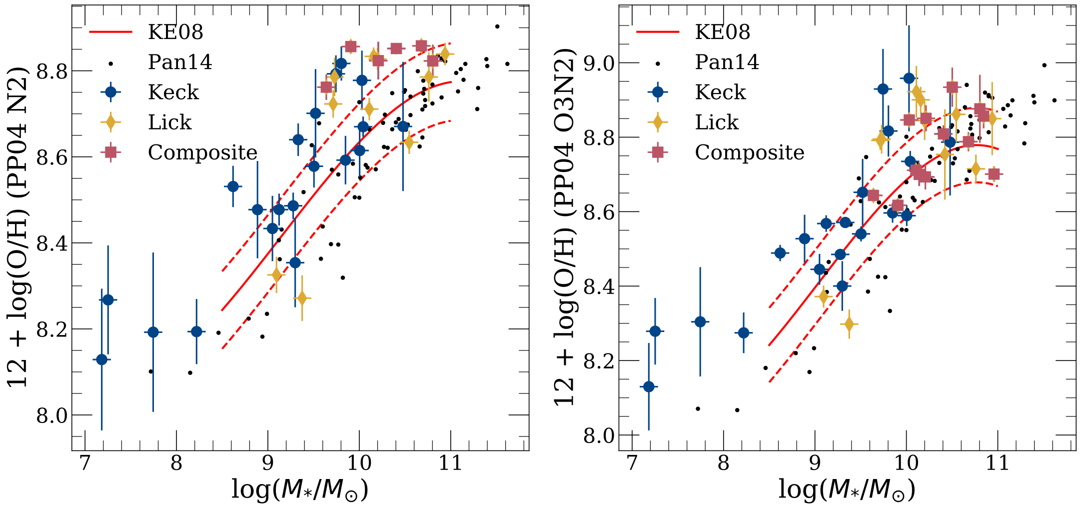

Figure 5.12: Mass-metallicity relationships derived from our host galaxy sample using the PP04 N2 (left panel) and PP04 O3N2 calibrators (right panel). Blue circles are measurements made from Keck-LRIS spectroscopy, gold diamonds are measurements made from Lick-Kast spectroscopy, and red squares are measurements from the composite galaxies. The red curves show the best-fit mass-metallicity relationships for each calibrator from KE08. The black points correspond to measurements from P14. In the right panel, measurements from P14 have been converted from PP04 N2 to PP04 O3N2 using the formula from KE08.

In the left panel of Figure 5.13, we show the difference between the local and global metallicities as a function of SN physical offset from its host galaxy. The local metallicity is measured from a 1 kpc aperture and the global metallicity is measured from an aperture with size of the galaxy r-band Kron radius. Circle are measurements made from Keck-LRIS spectra and diamonds are measurements made from Lick-Kast spectra. Points are colored by the ratio of the SN physical offset to the spatial resolution. The colorbar is truncated at SN Offset/Resolution = 4 to better illustrate the less-resolved metallicity differences, so dark points can have significantly larger values. Ground based observations are typically limited by the seeing of the atmosphere, thus we estimate our spatial resolution by calculating the physical sizes of typical nightly seeing at Keck and Lick Observatory (1" and 2" respectively) at the redshift of each SN. These are represented by the x-axis errorbars. The right panel of Figure 5.13, is the same as the left but for the differences between the local and nuclear metallicities, where nuclear metallicities have been measured from a 1 kpc aperture.

Overall we do not see strong evidence for differences between the local metallicity and global or nuclear metallicities. This is in agreement with Sanders et al. (2012) who found that central and local metallicites of SN Ibc SN sites are equal within 0.1 dex (using the PP04 indicator). This work also found that blending from from spatial resolution worse than 2 kpc did not significantly affect their $z < 0.1$ SN sample. Niino et al. (2015) found that local metallicity estimates are more uncertain above spatial of 1 kpc. Galbany et al. (2016) found that total gas-phase metallicities (using the PP04 calibrator) of SN Ia host galaxies are on average larger than local metallicities by 0.03

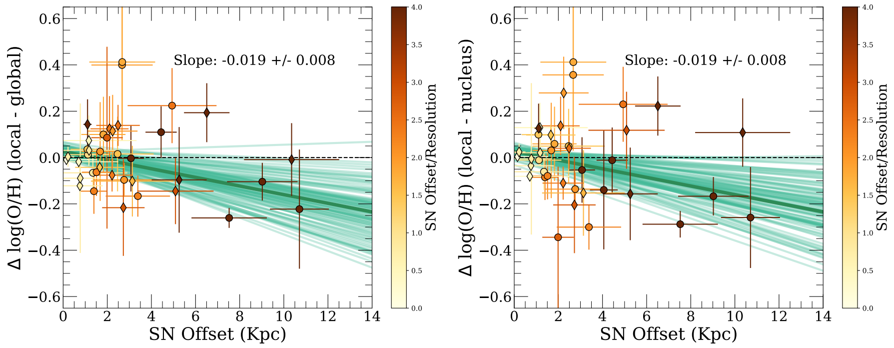

Figure 5.13: (*left panel*): The difference between the local (within 1 kpc of SN location) and global metallicity as function of physical offset from the host galaxy nucleus. (*right panel*): The difference between the local and nuclear (within 1 kpc of galaxy nucleus) metallicity as function of physical offset from the host galaxy nucleus. In both panels, circles are measurements made from Keck-LRIS spectroscopy and diamonds are measurements made from Lick-Kast spectroscopy. Points are colored by the ratio of their physical offset to the estimated seeing. The dark green curve is our best linear fit to the data, and the teal curves are random realizations of the fit drawn from the parameter uncertainties.

dex and that this correction could be applied at high-z. It is widely-agreed that on average metallicity decreases with galactocentric radius. The scatter and slope of this relationship can vary from galaxy to galaxy, however, it would not be surprising if the full Foundation/Swope sample produces a similar trend. In particular, there is marginal evidence (2.4σ) that for for physical offsets > 8 kpc, local metallicities may be systematically lower. With the current sample can say that for SN offsets < 8 kpc, global and nuclear metallicities are relatively safe to use as proxies for local metallicity in high-z samples.

5.3.4 Hubble Residual Dependence on Host Galaxy Properties

In this section we show how Foundation/Swope SN Ia HRs depend on host galaxy properties measured from spectroscopy. As in Siebert et al. (2020a), the HRs used in the analysis are from Jones et al. (2018b). Light curve fits to these data were done using SALT2.4 (Guy et al. 2010; Betoule et al. 2014) and the sample includes shape and color parameter cuts of $-3 < x_1 < 3$ and $-0.3 < c < 0.3$, respectively. We require MW reddening of $E(B-V) < 0.15$ mag and $z > 0.01$ to remove SNe that have distances with large peculiar-velocity uncertainties. We also used the same selection criteria as in the Pantheon analysis (Scolnic et al. 2018) to ensure accurate distances. SN Ia distances are derived using a version of the Tripp (1998) formula that includes a bias correction, $\Delta_B(z)$:

$$\mu = m_B - \mathcal{M} \ + \alpha \times x_1 - \beta \times c + \Delta_B(z) \tag{5.2}$$

Here, m_B is the light curve amplitude, $\mathcal{M}$ is the SN absolute magnitude (whose exact value is degenerate with that of the Hubble constant and is irrelevant when only comparing HRs), and α and β are nuisance parameters that are determined from a fit to the full low-z sample. The BEAMS with Bias Corrections (BBC) method of (Kessler & Scolnic 2017), corrects for observational biases on the x_1, c, and m_B parameters as well as on α and β. Those biases are estimated using large Monte Carlo simulations, generated with the SNANA software (Kessler et al. 2009a), to match the low-z samples observations and sample demographics (parameterized by $\Delta_B(z)$ term). We do not include the host-galaxy mass step correction, γ, since we are aiming to estimate similar relationships with other host galaxy properties that are degenerate with mass.

We estimate HRs relative to the maximum likelihood distances in three redshift bins to remove any dependence on cosmological parameters. Since we are looking for

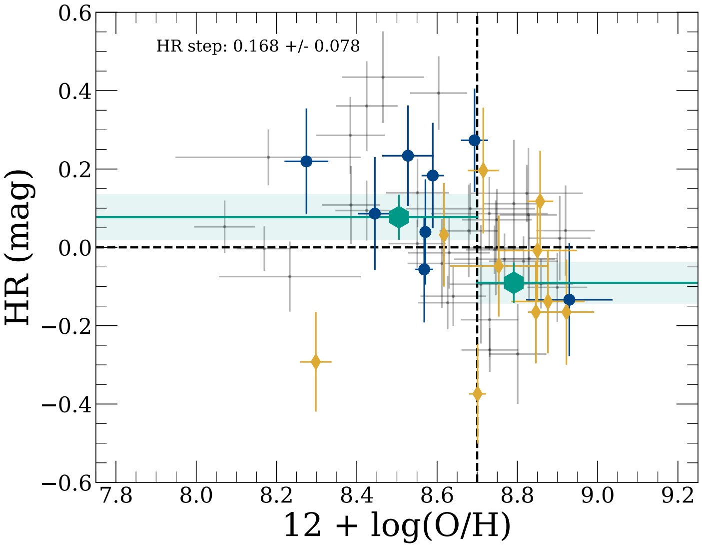

Figure 5.14: HRs as a function of host galaxy global PP04 O3N2 metallicity. Blue circles are measurements made from Keck-LRIS spectroscopy and gold diamonds are measurements made from Lick-Kast spectroscopy. Teal hexagons represent the weighted-mean of HRs in bins of metallicity above and below 12+log(O/H) = 8.7. The shaded regions represent the 1σ uncertainty of HR in each metallicity bin. The black points correspond to measurements from P14 which have been converted to PP04 O3N2 metallicities using the formula from KE08

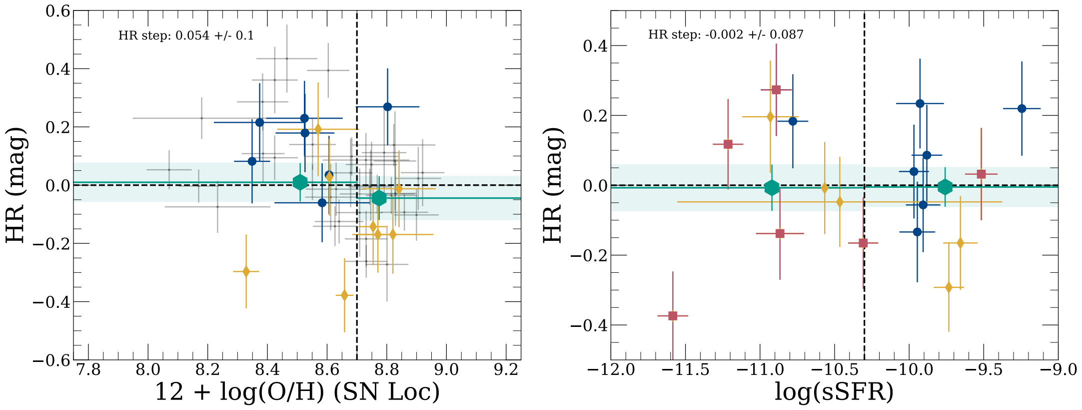

Figure 5.15: (*left panel*): Same as Figure 5.14, but for PP04 O3N2 local metallicity (within 1 kpc of SN location). Measurements from P14 are still global metallicities. (*right panel*): Same as Figure 5.14, but for log(sSFR) measured from Hα. We divide the sample into log(sSFR) bins above and below log(sSFR) = -10.3. Here, measurements from composite galaxies are shown as red squares.

environmental indicators that are the most responsible for HR intrinsic scatter, we do not include intrinsic dispersion into HR uncertainties.

In Figure 5.14, we show HRs as a function of global metallicity using the PP04 O3N2 indicator. Colored circles and diamonds correspond to measurements made from Keck-LRIS and Lick-Kast spectroscopy, respectively. The black background points represent measurements from P14 that have been converted from PP04 N2 to PP04 O3N2 using the formula derived in KE08. From the weighted-mean HRs (teal hexagons) in each metallicity bin, we measure a metallicity step of $0.15 \pm 0.075 (2.0\sigma)$ mag from the Foundation/Swope sample alone. This result is consistent with other studies of SN Ia host galaxy metallicity (D'Andrea et al. 2011; Childress et al. 2013c; Pan et al. 2014) that all found that higher-metallicity galaxies tend to host brighter SNe Ia (lower HR) after shape and color correction. This trend is not surprisingly consistent with a host mass step likely due to the strong positive correlation between galaxy mass and gas-phase metallicity.

Figure 5.15 shows the relationship between HR and local metallicity measured from a 1 kpc region near the SN location (left panel), and the relationship between HR and sSFR measured from the luminosity of Hα. We do not currently detect a strong relationship between HR and local metallicity or log(sSFR). We are currently limited by small number statistics and expect that the full Foundation/Swope sample will be able to determine whether the trend of local metallicity with HR can be accurately approximated by a global measurement. Bravo & Badenes (2011) determined theoretically that the global metallicity of star forming hosts are a good estimator of SN progenitor metallicity. Despite the lack of a correlation seen with log(sSFR), there is a well studied phenomenon that SFR is responsible for additional scatter in the mass-metallicity relationship (the fundamental metallicity relation, or FMR, Mannucci et al. 2010). In particular, at fixed galaxy mass, gas-phase metallicity decreases as SFR increase, therefore we should expect a positive correlation of HR with sSFR if the the relationship is a result of this degeneracy.

5.4 Conclusions

In this work, we analyzed the global and local properties of SN Ia host galaxies from the Foundation/Swope combined cosmological samples. Our measurements primarily relied on optical spectroscopy from the LRIS and Kast spectrographs on the Keck and Lick telescopes, respectively. Our main results are as follows:

1. The mass-SFR relationship measured from our sample is consistent with that of field galaxies (Foster et al. 2012) and that of other SN Ia host populations (P14).
2. Similarly, we find no significant differences between the mass-metallicity relationship of our sample to that of field galaxies (Kewley & Ellison 2008) and that of other SN Ia host populations (P14). This result confirms that SN Ia do not preferentially occur in low- or high-metallicity environments.
3. By aligning the slit with the host galaxy nucleus and SN position, we were able to study both the global and local properties of our sample. We find that global and nuclear metallicities are consistent with local metallicities for SN Ia with physical

offsets from their hosts < 8 kpc. We do not find significant evidence that our local metallicities are affected by the spatial resolution of our measurements.

4. Using the PP04 O3N2 gas-phase metallicity calibrator, we find evidence for a global metallicity step of 0.15 ± 0.075 mag consistent with previous work. We do not yet find significant evidence for a relationship between local metallicity or sSFR.

Detailed spectroscopic measurements of SN Ia host galaxies will not be possible for a large fraction of SNe in next-generation cosmological samples coming from the *Roman Space Telescope* and the Vera C. Rubin Observatory Legacy Survey of Space and Time (LSST). It is clear that more observations of low-z SN Ia host galaxies are needed to better understand how systematic effects related to environment will impact these surveys. In particular, more observations of SN Ia hosted in extremely low metallicity environments are needed to further constrain the functional form of the metallicity-HR relationship.

We need to carefully consider what follow up observations are necessary to properly characterize these spectroscopic relationships. Without a strong link between spectroscopic properties and properties observable through broad-band photometry by LSST or *Roman*, our constraints on dark energy might not improve as much as we hope with this large influx of data. The Dark Energy Spectroscopic Instrument (DESI) Bright Galaxy Survey will obtain spatially resolved spectroscopic information of ten million galaxies and acquire redshifts for more than ten thousand SN host galaxies. This dataset will be critical to further pin down HR relationships with host galaxy properties providing the necessary support for next generation cosmological experiments.

Chapter 6

Summary and Future Directions

In this thesis I have discussed several projects designed to investigate the physical sources of Hubble scatter. In Chapter 2, I presented a new open-source relational database for SN Ia observations (`kaepora`). This resource includes a homogeneous dataset of SN Ia spectra that has been significantly improved by inspecting the data for quality, removing galactic emission lines and cosmic rays, generating variance spectra, and correcting for the reddening caused by both MW and host-galaxy dust. I also presented a set of analysis tools that enable the generation of high-SNR composite spectra that can be precisely controlled for phase and light curve shape. Using sequences of composite spectra, we demonstrated that measurements of their spectral features are representative of their underlying samples. Broad-band measurements from these spectra reproduce the well-studied color evolution of SNe Ia, and the measurements of their individual absorption features reproduce known sequences in luminosity. WE also demonstrated good agreement with other popular spectral templates of SN Ia. We investigated the spectral differences between SNe occurring in early- versus late-type host galaxies and found marginal evidence that Ca II absorption is weaker in SNe Ia occurring in early-type environments.

In Chapter 3, I leveraged `kaepora` to generate composite spectra of SNe Ia with different HRs. We found that composite spectra generated from SNe Ia with negative-HRs tended to have absorption features that were more blue shifted at a variety of phases. We investigated this velocity-HR relationship and found 2.7σ evidence for a 0.091 mag HR-step in Si II absorption velocities above and below $-11{,}000$ km s^{-1} at +4 days. This result is consistent with the velocity-color relationship found in FSK11. Since high-velocity SNe Ia tend to have redder continua, we suggested that current distance estimators may be introducing a bias by over-correcting for SN color.

Then in Chapter 4, I presented novel observations of the high-velocity SN Ia, SN 2019yvq. This SN exhibited a bright UV-flash shortly after explosion. Nebular observations of this SN revealed strong [Ca II] emission, which is direct prediction from theoretical models of double-detonations of sub-Chandreskhar mass WDs. These late time observations suggest a total progenitor mass of 1.15 $M_{\odot}$, larger than what was initially inferred from modeling of the early time light-curve and peak luminosity. We suggested that these results indicate that it is likely that multiple progenitor channels contribute to the main population of "normal" SNe Ia, and likely contribute to our cosmological samples.

Finally, in Chapter 5 I presented early results from the Foundation/Swope host galaxy survey. Here I detailed a large spectroscopic follow up campaign to observe the global and local host galaxy properties of SN Ia contributing to the Foundation and Swope cosmology samples. Initial comparison between environmental indicators from our data and SDSS fiber spectroscopy indicate that differences in aperture size and orientation do not significantly bias our results. With the current sample, we can say that there is good agreement of the mass-SFR and mass- metallicity relationships with past work (P14). We have found that global measurements of metallicity are generally representative of SN environments within 8 kpc of the host nucleus. However, we found marginal evidence that local environments are biased toward lower metallicities when they are significantly offset from their host galaxies. Finally, we measured a global metallicity-step of 0.168 ± 0.078 mag consistent with past results (D'Andrea et al. 2011; Childress et al. 2013c; Pan et al. 2014). We did not yet find significant evidence for local metallicity or sSFR steps, but hope to further constrain their relationships with HR with the full sample.

This thesis demonstrates that there is additional diversity and SN physics that goes unaccounted using current techniques to measure SN Ia distances. While we have shown that distances can be further improved with knowledge of SN ejecta velocities and environment, we still cannot constrain the number and fraction of progenitor channels that contribute to our cosmological samples. One promising avenue toward solving this problem involves further investigating the UV diversity of SNe Ia.

UV spectra of SNe Ia have revealed that progenitor metallicity affects their peak luminosity without affecting light curve shape (Foley et al. 2020). This means that progenitor metallicity is likely a source of Hubble scatter. This phenomenon should be investigated in context with the results presented in this thesis. Since UV observations must be obtained from space, current spectroscopic samples do not adequately cover the basic diversity seen in SN Ia light curve shapes and ejecta velocities. Foley et al. (2016b) used the entire sample of *HST* UV near-peak SN Ia spectra to produce a spectral model that describes the average UV spectrum for an SN with a given light-curve shape. Since the model isolates differences related to width, comparing a SN spectrum to the model provides a way to detect secondary differences, including those from metallicity, without needing a “twin.” However, SN 2021J, which was recently observed, has the highest velocity yet and its UV spectrum is markedly different from all other SN Ia.

In the left panel of Figure 6.1, we show a comparison of the maximum-light UV spectrum of SN 2021J (black curve) to the spectral model from Foley et al. (2016b) (solid colored curves). We do not yet know if this SN is representative of other high-velocity SN Ia, and cannot confidently ascertain its metallicity by comparison to this model. In the right panel of Figure 6.1 we show a similar comparison but with other SNe that have similsr light curve shapes. SN 2021J stills differs greatly at 2500 Å from each of these SNe.

In Figure 6.2, we present pseudo-equivalent width (pEW) measurements of Si II $\lambda5972$ and Si II $\lambda6355$ from maximum light spectra of the *HST*-UV sample. Here four subclasses, “Shallow Silicon,” “Core normal,” “Cool,” and “Broad line,” are defined to represent the known diversity in SN Ia optical properties (Branch et al. 2009). In this parameter space, the x-axis is an indicator of velocity and the y-axis is an indicator of luminosity. We can use this diagram to assess how well the *HST*-UV data samples the

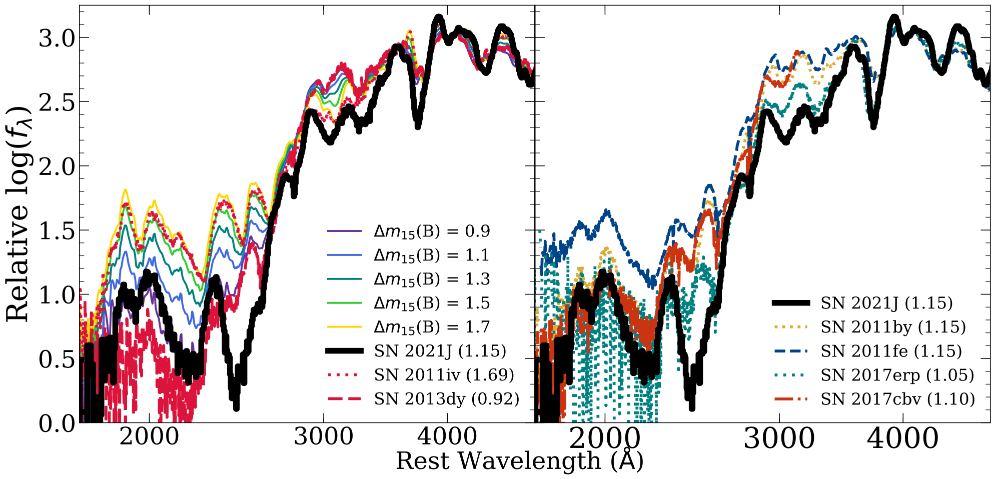

Figure 6.1: (Left): Maximum-light UV spectra of SN 2021J (black, light-curve shape parameter of $\Delta m_{15} = 1.15$ mag), SN 2011iv (small dashes; $\Delta m_{15} = 1.69$ mag, indicating a narrow width), and SN 2013dy (large dashed; $\Delta m_{15} = 0.92$ mag, indicating a broad width) (Foley et al. 2012d; Pan et al. 2015a), normalized to their optical flux. These SN represent the extremes of the current light-curve width and velocity ranges. Overplotted is a data-driven UV spectral model (Foley et al. 2016b) for specific Δm_{15} (listed on plot). The flux at 3000 Å is highly correlated with width. The flux of SN 2021J at 3000 Å is similar to a faster declining SN, but the flux ≤ 2200 Å is similar to slower declining SN. (Right): Similar plot for SN Ia with similar light-curve shapes. SN 2021J has depressed flux at both 2500 and 3000 Å, unlike other similar-width SN and our model. SN 2017erp has the most similar UV continuum to SN 2021J, but still differs greatly at 2500 Å. SN 2021J has the strongest Si II line of our sample, which may be related to this behavior. But more data are necessary to determine the underlying cause and how to account for it.

optical diversity of SN Ia. With the current sample of 15 SN Ia, the parameter space is well represented, but still insufficient for representing the “Broad-line” and “Cool” subclasses.

Future studies should make an effort to understand the full parameter space defined by SN Ia light-curve shape, ejecta velocity, UV continuum, and local environment. These are key observables that we know have close relationships with the distances derived for cosmology. A complete understanding of these effects will allow for a precise

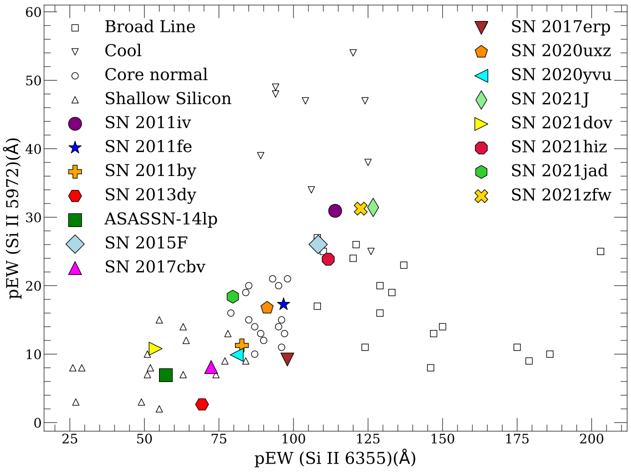

Figure 6.2: Si II λ5972 and Si II λ6355 pseudo-equivalent-width measurements for a sample of SN Ia (empty symbols) and for the *HST*-UV sample (filled symbols). This parameter space defines subclasses of SN Ia (Branch et al. 2009): “shallow silicon,” “core normal,” “cool,” and “broad line” corresponding to high-luminosity SN 1991T-like, typical low-velocity, low-luminosity SN 1991bg-like, and typical HV SN, respectively. UV observations now span most of the parameter space of optical properties for SN Ia, but 45% of nearby SN Ia are outside the range covered by the current sample (i.e., most cool and broad-line SN).

determination of the biases associated with next-generation cosmological samples.

For example, we do not yet know how well *Roman* will be able to measure the velocity distribution of SNe Ia at high redshift using slitless prism spectroscopy. Additionally, the SN Ia cosmology sample from LSST will include a large number of photometrically-classified SNe Ia for which measurements of ejecta velocity, UV continuum, and local environment are not feasible. With a detailed knowledge of the relationships among these observables and their impact on distance measurements, we may be able to define sub-samples of SNe Ia that we consider to be “more standard” than a normal cosmological sample. For example, host galaxy photometry may be adequate to characterize the a progenitor metallicity effect that has been linked to host gas-phase metallicity. Furthermore, it is possible that velocity can be linked to broad-band colors at fixed light curve shape (Foley et al. 2011; Dettman et al. 2021). All of this information should be used to get the most out of the enormous influx of data that next-generation samples will provide.

Bibliography

Almgren A. S., et al., 2010, ApJ, 715, 1221

Altavilla G., et al., 2007, A&A, 475, 585

Amanullah R., et al., 2015, MNRAS, 453, 3300

Anupama G. C., Sahu D. K., Jose J., 2005, A&A, 429, 667

Arnett W. D., 1982, ApJ, 253, 785

Bailey S., et al., 2009, A&A, 500, L17

Baldwin J. A., Phillips M. M., Terlevich R., 1981, PASP, 93, 5

Benetti S., et al., 2004, MNRAS, 348, 261

Benetti S., et al., 2005, ApJ, 623, 1011

Betoule M., et al., 2014, A&A, 568, A22

Bianco F. B., Modjaz M., Oh S. M., Fierroz D., Liu Y. Q., Kewley L., Graur O., 2016, Astronomy and Computing, 16, 54

Bildsten L., Shen K. J., Weinberg N. N., Nelemans G., 2007, ApJ, 662, L95

Black C. S., Fesen R. A., Parrent J. T., 2016, MNRAS, 462, 649

Blondin S., et al., 2006, AJ, 131, 1648

Blondin S., Mandel K. S., Kirshner R. P., 2011, A&A, 526, A81+

Blondin S., et al., 2012a, AJ, 143, 126

Blondin S., et al., 2012b, AJ, 143, 126

Blondin S., Dessart L., Hillier D. J., 2018, MNRAS, 474, 3931

Bloom J. S., et al., 2012, ApJ, 744, L17

Botyánszki J., Kasen D., 2017, ApJ, 845, 176

Botyánszki J., Kasen D., Plewa T., 2018, ApJ, 852, L6

Branch D., 1987, ApJ, 316, L81

Branch D., Chau Dang L., Baron E., 2009, PASP, 121, 238

Bravo E., Badenes C., 2011, MNRAS, 414, 1592

Briday M., et al., 2022, A&A, 657, A22

Brinchmann J., Charlot S., White S. D. M., Tremonti C., Kauffmann G., Heckman T., Brinkmann J., 2004, MNRAS, 351, 1151

Brown P. J., et al., 2018, preprint, (`arXiv:1808.04729`)

Burns C. R., et al., 2014, ApJ, 789, 32

Cao Y., et al., 2015, Nature, 521, 328

Cappellaro E., et al., 2001, ApJ, 549, L215

Childress M. J., et al., 2013a, ApJ, 770, 29

Childress M., et al., 2013b, ApJ, 770, 107

Childress M., et al., 2013c, ApJ, 770, 108

Childress M. J., Wolf C., Zahid H. J., 2014, MNRAS, 445, 1898

Chornock R., Filippenko A. V., Branch D., Foley R. J., Jha S., Li W., 2006, PASP, 118, 722

Cikota A., et al., 2019, MNRAS, 490, 578

Colgate S. A., McKee C., 1969, ApJ, 157, 623

Conley A., et al., 2011, ApJS, 192, 1

Contreras C., et al., 2010, AJ, 139, 519

D'Andrea C. B., et al., 2011, ApJ, 743, 172

De S., et al., 2014, ApJ, 787, 149

De K., et al., 2019, ApJ, 873, L18

Dettman K. G., et al., 2021, ApJ, 923, 267

Dilday B., et al., 2012, Science, 337, 942

Dimitriadis G., et al., 2019a, ApJ, 870, L1

Dimitriadis G., et al., 2019b, ApJ, 870, L14

Dong S., Katz B., Kushnir D., Prieto J. L., 2015, MNRAS, 454, L61

Elias-Rosa N., et al., 2006a, MNRAS, 369, 1880

Elias-Rosa N., et al., 2006b, MNRAS, 369, 1880

Elias-Rosa N., et al., 2008, MNRAS, 384, 107

Fabricant D., Cheimets P., Caldwell N., Geary J., 1998, PASP, 110, 79

Filippenko A. V., et al., 1992a, AJ, 104, 1543

Filippenko A. V., et al., 1992b, AJ, 104, 1543

Filippenko A. V., et al., 1992c, ApJ, 384, L15

Filippenko A. V., et al., 1992d, ApJ, 384, L15

Fitzpatrick E. L., 1999, PASP, 111, 63

Flörs A., et al., 2020, MNRAS, 491, 2902

Folatelli G., et al., 2010, AJ, 139, 120

Folatelli G., et al., 2013a, ApJ, 773, 53

Folatelli G., et al., 2013b, ApJ, 773, 53

Foley R. J., 2012, ApJ, 748, 127

Foley R. J., Kasen D., 2011, ApJ, 729, 55

Foley R. J., Kirshner R. P., 2013a, ApJ, 769, L1

Foley R. J., Kirshner R. P., 2013b, ApJ, 769, L1

Foley R. J., et al., 2008a, ApJ, 684, 68

Foley R. J., Filippenko A. V., Jha S. W., 2008b, ApJ, 686, 117

Foley R. J., Filippenko A. V., Jha S. W., 2008c, ApJ, 686, 117

Foley R. J., et al., 2009a, AJ, 138, 376

Foley R. J., et al., 2009b, AJ, 138, 376

Foley R. J., Narayan G., Challis P. J., Filippenko A. V., Kirshner R. P., Silverman J. M., Steele T. N., 2010, ApJ, 708, 1748

Foley R. J., Sanders N. E., Kirshner R. P., 2011, ApJ, 742, 89

Foley R. J., et al., 2012a, AJ, 143, 113

Foley R. J., et al., 2012b, ApJ, 744, 38

Foley R. J., et al., 2012c, ApJ, 752, 101

Foley R. J., et al., 2012d, ApJ, 753, L5

Foley R. J., et al., 2013, ApJ, 767, 57

Foley R. J., et al., 2014, MNRAS, 443, 2887

Foley R. J., Jha S. W., Pan Y.-C., Zheng W. K., Bildsten L., Filippenko A. V., Kasen

D., 2016a, MNRAS, 461, 433

Foley R. J., et al., 2016b, MNRAS, 461, 1308

Foley R. J., et al., 2016c, MNRAS, 461, 1308

Foley R. J., et al., 2018, MNRAS, 475, 193

Foley R. J., Hoffmann S. L., Macri L. M., Riess A. G., Brown P. J., Filippenko A. V., Graham M. L., Milne P. A., 2020, MNRAS, 491, 5991

Foreman-Mackey D., Hogg D. W., Lang D., Goodman J., 2013, PASP, 125, 306

Foster C., et al., 2012, A&A, 547, A79

Gal-Yam A., Maoz D., Guhathakurta P., Filippenko A. V., 2003, AJ, 125, 1087

Galbany L., et al., 2016, A&A, 591, A48

Galbany L., et al., 2019, A&A, 630, A76

Gallagher J. S., Garnavich P. M., Berlind P., Challis P., Jha S., Kirshner R. P., 2005, ApJ, 634, 210

Gallagher J. S., Garnavich P. M., Caldwell N., Kirshner R. P., Jha S. W., Li W., Ganeshalingam M., Filippenko A. V., 2008, ApJ, 685, 752

Ganeshalingam M., Li W., Filippenko A. V., 2011, MNRAS, 416, 2607

Ganeshalingam M., et al., 2012, ApJ, 751, 142

Garavini G., et al., 2007, A&A, 471, 527

Garnavich P. M., et al., 2004, ApJ, 613, 1120

Gerardy C. L., et al., 2004, ApJ, 607, 391

Goldhaber G., et al., 2001, ApJ, 558, 359

Gomez G., Lopez R., Sanchez F., 1996, AJ, 112, 2094

Goobar A., et al., 2014, ApJ, 784, L12

Graham M. L., et al., 2017, MNRAS, 472, 3437

Graham M. L., et al., 2019, ApJ, 871, 62

Graur O., Bianco F. B., Modjaz M., 2015, MNRAS, 450, 905

Guillochon J., Dan M., Ramirez-Ruiz E., Rosswog S., 2010, ApJ, 709, L64

Guillochon J., Parrent J., Kelley L. Z., Margutti R., 2017, ApJ, 835, 64

Guy J., Astier P., Nobili S., Regnault N., Pain R., 2005, A&A, 443, 781

Guy J., et al., 2007, A&A, 466, 11

Guy J., et al., 2010, A&A, 523, A7+

Hachinger S., Mazzali P. A., Tanaka M., Hillebrandt W., Benetti S., 2008, MNRAS, 389, 1087

Hamuy M., Phillips M. M., Suntzeff N. B., Schommer R. A., Maza J., Aviles R., 1996, AJ, 112, 2391

Hamuy M., Trager S. C., Pinto P. A., Phillips M. M., Schommer R. A., Ivanov V., Suntzeff N. B., 2000, AJ, 120, 1479

Hatano K., Branch D., Lentz E. J., Baron E., Filippenko A. V., Garnavich P. M., 2000, ApJ, 543, L49

Hicken M., Garnavich P. M., Prieto J. L., Blondin S., DePoy D. L., Kirshner R. P., Parrent J., 2007, ApJ, 669, L17

Hicken M., Wood-Vasey W. M., Blondin S., Challis P., Jha S., Kelly P. L., Rest A., Kirshner R. P., 2009, ApJ, 700, 1097

Hicken M., et al., 2012, ApJS, 200, 12

Höflich P., Wheeler J. C., Thielemann F.-K., 1998, ApJ, 495, 617

Hosseinzadeh G., et al., 2017, ApJ, 845, L11

Hounsell R., et al., 2018, ApJ, 867, 23

Howell D. A., 2001, ApJ, 554, L193

Howell D. A., 2011, Nature Communications, 2, 350

Howell D. A., et al., 2009, ApJ, 691, 661

Hoyle F., Fowler W. A., 1960, ApJ, 132, 565

Hsiao E. Y., Conley A., Howell D. A., Sullivan M., Pritchet C. J., Carlberg R. G., Nugent P. E., Phillips M. M., 2007, ApJ, 663, 1187

Iben Jr. I., Tutukov A. V., 1984, ApJS, 54, 335

Iben Icko J., Tutukov A. V., 1996, ApJS, 105, 145

Ivezić Ž., et al., 2019, ApJ, 873, 111

Jacobson-Galán W. V., Dimitriadis G., Foley R. J., Kilpatrick C. D., 2018, ApJ, 857, 88

Jacobson-Galan W. V., et al., 2019a, arXiv e-prints, p. arXiv:1910.05436

Jacobson-Galán W. V., et al., 2019b, MNRAS, 487, 2538

Jacobson-Galán W. V., et al., 2020, ApJ, 896, 165

Jha S., et al., 2006a, AJ, 131, 527

Jha S., Branch D., Chornock R., Foley R. J., Li W., Swift B. J., Casebeer D., Filippenko A. V., 2006b, AJ, 132, 189

Jha S., Riess A. G., Kirshner R. P., 2007, ApJ, 659, 122

Jiang J.-A., et al., 2017, Nature, 550, 80

Jones D. O., et al., 2018a, ApJ, 857, 51

Jones D. O., et al., 2018b, ApJ, 867, 108

Jones D. O., et al., 2019, ApJ, 881, 19

Jones D. O., et al., 2021, ApJ, 908, 143

Kasen D., 2010, ApJ, 708, 1025

Kasen D., Woosley S. E., 2007, ApJ, 656, 661

Kasen D., Thomas R. C., Nugent P., 2006, ApJ, 651, 366

Kauffmann G., et al., 2003, MNRAS, 346, 1055

Kelly P. L., Hicken M., Burke D. L., Mandel K. S., Kirshner R. P., 2010, ApJ, 715, 743

Kelly P. L., et al., 2014, ApJ, 790, 3

Kennicutt Jr. R. C., 1998, ARA&A, 36, 189

Kessler R., Scolnic D., 2017, ApJ, 836, 56

Kessler R., et al., 2009a, PASP, 121, 1028

Kessler R., et al., 2009b, ApJS, 185, 32

Kewley L. J., Ellison S. L., 2008, ApJ, 681, 1183

Kewley L. J., Dopita M. A., Sutherland R. S., Heisler C. A., Trevena J., 2001, ApJ, 556, 121

Kewley L. J., Jansen R. A., Geller M. J., 2005, PASP, 117, 227

Kilic M., Hambly N. C., Bergeron P., Genest-Beaulieu C., Rowell N., 2018, Monthly Notices of the Royal Astronomical Society: Letters, 479, L113

Knop R. A., et al., 2003, ApJ, 598, 102

Kollmeier J. A., et al., 2019, MNRAS, 486, 3041

Kotak R., et al., 2005, A&A, 436, 1021

Krisciunas K., et al., 2011, AJ, 142, 74

Kromer M., et al., 2013, MNRAS, 429, 2287

Kromer M., et al., 2016, MNRAS, 459, 4428

Kron R. G., 1980, ApJS, 43, 305

Lampeitl H., et al., 2010, ApJ, 722, 566

Léget P. F., et al., 2019, arXiv e-prints, p. arXiv:1909.11239

Leibundgut B., et al., 1993, AJ, 105, 301

Lentz E. J., Baron E., Branch D., Hauschildt P. H., Nugent P. E., 2000, ApJ, 530, 966

Leonard D. C., 2007a, ApJ, 670, 1275

Leonard D. C., 2007b, in Immler S., Weiler K., McCray R., eds, American Institute of Physics Conference Series Vol. 937, Supernova 1987A: 20 Years After: Supernovae and Gamma-Ray Bursters. pp 311–315, doi:10.1063/1.3682922

Leonard D. C., Li W., Filippenko A. V., Foley R. J., Chornock R., 2005a, ApJ, 632, 450

Leonard D. C., Li W., Filippenko A. V., Foley R. J., Chornock R., 2005b, ApJ, 632, 450

Leung S.-C., Nomoto K., 2020, ApJ, 888, 80

Li W. D., et al., 1999, AJ, 117, 2709

Li W., et al., 2001a, PASP, 113, 1178

Li W., Filippenko A. V., Treffers R. R., Riess A. G., Hu J., Qiu Y., 2001b, ApJ, 546, 734

Li W., Filippenko A. V., Treffers R. R., Riess A. G., Hu J., Qiu Y., 2001c, ApJ, 546, 734

Li W., et al., 2003, PASP, 115, 453

Li W., et al., 2011a, MNRAS, 412, 1441

Li W., et al., 2011b, Nature, 480, 348

Maeda K., et al., 2008, Science, 319, 1220

Maeda K., et al., 2010a, Nature, 466, 82

Maeda K., Taubenberger S., Sollerman J., Mazzali P. A., Leloudas G., Nomoto K., Motohara K., 2010b, ApJ, 708, 1703

Maeda K., et al., 2011, MNRAS, 413, 3075

Maguire K., et al., 2013, MNRAS, 436, 222

Maguire K., Taubenberger S., Sullivan M., Mazzali P. A., 2016, MNRAS, 457, 3254

Maguire K., et al., 2018, MNRAS, 477, 3567

Mandel K. S., Foley R. J., Kirshner R. P., 2014, ApJ, 797, 75

Mannucci F., Della Valle M., Panagia N., 2006, MNRAS, 370, 773

Mannucci F., Cresci G., Maiolino R., Marconi A., Gnerucci A., 2010, MNRAS, 408, 2115

Maoz D., Mannucci F., 2008, MNRAS, 388, 421

Maraston C., Strömbäck G., 2011, MNRAS, 418, 2785

Marion G. H., et al., 2016, ApJ, 820, 92

Matheson T., Filippenko A. V., Li W., Leonard D. C., Shields J. C., 2001, AJ, 121, 1648

Matheson T., et al., 2008, AJ, 135, 1598

Matteucci F., Greggio L., 1986, A&A, 154, 279

Mattila S., Lundqvist P., Sollerman J., Kozma C., Baron E., Fransson C., Leibundgut B., Nomoto K., 2005, A&A, 443, 649

Mazzali P. A., Chugai N., Turatto M., Lucy L. B., Danziger I. J., Cappellaro E., della Valle M., Benetti S., 1997, MNRAS, 284, 151

Mazzali P. A., Benetti S., Stehle M., Branch D., Deng J., Maeda K., Nomoto K., Hamuy M., 2005a, MNRAS, 357, 200

Mazzali P. A., et al., 2005b, ApJ, 623, L37

Mazzali P. A., et al., 2014b, MNRAS, 439, 1959

Mazzali P. A., et al., 2014a, MNRAS, 439, 1959

Mazzali P. A., Ashall C., Pian E., Stritzinger M. D., Gall C., Phillips M. M., Höflich P., Hsiao E., 2018, MNRAS, 476, 2905

McCully C., et al., 2014, ApJ, 786, 134

Miles B. J., van Rossum D. R., Townsley D. M., Timmes F. X., Jackson A. P., Calder A. C., Brown E. F., 2016, ApJ, 824, 59

Miller A. A., et al., 2020, The Astrophysical Journal, 898, 56

Modjaz M., Li W., Filippenko A. V., King J. Y., Leonard D. C., Matheson T., Treffers R. R., Riess A. G., 2001, PASP, 113, 308

Modjaz M., Kewley L., Bloom J. S., Filippenko A. V., Perley D., Silverman J. M., 2011, ApJ, 731, L4

Niino Y., Nagamine K., Zhang B., 2015, MNRAS, 449, 2706

Noebauer U. M., Kromer M., Taubenberger S., Baklanov P., Blinnikov S., Sorokina E., Hillebrand t W., 2017, MNRAS, 472, 2787

Nomoto K., 1982, ApJ, 257, 780

Nomoto K., Leung S.-C., 2018, Space Sci. Rev., 214, 67

Nomoto K., Thielemann F.-K., Yokoi K., 1984, ApJ, 286, 644

Nugent P., Phillips M., Baron E., Branch D., Hauschildt P., 1995, ApJ, 455, L147

Nugent P., Kim A., Perlmutter S., 2002, PASP, 114, 803

Nugent P. E., et al., 2011, Nature, 480, 344

Oke J. B., et al., 1995, PASP, 107, 375

Östman L., et al., 2011, A&A, 526, A28

Pakmor R., Kromer M., Röpke F. K., Sim S. A., Ruiter A. J., Hillebrandt W., 2010, Nature, 463, 61

Pan Y. C., et al., 2014, MNRAS, 438, 1391

Pan Y.-C., et al., 2015a, MNRAS, 452, 4307

Pan Y.-C., et al., 2015b, MNRAS, 452, 4307

Pan Y.-C., Foley R. J., Filippenko A. V., Kuin N. P. M., 2018, MNRAS, 479, 517

Pan Y. C., Foley R. J., Jones D. O., Filippenko A. V., Kuin N. P. M., 2019, arXiv e-prints, p. arXiv:1906.09554

Pan Y. C., Foley R. J., Jones D. O., Filippenko A. V., Kuin N. P. M., 2020, MNRAS, 491, 5897

Patat F., Benetti S., Cappellaro E., Danziger I. J., della Valle M., Mazzali P. A., Turatto M., 1996a, MNRAS, 278, 111

Patat F., Benetti S., Cappellaro E., Danziger I. J., della Valle M., Mazzali P. A., Turatto M., 1996b, MNRAS, 278, 111

Pereira R., et al., 2013a, A&A, 554, A27

Pereira R., et al., 2013b, A&A, 554, A27

Perets H. B., et al., 2010, Nature, 465, 322

Perlmutter S., et al., 1999, ApJ, 517, 565

Pettini M., Pagel B. E. J., 2004, MNRAS, 348, L59

Phillips M. M., 1993, ApJ, 413, L105

Phillips M. M., Wells L. A., Suntzeff N. B., Hamuy M., Leibundgut B., Kirshner R. P., Foltz C. B., 1992, AJ, 103, 1632

Phillips M. M., Lira P., Suntzeff N. B., Schommer R. A., Hamuy M., Maza J., 1999, AJ, 118, 1766

Phillips M. M., et al., 2007, PASP, 119, 360

Phillips M. M., et al., 2013, ApJ, 779, 38

Pignata G., et al., 2008, MNRAS, 388, 971

Pinto P. A., Eastman R. G., 2000, arXiv e-prints, pp astro–ph/0006171

Pinto P. A., Eastman R. G., 2001, New A, 6, 307

Piro A. L., Morozova V. S., 2016, ApJ, 826, 96

Planck Collaboration et al., 2020, A&A, 641, A6

Polin A., Nugent P., Kasen D., 2019, ApJ, 873, 84

Polin A., Nugent P., Kasen D., 2021, ApJ, 906, 65

Pskovskii I. P., 1977, Soviet Ast., 21, 675

Raskin C., Kasen D., 2013, ApJ, 772, 1

Rest A., et al., 2014, ApJ, 795, 44

Richardson D., Thomas R. C., Casebeer D., Blankenship Z., Ratowt S., Baron E., Branch D., 2001, in American Astronomical Society Meeting Abstracts. p. 1428

Richmond M. W., et al., 1995, AJ, 109, 2121

Riess A. G., Press W. H., Kirshner R. P., 1996, ApJ, 473, 88

Riess A. G., et al., 1997, AJ, 114, 722

Riess A. G., et al., 1998, AJ, 116, 1009

Riess A. G., et al., 1999, AJ, 117, 707

Riess A. G., et al., 2021, arXiv e-prints, p. arXiv:2112.04510

Rigault M., et al., 2013, A&A, 560, A66

Rigault M., et al., 2018, A&A, 612, C1

Roman M., et al., 2018, A&A, 615, A68

Rose B. M., Garnavich P. M., Berg M. A., 2019, ApJ, 874, 32

Ruiz-Lapuente P., et al., 1993, Nature, 365, 728

Ruiz-Lapuente P., Canal R., Isern J., eds, 1997, Thermonuclear supernovae. Proceedings. NATO Advanced Science Institutes (ASI) Series C Vol. 486, doi:10.1007/978-94-011-5710-0.

Salpeter E. E., 1955, ApJ, 121, 161

Salvo M. E., Cappellaro E., Mazzali P. A., Benetti S., Danziger I. J., Patat F., Turatto M., 2001, MNRAS, 321, 254

Sand D. J., et al., 2018, ApJ, 863, 24

Sanders N. E., et al., 2012, ApJ, 758, 132

Sauer D. N., et al., 2008, MNRAS, 391, 1605

Schaefer B. E., Pagnotta A., 2012, Nature, 481, 164

Schlafly E. F., Finkbeiner D. P., 2011, ApJ, 737, 103

Scolnic D., et al., 2015, ApJ, 815, 117

Scolnic D. M., et al., 2018, ApJ, 859, 101

Scolnic D., et al., 2021, arXiv e-prints, p. arXiv:2112.03863

Shappee B. J., Stanek K. Z., Pogge R. W., Garnavich P. M., 2013, ApJ, 762, L5

Shappee B. J., et al., 2016, ApJ, 826, 144

Shappee B. J., et al., 2019, ApJ, 870, 13

Shen K. J., Bildsten L., 2009, ApJ, 699, 1365

Shen K. J., Moore K., 2014, ApJ, 797, 46

Shen K. J., Schwab J., 2017, ApJ, 834, 180

Shen K. J., Kasen D., Miles B. J., Townsley D. M., 2018a, ApJ, 854, 52

Shen K. J., et al., 2018b, ApJ, 865, 15

Siebert M. R., et al., 2019, MNRAS, 486, 5785

Siebert M. R., Foley R. J., Jones D. O., Davis K. W., 2020a, MNRAS, 493, 5713

Siebert M. R., Dimitriadis G., Polin A., Foley R. J., 2020b, ApJ, 900, L27

Silverman J. M., Ganeshalingam M., Li W., Filippenko A. V., Miller A. A., Poznanski D., 2011, MNRAS, 410, 585

Silverman J. M., et al., 2012a, MNRAS, 425, 1789

Silverman J. M., et al., 2012b, MNRAS, 425, 1789

Silverman J. M., Ganeshalingam M., Li W., Filippenko A. V., 2012c, MNRAS, 425, 1889

Silverman J. M., et al., 2013a, ApJS, 207, 3

Silverman J. M., Ganeshalingam M., Filippenko A. V., 2013b, MNRAS, 430, 1030

Silverman J. M., Vinkó J., Marion G. H., Wheeler J. C., Barna B., Szalai T., Mulligan B. W., Filippenko A. V., 2015, MNRAS, 451, 1973

Simon J. D., et al., 2007, ApJ, 671, L25

Spergel D., et al., 2015, preprint, (`arXiv:1503.03757`)

Springel V., Hernquist L., 2003, MNRAS, 339, 289

Stanishev V., et al., 2007, A&A, 469, 645

Stern D., et al., 2004, ApJ, 612, 690

Sternberg A., et al., 2011, Science, 333, 856

Stritzinger M., Mazzali P. A., Sollerman J., Benetti S., 2006, A&A, 460, 793

Stritzinger M. D., et al., 2011, AJ, 142, 156

Sullivan M., et al., 2010, MNRAS, 406, 782

Tanikawa A., Nomoto K., Nakasato N., Maeda K., 2019, ApJ, 885, 103

Taubenberger S., et al., 2009, MNRAS, 397, 677

Taubenberger S., et al., 2013a, MNRAS, 432, 3117

Taubenberger S., Kromer M., Pakmor R., Pignata G., Maeda K., Hachinger S., Leibundgut B., Hillebrand t W., 2013b, ApJ, 775, L43

Taylor E. N., et al., 2011, MNRAS, 418, 1587

The LSST Dark Energy Science Collaboration et al., 2018, arXiv e-prints, p.

arXiv:1809.01669

Thomas R. C., et al., 2007, ApJ, 654, L53

Timmes F. X., Brown E. F., Truran J. W., 2003, ApJ, 590, L83

Tinsley B. M., 1980, Fund. Cosmic Phys., 5, 287

Totani T., Morokuma T., Oda T., Doi M., Yasuda N., 2008, PASJ, 60, 1327

Townsley D. M., Miles B. J., Shen K. J., Kasen D., 2019, ApJ, 878, L38

Tremonti C. A., et al., 2004, ApJ, 613, 898

Tripp R., 1998, A&A, 331, 815

Tucker M. A., Shappee B. J., Wisniewski J. P., 2019, ApJ, 872, L22

Tucker M. A., Payne A. V., Hinkle J., Do A., Huber M. E., Shappee B. J., 2020, Transient Name Server Classification Report, 2020-861, 1

Turatto M., Benetti S., Cappellaro E., Danziger I. J., Della Valle M., Gouiffes C., Mazzali P. A., Patat F., 1996, MNRAS, 283, 1

Valentini G., et al., 2003, ApJ, 595, 779

Vallely P. J., et al., 2019, arXiv e-prints,

Vallely P. J., Tucker M. A., Shappee B. J., Brown J. S., Stanek K. Z., Kochanek C. S., 2020, MNRAS, 492, 3553

Walker E. S., Hachinger S., Mazzali P. A., Ellis R. S., Sullivan M., Gal Yam A., Howell D. A., 2012, MNRAS, 427, 103

Wang L., Baade D., Höflich P., Wheeler J. C., Kawabata K., Khokhlov A., Nomoto K., Patat F., 2006, ApJ, 653, 490

Wang X., et al., 2008a, ApJ, 675, 626

Wang X., et al., 2008b, ApJ, 675, 626

Wang X., et al., 2009a, ApJ, 697, 380

Wang X., et al., 2009b, ApJ, 699, L139

Wang X., Wang L., Filippenko A. V., Zhang T., Zhao X., 2013, Science, 340, 170

Wang X., Chen J., Wang L., Hu M., Xi G., Yang Y., Zhao X., Li W., 2019, ApJ, 882, 120

Webbink R. F., 1984, ApJ, 277, 355

Wells L. A., et al., 1994a, AJ, 108, 2233

Wells L. A., et al., 1994b, AJ, 108, 2233

Whelan J., Iben I. J., 1973, ApJ, 186, 1007

Wilk K. D., Hillier D. J., Dessart L., 2020, MNRAS, 494, 2221

Wilkinson D. M., Maraston C., Goddard D., Thomas D., Parikh T., 2017, MNRAS, 472, 4297

Woosley S. E., Kasen D., 2011, ApJ, 734, 38

Woosley S. E., Weaver T. A., 1994, ApJ, 423, 371

Woosley S. E., Taam R. E., Weaver T. A., 1986, ApJ, 301, 601

Yamanaka M., et al., 2009, PASJ, 61, 713

Yao Y., et al., 2019, ApJ, 886, 152

Yaron O., Gal-Yam A., 2012, PASP, 124, 668

Zhang T., et al., 2010, PASP, 122, 1

Zhang K. D., et al., 2020, MNRAS, 499, 5325

Zheng W., et al., 2013, ApJ, 778, L15

Zheng W., Kelly P. L., Filippenko A. V., 2018, ApJ, 858, 104